

UNIVERSITY OF BERGEN
DEPARTMENT OF PHYSICS AND TECHNOLOGY



Master thesis
Optics and atomic physics

Characterization of Hyper Spectral Irradiance and Radiance Sensors

By: Jørund Tveiterås

Supervisors: Øyvind Frette and Børge Hamre

September 11, 2013

Preface

Abstract

It is surprisingly problematic to accurately measure light in the laboratory. Even more so when measuring in the field. There are lots of areas where measuring light spectrum and irradiance outside a laboratory is of great interest. For instance spectra which vary with algae concentrations in the sea, concentration of different gases in the atmosphere and UV radiation to name a few. Trios has made a versatile set of irradiance and radiance sensors for different types of wavelength ranges, that could potentially be very well suited for these types of tasks. However there have been observed some inaccurate data when using them in the field. In this thesis we will take a closer look at the different Trios Ramses sensors and their characteristics to see if there are any errors in the sensors. If any errors are present look for corrections or improvements to these errors. There are certain areas that are known to be problematic when measuring light irradiance, like the cosine response. This and other aspects have been carefully tested in a laboratory environment. We have used these results to make corrections to the field measurements. Finally compared the corrected measurements to the results calculated from a radiative transfer model.

Contents

Preface	i
Abstract	i
1 Introduction	2
1.1 Why light is important	2
1.2 Applications of spectral light measurements	4
1.3 Challenges in accurately measuring solar spectra	8
1.4 Motivation	8
1.5 Outline of the thesis	9
2 Theory	11

2.1	Light	11
2.2	Uncertainty in measurements	15
2.3	Spectrometers	18
3	Presenting the instruments	20
3.1	Radiance sensors	21
3.2	Irradiance sensors	24
3.3	The inner workings of the instruments	26
3.4	Data handling	28
4	Data collected in the laboratory	31
4.1	Setup	31
4.2	Spectral accuracy	33
4.3	Determining the field of view of a radiance sensor	35
4.4	Cosine response of the 80FB and 80E2 Irradiance sensors	40
4.5	Comparing the different sensors	51
4.6	Examining possible problems in the setup, and determining the uncertainty of the measurements	57
4.7	Uncertainty of the measurements	67
4.8	Drift of the sensors	70
5	Measurements in natural sunlight	74
5.1	17. January, clear sky weather conditions	75
5.2	07. February, clear sky weather conditions	78
5.3	12. February, shifting weather conditions	81
5.4	Measured UV-index	84
6	Model	85
6.1	C-disort	85
6.2	Sample comparison of model and measurements	89
6.3	Corrections	91
7	Conclusion	98

List of Figures

1.1	Image of the sun shining on the earth. Credit: NASA/ISS expedition 13 . . .	2
1.2	Image of how far down into the ocean the different colors of light penetrates. Credit: Kyle Carothers, NOAA-OE	3
1.3	Satellite image of a phytoplankton bloom taken in 2008. This bloom is most likely a result of Volcanic eruptions on Iceland Langmann et al. (2010). NASA image by Jeff Schmaltz, MODIS Rapid Response Team.	5
1.4	Calculated irradiance at various depths of the ocean.	7
2.1	Illustration of a light beam traveling through a medium. Adapted from: Kirk (1994)	13
2.2	Illustration of Lambert’s cosine law and what percentage of the incoming irradiance is observed at the surface. From Ryer (1997).	15
2.3	Gaussian distribution of a set of 1000 random numbers generated by Matlab. 68 percent fall within one standard deviation (cyan line) and 95 percent within two standard deviations (magenta line)	17
3.1	RAMSES-ARC Hyper-spectral UV-VIS Radiance Sensor. From: TriOS (2012)	21
3.2	Sketch of a radiance sensor, with the field of view shown in the gray area. .	22
3.3	Illustration of the optics of the Ramses radiance sensors.	23
3.4	RAMSES-ACC-VIS Hyper-spectral UV-VIS Irradiance Sensor. From TriOS (2012).	24
3.5	The layout of the Zeiss mms1 spectrometer. From: TriOS (2012).	27
3.6	Example of the raw output from the 80E2 irradiance sensors when measuring light from the standard calibration lamp used in our laboratory experiments.	28
3.7	Example of calibrated spectrum from the raw data plotted in figure 3.6. Measurement of the calibration lamp used in the laboratory by the 80E2 irradiance sensor.	30
4.1	Illustration of the setup used for the measurements performed in the laboratory (showing the other rotating side in dashed lines). θ is the angle between the normal of the sensor and the incoming light.	32
4.2	The spectrum (data points) of a 532.0 nm wavelength laser, and a Gaussian fit applied to the data points.	34

4.3	Plots of the different spectra measured by the radiance sensor 804A at different angles	36
4.4	Radiance as a function of the angle between the normal and the incoming light for four selected wavelengths. Specified field of view determined as a theoretical 100% radiance inside, 0% outside the manufacturer's specified field of view of 7°.	37
4.5	Calculated field of view from equation 4.3 of the 804A radiance sensor for all wavelengths in its range	39
4.6	The cosine response error, $\epsilon(\theta)$, in percent, of the 80FB irradiance sensor at light coming in at various angles , for all of the wavelengths in its range . .	41
4.7	Calculated $\epsilon_{isotropic}$ for the entire spectrum of the two irradiance sensors 80FB and 80E2	42
4.8	The cosine response error, $\epsilon(\theta)$, of the 80E2 irradiance sensor at various incoming angles of light, in percent, for all of the wavelengths in its range. .	44
4.9	The cosine response error $\epsilon(\theta)$ as a function of the angle between the normal and the incoming light. Presenting four selected wavelengths of the light. As measured by the 80FB irradiance sensor.	45
4.10	The cosine response error $\epsilon(\theta)$ as a function of the angle between the normal and the incoming light. Presenting four selected wavelengths of the light. As measured by the 80E2 irradiance sensor.	46
4.11	The cosine response error of the 80E2 irradiance sensor as a function of angle. Plotted for all of the wavelengths in its range. With a colorbar to identity the different wavelengths	47
4.12	From the Trios Ramses manual TriOS (2012): A typical cosine response curve for the Ramses sensors.	48
4.13	Comparison of cosine response measurements of the 80E2 sensor and an ideal cosine curve.	49
4.14	Deviation from cosine response in absolute values for 80E2 irradiance sensor at for selected wavelengths.	50
4.15	The spectrum of the calibration lamp as measured by the three different irradiance sensors. Including the spectra without recalibration coefficients .	52
4.16	The spectrum of the calibration lamp as measured by the two radiance sensors (804A and 810C). Including new calibration coefficients for the 810C sensor.	53

4.17	The spectrum of the calibration measured by the irradiance sensor 80FB compared to the spectrum measured by the radiance sensor 804A of white reflector (multiplied by pi).	55
4.18	The spectrum of the calibration measured by the irradiance sensor 80FB compared to the spectrum measured by the radiance sensor 810C of white reflector (multiplied by pi).	56
4.19	The spectra measured at $\theta = 95^\circ$ or $E_{measured}(95^\circ)$ by the 80FB and 80E2 irradiance sensors.	58
4.20	The percentage difference, for the entire spectrum, between the two rotational directions for the 80E2 irradiance sensor. Found when measuring the cosine response at the selected angles.	59
4.21	The percentage difference, for the entire spectrum, between the two rotational directions for the 80FB irradiance sensor. The difference was found when measuring the cosine response at the selected angles.	61
4.22	Change in measured irradiance over time for the calibration lamp. The voltage of the power supply was kept continuously at 15.000 V. Measurements were obtained by the 80FB irradiance sensor.	63
4.23	The standard deviation of the calibration lamp in percent for the entire spectrum. This result was calculated from the measured irradiance from 10 minutes after the lamp was turned on. Measurements were obtained by the 80FB irradiance sensor.	64
4.24	Change in measured irradiance for different distances r between the calibration lamp and the sensor compared to the default position of r equal to 50.3 cm.	65
4.25	The relative change in the measured irradiance for different voltage output of the power supply.	66
4.26	The combined uncertainty in the measured irradiance, at $\theta = 0^\circ$, calculated for the entire spectrum. Calculated from equation 4.11.	68
4.27	Uncertainty in the measured irradiance, for both sensors, at the various angles between the normal of the sensor and the incoming light. Calculate from equation 4.13.	69

4.28	Change in the measured irradiance over time as measured by the 80E2 sensor. Every wavelength are plotted separately with a colorbar to identify them. All measurements are performed in the same position, and with the same standard calibration lamp.	71
4.29	Change in the measured irradiance over time as measured by the 80FB sensor. Every wavelength are plotted separately with a colorbar to identify them. All measurements are performed in the same position, and with the same standard calibration lamp.	72
4.30	Change in the measured irradiance over time as measured by the 82E6 sensor. Every wavelength are plotted separately with a colorbar to identify them. All measurements are performed in the same position, and with the same standard calibration lamp.	73
5.1	Radiance measured by the 810C radiance sensor on 17. January at 13:15. Weather conditions was clear sky.	75
5.2	Radiance measured by the 810C radiance sensor on 17. January. Each line is the difference for a single wavelength over time, with a colorbar to identify the wavelengths. Weather conditions was clear sky.	76
5.3	The difference, in percent, between the two radiance sensors (804A and 810C). Each line is the difference for a single wavelength over time, with a colorbar to identify the wavelengths. Both instruments were making measurements at the same time and in the same position. Weather conditions was clear sky.	77
5.4	Example of a single wavelength, 664.1 nm, as measured by the two irradiance sensors (80FB, 80E2) and the radiance sensor (810C). Weather conditions was clear sky. Note: different y-axis used for the radiance.	78
5.5	07. February. Plot of the solar spectrum as it was measured throughout the day by the 80E2 irradiance sensor. Weather conditions was clear sky.	79
5.6	The difference, in percent, between the two irradiance sensors (80FB and 80E2). Each line is the difference for a single wavelength over time, with a colorbar to identify the wavelengths. Both instruments were making measurements at the same time and in the same position. Weather conditions was clear sky.	80

5.7	Example of a single wavelength, 664.1 nm, as measured by the two irradiance sensors (80FB, 80E2) and the radiance sensor (810C). Weather conditions were shifting cloud cover. Note: different y-axis used for the radiance.	81
5.8	12. February. Plot of the solar spectrum as it was measured throughout the day by the 80E2 irradiance sensor. Weather conditions were shifting cloud cover.	82
5.9	The difference, in percent, between the two irradiance sensors (80FB and the 80E2). Each line is the difference for a single wavelength over time, with a colorbar to identify the wavelengths. Both instruments were making measurements at the same time and in the same position. Weather conditions were shifting cloud cover.	83
5.10	Calculated UV index based on measurements by the 80FB irradiance sensor and the 82E6 UV-irradiance sensor. Note that the 80FB sensor does not include measurements below 320 nm, it can not be considered a complete UV-index.	84
6.1	Illustration of the radiative transfer model used in the c-distort model to calculate irradiance. Dividing the atmosphere and ocean into homogeneous layers.	86
6.2	Example of different solar light spectra calculated by c-disort model, at the top of the atmosphere, sea level and for various depths in the ocean.	88
6.3	Comparison of the measured irradiance on the roof of the IFT university building in Bergen to the output both for 12 and 1 nm bandwidth, from the C-disort model. The input to the model mimicked the actual conditions for the sample day. the input is displayed in table 4.	90
6.4	Calculated solar spectrum from the c-disort model. Including the irradiance from the direct part of the solar spectrum and what fraction of the solar irradiance comes from the direct part.	92
6.5	The correction factor C for the 80E2 sensor. From equation 6.2. With α as calculated by c-disort. ϵ_{direct} and $\epsilon_{diffuse}$ from the measurements in the laboratory (see figure 4.7 and figure 4.8)	93
6.6	Comparison of the measurements corrected for cosine error and the spectrum calculated from the accurate model with a 12 nm bandwidth. Also included is an estimated correction for a 1.5 degree tilt of the instrument towards the sun.	95

6.7	Showing the difference in percent between the corrected measurements and modeled and calculated compared to the model as a function of wavelength	96
-----	---	----

List of Tables

1	The sensors used in this thesis	20
2	Calculated characteristics from the measurement of a 532.0 nm laser for the two irradiance sensors. 95 percent confidence intervals in parenthesis	35
3	Input parameters to the C-disort model used for calculations of the irradiance displayed in figure 6.2	88
4	Input parameters to the C-disort model used for calculations of the irradiance displayed in figure 6.3	89

1 Introduction



Figure 1.1: Image of the sun shining on the earth. Credit: NASA/ISS expedition 13

1.1 Why light is important

The visible light spectrum (400-700 nm) is very important for all life on earth. There is a peak in the energy-spectrum from sunlight in this part of the spectrum. We also have a dip in the absorption spectrum of water. This means that almost all the radiance below sea-level is in this range, as shown in figure 1.2. This is why life evolved by taking advantage of this range. Above sea-level there is a wider energy-spectrum available but most life is still dependent on the visible spectrum Demmig-Adams and Adams (2000). In figure 1.4 we see that the absorption spectrum of some of the most common photosynthetic pigments of plants and algae peaks in the visible range. Almost all of the ecosystems on the earth have photosynthesis as a starting point. This synthesis of sunlight into organic

compounds is also known as primary production and is closely linked to the amount of light available. Since primary production involves the absorption of light it will have an impact on the amount of light being scattered from this location. Therefore it is naturally of great interest to measure light-irradiance at different locations. Light provides fuel, oxygen and vision for living creatures. This range of the spectrum also plays a very big role in a host of different environmental aspects around the globe. Bendall et al. (2008) looks at how the atmosphere has changed due to photosynthesis and how this affects the climate.

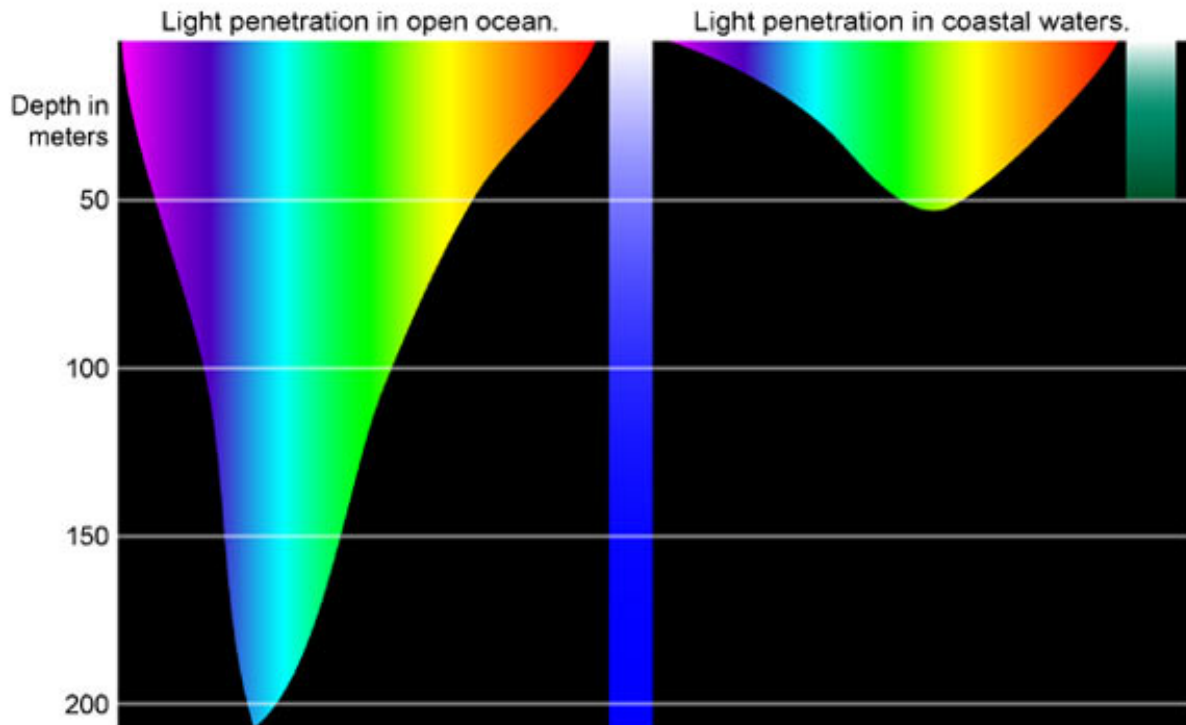


Figure 1.2: Image of how far down into the ocean the different colors of light penetrates. Credit: Kyle Carothers, NOAA-OE

1.2 Applications of spectral light measurements

Many models make use of a default solar spectrum as input. Unfortunately there is no standard spectrum defined. Shanmugam and Ahn (2007) examines how using different default solar irradiance spectra leads to different results for remote sensing operations and models. They found differences ranging from 1% in the NIR to as big as 6% differences in the UV-region. Thus highlighting the need for careful measurements of the solar spectrum both on the ground and from satellites. This will allow more accurate applications of the different models, and make the results easier to compare.

There is exciting research being done with the sun as a source for heating and desalination of sea water. Dreizin et al. (2008) looks at large scale operations in Israel while Fritzmann et al. (2007) presents the low energy method of reverse osmosis. Accurate measurements of the energy below the surface will improve the efficiency of these methods. Muaddi (2012) used knowledge of the solar spectrum, the response curve of solar cells and the absorption coefficient of water to calculate the efficiency of different measuring devices as a function of depth. Finding that most cells increase efficiency up to a certain depth before decreasing.

Doing spectral measurements of water can give us a lot of information about the contents of the water, for example different pollutants, algae concentrations and general water quality.

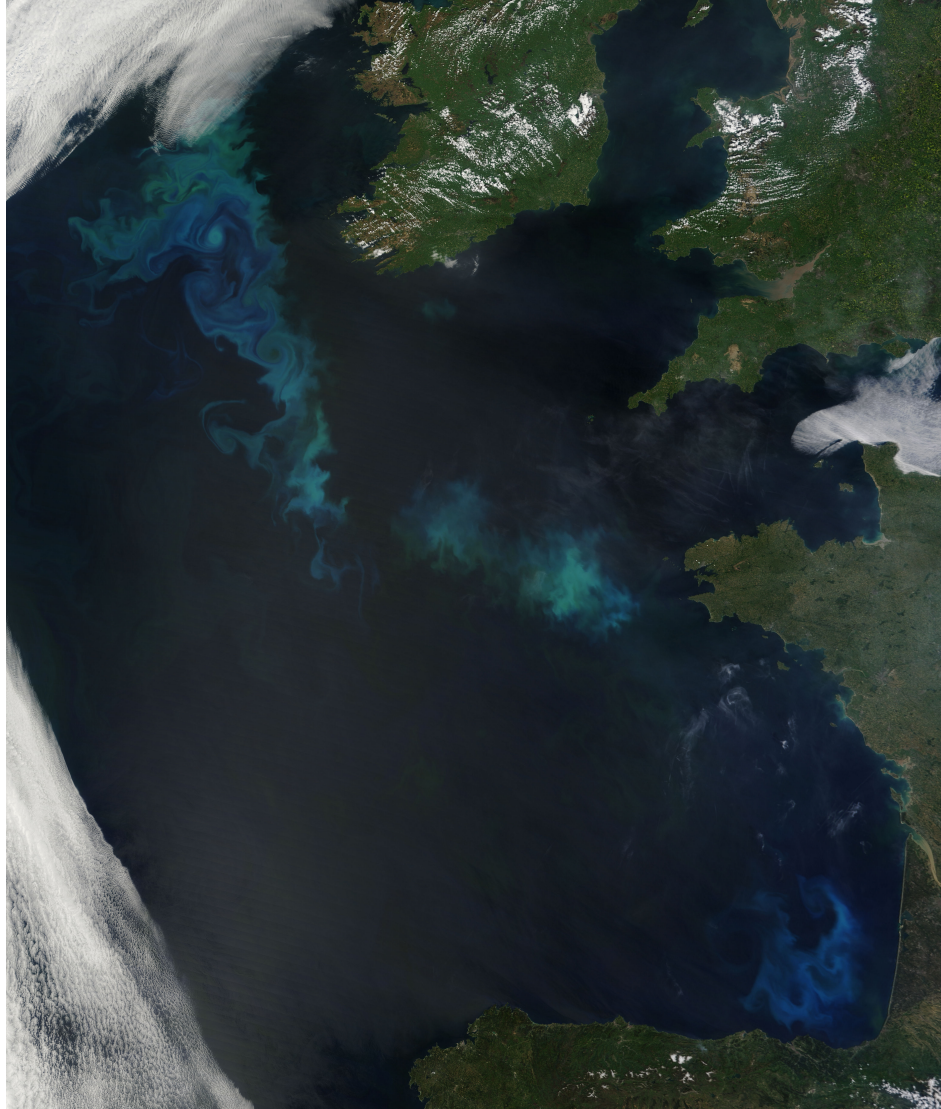


Figure 1.3: Satellite image of a phytoplankton bloom taken in 2008. This bloom is most likely a result of Volcanic eruptions on Iceland Langmann et al. (2010). NASA image by Jeff Schmaltz, MODIS Rapid Response Team.

Erga et al. (2012) shows how to use the link between optical properties and phytoplankton as a tool for exploring different theories on what affects the algae production in a Norwegian fjord. Chen et al. (2012) uses a spectral analysis to look at the optical properties of the aerosols over Svalbard and the northern part of Norway, and discovered that the aerosols were dominated by fine-mode particles. Erga et al. (2010) looks at algae development in water columns, and study how the light conditions control the vertical mobility

of the algae. In a recent study Erga et. al used the Ramses sensors for a closer look at how algae responds to different parts of the visible spectrum instead of just looking at the total irradiance. This was achieved by exposing algae to a single colored light-diode. Hamre (2008) makes the argument that ozone depletion could lead to higher primary production in the Arctic. This is because in this region primary production is often limited by lack of light. Ozone also stops some of the visible light spectrum as opposed to the more common conception that it only stops UV-light. We see that the link between different environmental aspects is not always as straight forward as one might expect.

There is even development of techniques using light scattering as diagnostic tool for skin cancer and other diseases. Lieber et al. (2008) and Balter Medical are showing promising results using similar techniques for processing the scattered light as the ones used for remote satellite monitoring of oceans. Bhandari et al. (2012) explores the Stokes scattering matrix for human skin. While in Bhandari et al. (2011) they use the Mie theory to model the different optical properties of particles in the skin.

By also measuring the ultraviolet part of the spectrum we get another important tool for environmental research. Chen et al. (2013) have measured the extreme UV-radiation in Tibet. Showing how relative small changes (most likely in air circulation and altitude) can lead to harmful radiation levels.

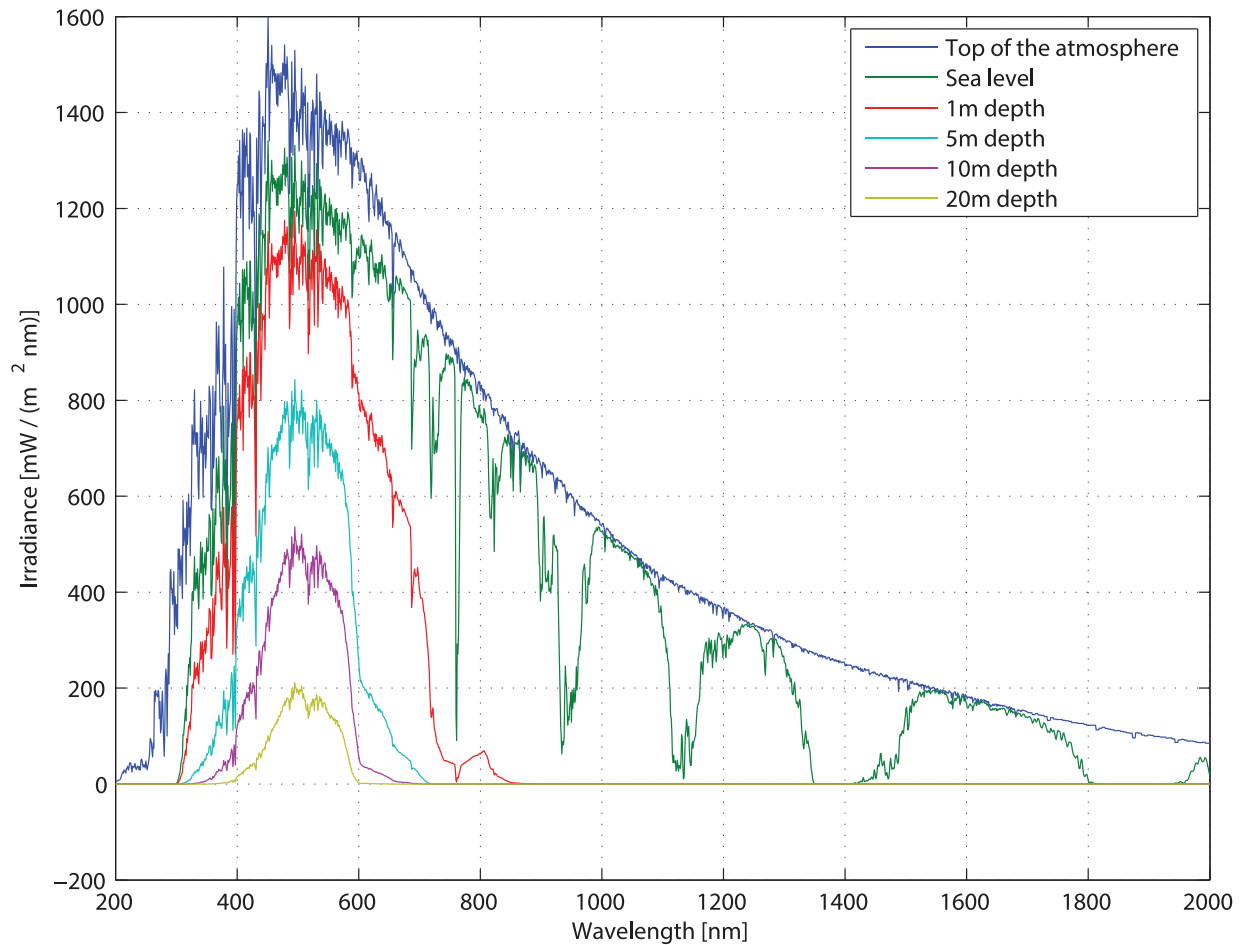


Figure 1.4: Calculated irradiance at various depths of the ocean.

Kiang et al. (2007) examines the spectral signatures of different plants on the earth and looks at possible evolutionary explanations of why plants are reflective in one area and absorbing in another area of the spectrum, or in other words an answer to the age old question of why are plants green? Kiang et al. (2007) examines the possible link between photosynthesis as a signature for life and how this signature would change with different stars as a way of using spectral analysis to search for life in other solar systems.

Remote sensing for large scale monitoring of oceans have the potential to be very useful, (Platt and Sathyendranath (1988)) determines the concentrations of gases and aerosols in the atmosphere and ocean by comparing the spectrum registered by the satellite to spectra calculated by models. The Ferrybox project led by the Norwegian institute of water

research is another alternative to on site measurements. Where different ships are used as carriers for various sensors for automated measurements of water contents and quality.

This is just a small sample of some of the work being done with spectral analysis of light around the world. But hopefully it is clear that there exists many areas of research that would benefit from accurate measurements of the light spectrum. The better we get at measuring the better we will understand the world around us.

1.3 Challenges in accurately measuring solar spectra

Even though better and better models are being developed and satellites can cover vast areas, there will always be a need for on site measurements to confirm the data. The more data points we have the more accurate models we can make. However there are more problems with simple measurements of light than one might expect. Some difficulties from spectral analysis arise from the big range of the typical irradiance values and the big variations in irradiance at the different wavelengths. The small width of the absorption lines for different atmospheric gases and aerosols place a high requirement on bandwidth size. Zibordi and Bulgarelli (2007), Grainger et al. (1993), Michalsky et al. (1995) and Bais et al. (1998a) look at the weaknesses in different sensors, and discusses various methods for reducing the errors observed. One recurring theme in this area is the increase in error observed with increasing solar zenith angle. Because there are so many days where the sun only appears close to the horizon in areas of higher latitudes such as the Arctic. In the north pole the sun is never higher on the horizon than 23.44 degrees (equal to the tilt of the earth axis). It becomes clear that this increase in error with increasing solar zenith angle is of extra importance for research in these areas. Gröbner et al. (1996) examines how the estimated error in the cosine response is affected by varying degrees of diffuse solar radiation.

1.4 Motivation

As we have shown there are many uses for quick and easy spectral analysis of light at different locations. However it can be quite problematic obtaining affordable and reliable

instruments with good accuracy. Trios has made a series of sensors, called Ramses, that are designed for hyper-spectral measurements in the field. These sensors are potentially very good for a variety of applications both on land and under water. The Norwegian Polar Institute, the Norwegian Institute for Water Research (NIVA) and the University in Bergen (UiB) among others has bought several Ramses sensors for monitoring different environmental parameters in Norway and in the Arctic. However there has been a growing concern about the accuracy of these sensors. There were reports of sudden changes in the output, and tests were performed that appeared to undermine the quality of the instruments (Oral source). Another issue was the lack of documentation available on some key aspects of the sensors such as the bandwidth and precise measurements of the cosine response. These sensors are not overly expensive but not so cheap that they can easily be discarded either. Therefore there was a need to thoroughly test these sensors and find out if they performed up to standards. This is the main motivation for this thesis. To thoroughly test these sensors in a laboratory setting, and conclude if there exist any major faults. And if any faults are discovered, find a way to correct them.

1.5 Outline of the thesis

Chapter 2: A brief outline of the various theories used in this thesis.

Chapter 3: An introduction of the different sensors. And an explanation of how they work.

Chapter 4: The set-up in the laboratory. The results of all our tests regarding different aspects of the sensors. How these results can be used to improve measurements and a discussion about the uncertainty of our measurements.

Chapter 5: Examples of field measurements, and how the different sensors compare to each other when measuring the same solar spectrum.

Chapter 6: We used a model, *c-disort*, that calculates a theoretical spectrum and compare this spectrum with the one we have measured.

Chapter 7: Conclusion and summary of results.

2 Theory

2.1 Light

In this thesis we have used two different definitions when measuring light.

Radiance: The quantity of radiation that passes through or is emitted from a surface and falls within a given solid angle in a specified direction.

Irradiance: The quantity of radiation that passes through or is emitted from a surface.

Light as we observe it can appear to behave both as a particle and a wave. For shorter wavelengths (UV-region) more like a particle and for longer wavelengths (Infrared-region) more like waves, and the visible spectrum something in between both as a particle and a wave. A single photon behaves in quite a random fashion as explained by Quantum Theory. This randomness is mostly ignored in optics since we have so many photons that the random distribution evens out (Ryer (1997)).

2.1.1 Photon energy

Each photon carries energy proportional to its frequency,

$$E = h \cdot \nu, \tag{2.1}$$

where h is Planck constant and ν is the frequency of the photon. This explains why UV light is more dangerous than visible light even though we have more total energy in the visible spectrum of sunlight. Each photon from the UV-region has the potential to do much more biological damage. The biological damage to human skin tissue which is used to calculate the UV index, has been quantified in the CIE Erythema action spectrum

as follows:

$$\begin{aligned} \text{ery}(\lambda) &= 1.0 & 250nm \leq \lambda \leq 298nm \\ \text{ery}(\lambda) &= 10^{0.094(298-\lambda)} & 298nm \leq \lambda \leq 328nm \\ \text{ery}(\lambda) &= 10^{0.015(139-\lambda)} & 328nm \leq \lambda \leq 400nm, \end{aligned} \quad (2.2)$$

Webb et al. (2011).

2.1.2 Attenuation

Beer-Lambert's law or the extinction law gives the attenuation of a light beam traveling through a homogeneous medium. There is exponential decay of the radiance L of the light beam:

$$L = L_0 \cdot \exp^{-(s \cdot k)} \quad (2.3)$$

where L_0 is the radiance at the start and s is the distance traveled and k is the extinction coefficient of the medium. This law does not take into account multiple scattering.

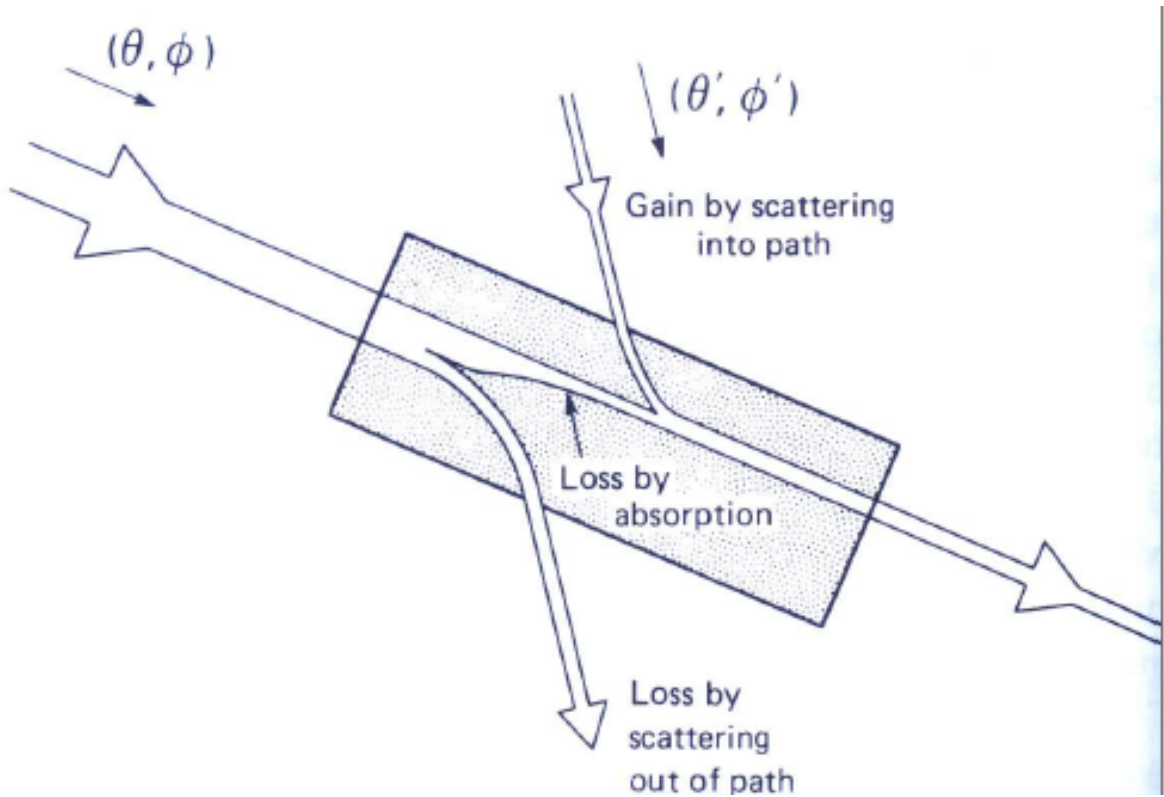


Figure 2.1: Illustration of a light beam traveling through a medium. Adapted from: Kirk (1994)

To solve for this more complex problem we use the radiative transfer equation.

$$\frac{dL}{ds} = -kL + \frac{\sigma}{4\pi} \int_{4\pi} dw' p(\hat{\Omega}', \hat{\Omega}) L(\hat{\Omega}') + Q, \quad (2.4)$$

where L is the radiance, k is the extinction coefficient, σ the scattering coefficient, $p(\hat{\Omega}', \hat{\Omega})$ is the scattering phase function, and Q is the single scattering source term provided by the direct solar beam.

2.1.3 Inverse square law

The inverse square law tells us about how the energy, E , from a single point light source, with power P , changes with distance from the light source,

$$E = \frac{P}{4\pi r^2}. \quad (2.5)$$

The energy is inversely proportional to the distance from the source squared. In reality we don't have many single point sources, but if we are measuring far away compared to the size of the source the single point source can be used as a good approximation.

2.1.4 Snell's law

Snell's law describes how light refracts when crossing the boundary between medium 1 and medium 2.

$$n_1 \cdot \sin(\theta_1) = n_2 \cdot \sin(\theta_2) \quad (2.6)$$

Where n is the index of refraction for the different media and θ is the angle of the light compared to the normal of the interface. We see that the higher the change in the index of refraction the more the light will bend.

The index of refraction (n) of a medium relates to the speed of light propagating through that medium. It is defined as:

$$n(\lambda) = \frac{c}{v(\lambda)} \quad (2.7)$$

where c is the speed of light in vacuum and v is the speed of light in the medium. As the speed of light changes with wavelength in most media the index of refraction changes with the wavelength of light as well.

2.1.5 Lambert's cosine law

The irradiance observed at a surface can be expressed as a function of the angle between the normal of the surface and the incoming irradiance. This is known as Lambert's cosine law:

$$E = E_{incoming} \cdot \cos(\theta) \quad (2.8)$$

Lambert's cosine law is illustrated in figure 2.2.

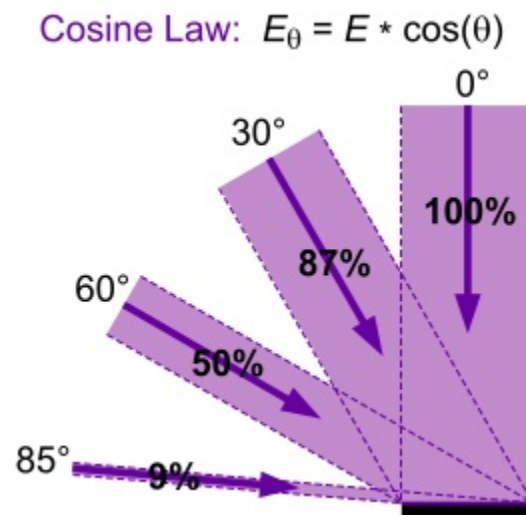


Figure 2.2: Illustration of Lambert's cosine law and what percentage of the incoming irradiance is observed at the surface. From Ryer (1997).

2.2 Uncertainty in measurements

In general we have two types of uncertainties for measurements.

Random uncertainties that will be reduced the more measurements we make.

Systematic uncertainties that remain the same for all measurements.

2.2.1 Standard Deviation

The estimated standard deviation s from a set of repeated measurements gives us information about the spread of the readings. Two thirds of the readings are within one standard deviation from the average value,

$$s = \sqrt{\frac{\sum_{i=1}^n (x_i - \bar{x})^2}{(n-1)}}, \quad (2.9)$$

where s is the estimated standard deviation, \bar{x} is the average value, and x_i is the i th measurement of the n measurements.

2.2.2 Uncertainty for uncorrelated variables

The combined uncertainty Δ of a measurement consisting of n uncertainty factors:

$$\Delta(\text{combined})^2 = \Delta(1)^2 + \Delta(2)^2 \cdots \Delta(n)^2 \quad (2.10)$$

When determining the uncertainty Δ of a function $f(x_1, x_2 \cdots x_n)$ of n uncorrelated variables we use the following equation:

$$\Delta^2(f) = \sum_{i=1}^n \left(\frac{\partial f}{\partial x_i} \right)^2 \cdot \Delta^2(x_i). \quad (2.11)$$

To get the uncertainty in percent we divide the equation with the function f .

2.2.3 Normal distribution

Also referred to as Gaussian distribution. Often repeated measurements are more likely to be closer to the average value than far away, and the frequency analysis will then often take the shape of a bell curve.

$$f(x) = \frac{1}{\sigma\sqrt{2\pi}} \exp^{-\frac{(x-\mu)^2}{2\sigma^2}}. \quad (2.12)$$

Equation 2.12 is the Gaussian distribution function, where μ is the average value and σ is the standard deviation. This is often referred to as the probability density function. As an illustration figure 2.3 is a plot of equation 2.12 for 1000 randomly distributed x values generated by Matlab.

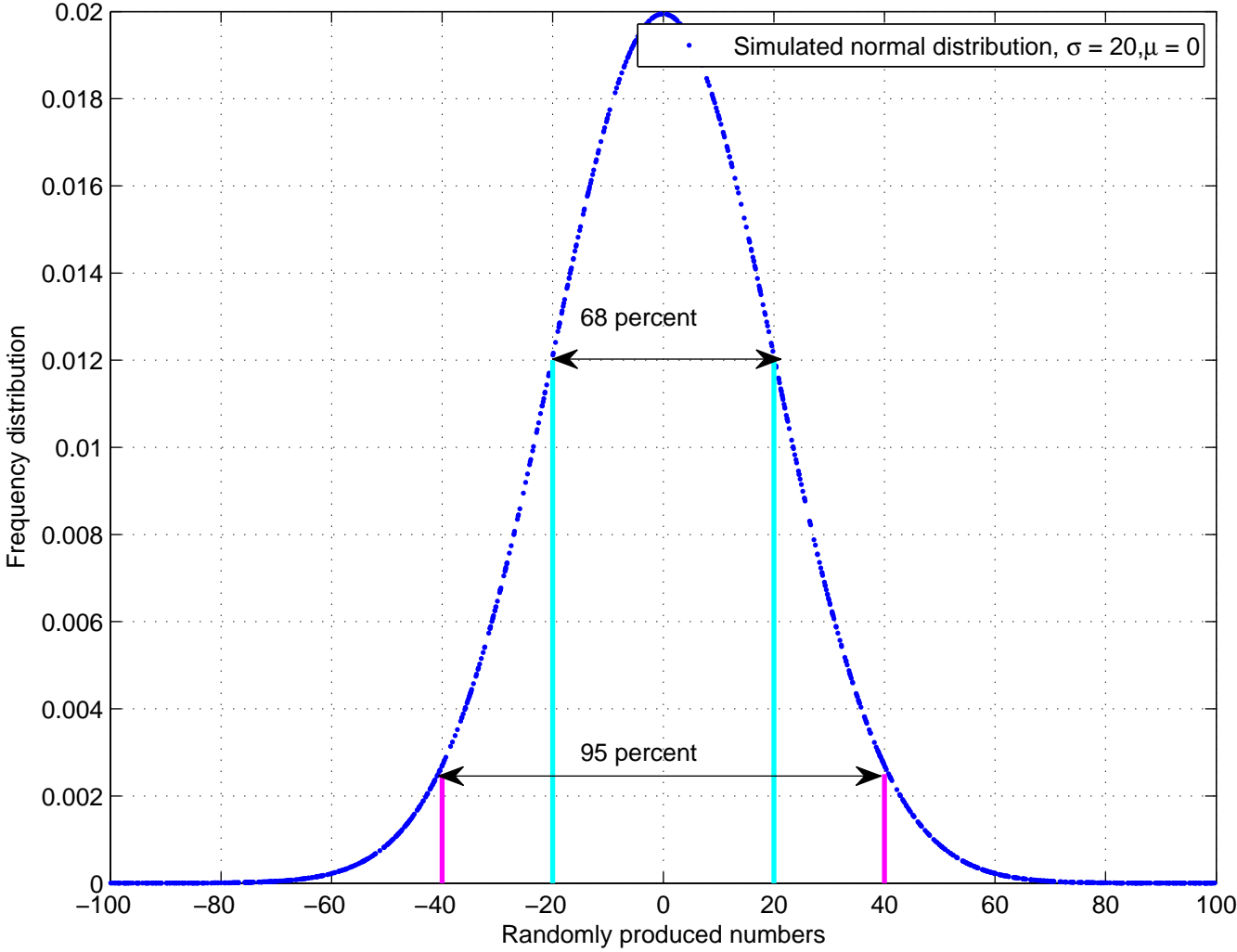


Figure 2.3: Gaussian distribution of a set of 1000 random numbers generated by Matlab. 68 percent fall within one standard deviation (cyan line) and 95 percent within two standard deviations (magenta line)

2.3 Spectrometers

The most important aspect when selecting a spectrometer is the spectral range and this is often very well documented by the manufacturer. But two other important aspects which are often not specified is the spectral resolution and the radiometric resolution. When talking about spectral resolution we often come across four different terms

1. Rayleigh criterion - Is widely accepted as the minimum requirement needed to separate two lines. The German institute for standardization (DIN) defines it as: Two lines of equal intensity are separated if the dip between the two lines are greater than 19 percent of the maximum value.
2. Line width - Full width at half maximum. To measure the width of a spectral line the expansion of that line has to be smaller than the width of the spectral line itself. So we have to know the full width at half maximum (FWHM) for the spectrometer. The FWHM is equal to 0.8 times the Rayleigh criterion.
3. Sub-pixel resolution - Is used to determine the peak wavelength and or peak intensity of a single line.
4. Pixel dispersion - Pixel dispersion is not a resolution in itself but states how close the center of the different diodes (pixels) are.

Which term is most interesting depends on what we are measuring. Three of the most common uses of a spectrometer regarding the spectral resolution are:

- Measuring a single line -> Sub pixel resolution
- Determining the shape of a line -> FWHM
- Separating different lines -> Rayleigh criterion and pixel dispersion

When talking about radiometric resolution the main areas of focus are:

- Smallest detectable change

- Stability of the signal
- The dynamic range of the detector
- Linearity

The smallest detectable change and the stability of the signal are correlated, and determine the accuracy of the sensor. The accuracy is found by doing multiple measurements of the same source and calculating the standard deviation.

The dynamic range is the ratio of noise to the maximum value the sensor can measure. And this ratio is calculated after we have removed dark current measurements and included any problems arising from data-handling. In other words the dynamic range is the maximum number of increments we can divide the signal into. To get the most increments of the signal we want to measure as close to saturation as possible.

Most modern semiconductor detectors are very close to perfectly linear (ZEISS (2011)).

3 Presenting the instruments

In this chapter we will look at information about the different types of sensors used in this thesis and how they work. We have two main categories of sensor types:

- Radiance sensors - measuring with a limited field of view
- Irradiance sensors - measuring total incoming radiance

Most of the information in this section comes directly from the manufacturer, Trios. Either from their website, one of their manuals or the software that comes with the instruments. Later we will try to reproduce some of these characteristics in a laboratory setting.

The sensors we have used are all from the Ramses type of sensor, manufactured by Trios. The Ramses instruments are hyper-spectral detectors of different types and for different spectral ranges. The detectors are designed to be versatile as they are waterproof and lightweight (less than 1 kg) which gives us a very mobile instrument. The five instruments that we had available for testing and some of their characteristics are presented in table 1.

Type	ID	Usable channels	Spectral range	Spectral accuracy	Accuracy
Radiance	804A	194	318.9 - 951.5 nm	0.3 nm	6%
Radiance	810C	194	319.1 - 951.8 nm	0.3 nm	6%
Irradiance	80FB	214	308.9- 1005.5 nm	0.3 nm	6-10%
Irradiance	80E2	194	319.5 - 951.8 nm	0.3 nm	6-10%
Irradiance	82E6	104	279.5 - 501.9 nm	0.2 nm	6-10%

Table 1: The sensors used in this thesis

The two radiance sensors are the same type of hyper-spectral detector measuring in the UV-visible range (320-1000 nm). For the irradiance sensors we have two different types. 82E6 is a UV-sensor focused in the UV-A/UV-B-range (280-400 nm) while 80FB and 80E2 measure a wider spectrum, UV-visible range (320-1000 nm), at the cost of lower accuracy.

Number of usable channels and the spectral range for the different instruments have been collected from the output of the instruments. There are some slight differences in the spectral ranges and number of usable channels. The difference in spectral range is most likely a result of the tiny differences that will occur in the production of the sensors. This difference is very small and was mostly ignored except when we calculated how much the instruments deviated from one another.

Typical uses of the TriOS Ramses instruments include:

- Monitoring water quality
- Climatology
- Confirming satellite data
- Biological experiments
- Measurements of algae concentrations
- Field measurements

3.1 Radiance sensors



Figure 3.1: RAMSES-ARC Hyper-spectral UV-VIS Radiance Sensor. From: TriOS (2012)

Radiance sensors are used when we want to measure incoming light coming from a certain direction. The sensors are generally constructed in such a way that it only can detect light coming from directions within a given cone. The opening angle of this cone is defined to as the field of view (FOV) of the instrument.

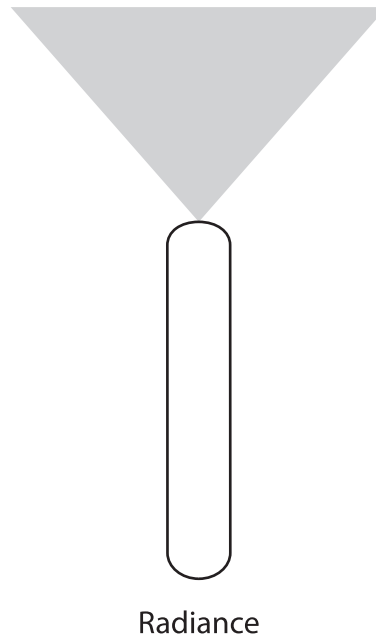


Figure 3.2: Sketch of a radiance sensor, with the field of view shown in the gray area.

In our case (Ramses-ARC) the field of view is obtained with the help of a lens placed at the front of the instrument. The lens only refracts light below a certain angle into the optical fiber. Only light entering the optical fiber will be registered by the sensor. It is possible to change the field of view if we change the position of the focal axis relative to the optical fiber. The closer the focal axis is to the optical fiber the smaller the field of view.

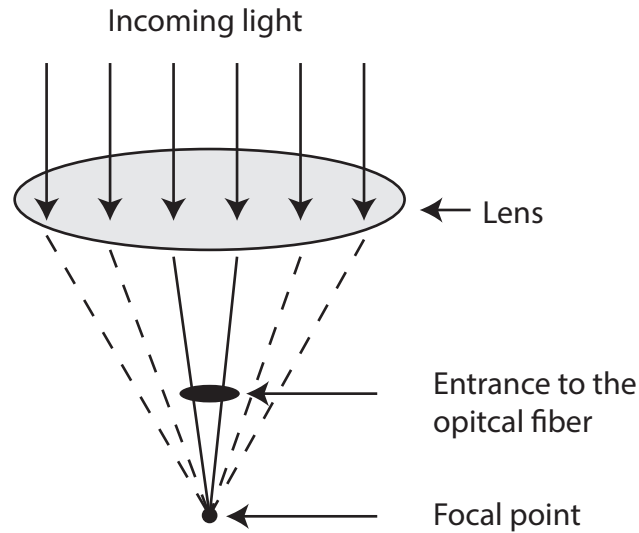


Figure 3.3: Illustration of the optics of the Ramses radiance sensors.

In figure 3.3 we see that if the focal point is too far to either side no light will reach the entrance to the optical fiber. Thus creating the field of view of the sensor.

The radiance sensors give output as power per solid angle per projected source area per wavelength

$$\frac{mW}{(m^2 \cdot nm \cdot Sr)}$$

3.1.1 Technical data of the radiance sensors

- Optical:
 - wavelength range*: 320 - 950 nm
 - detector type*: 256 channel silicon photo-diode array
 - spectral sampling*: 3.3 nm/pixel
 - spectral accuracy: 0.3 nm
 - usable channels: 190
 - typical saturation (at): $1000mW/(m^2 \cdot nm \cdot Sr)$
- Detection:

- field of view: 7° in air (can be optimized)
- accuracy: better than 6% (depending on spectral range)
- Electrical:
 - integration time: 4 ms - 8 sec (user selectable or auto [4 ms - 4096 ms])
 - elementary data interface: RS232 or Serial Bus
 - data rate (RS232): 1,200 - 19,200 baud
 - power requirements: 1.5 - 11 VDC
 - * 0.85 mW (data acquisition active)
 - * 80 mW (interface active)
 - * 0.5 mW (stand-by modus)
 - connector: SubConn micro 5 pin male
- Physical:
 - size: Ø4.83 cm x 29.7 cm (without connector)
 - weight in air: 1.0 kg (stainless steel / POM housing)
 - depth range: 300 m
 - operating temperature: -10°C to +50°C

* specifications from Carl ZEISS, Germany

3.2 Irradiance sensors

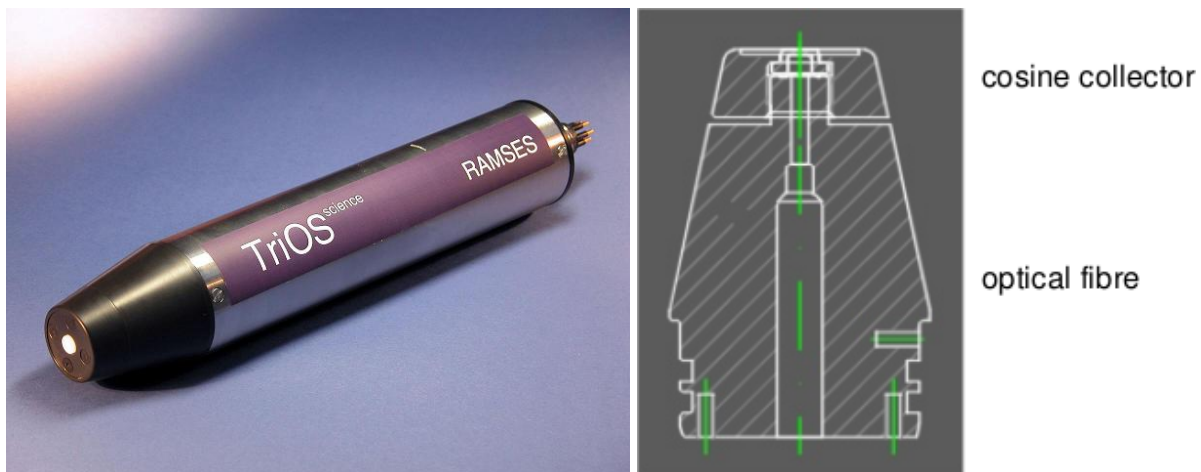


Figure 3.4: RAMSES-ACC-VIS Hyper-spectral UV-VIS Irradiance Sensor. From TriOS (2012).

When we want to measure the total radiation incoming at a surface we use irradiance sensors. Irradiance sensors are made to register light from all incoming angles, and this places some strain on the detector as to light coming in at different angles has to be registered in the correct way. Constructing ideal optics for collecting the light has proven to be a difficult task (Zibordi and Bulgarelli (2007); Bais et al. (1998a); Michalsky et al. (1995); Grainger et al. (1993)). Which is why we have chosen to take extra care in thoroughly testing this part of the instrument. The radiance incoming at the surface can be expressed as a function of the angle between the normal of the surface and the incoming radiance (see equation 2.8). This is known as Lambert's cosine law. Which for a perfect instrument has to be true for all incoming angles. The geometry of Lambert's cosine law is illustrated in figure 2.2.

The Trios Ramses irradiance sensors uses a white cosine collector made out of fused silica, placed at the front of the instrument to diffuse the light into the optical fiber behind it. The output of the irradiance sensors is given as power incident on a surface per wavelength

$$\frac{mW}{(m^2 \cdot nm)}$$

3.2.1 Technical data for the irradiance sensors

- Optical:
 - wavelength range*: 320 - 950 nm
 - detector type*: 256 channel silicon photo-diode array
 - spectral sampling*: 3.3 nm/pixel
 - spectral accuracy: 0.3 nm
 - usable channels: 190
 - typical saturation (4 ms integration time):
 - * $10Wm^{-2}nm^{-1}$ (at 400 nm)
 - * $8Wm^{-2}nm^{-1}$ (at 500 nm)
 - * $14Wm^{-2}nm^{-1}$ (at 700 nm)
 - typical NEI (8 sec integration time):
 - * $0.4\mu Wm^{-2}nm^{-1}$ (at 400 nm)
 - * $0.4\mu Wm^{-2}nm^{-1}$ (at 500 nm)
 - * $0.6\mu Wm^{-2}nm^{-1}$ (at 700 nm)
- detection
 - collector type: cosine response
 - accuracy: better than 6%-10% (depending on spectral range)

- Electrical:
 - integration time: 4 ms - 8 sec (user selectable or auto [4 ms - 4096 ms])
 - elementary data interface: RS232
 - data rate (RS232): 1,200 - 19,200 baud
 - power requirements: 1.5 - 11 VDC
 - * 0.85 mW (data acquisition active)
 - * 80 mW (interface active)
 - * 0.5 mW (stand-by modus)
 - connector: SubConn micro 5 pin male
- Physical:
 - size: Ø4.83 cm x 26 cm (without connector)
 - weight in air: <1.0 kg (stainless steel / POM housing)
 - depth range: 300 m
 - operating temperature: -10°C to +50°C

* specifications from Carl ZEISS, Germany

3.3 The inner workings of the instruments

The instruments are pretty much the same on the inside. They use the spectrometer mms1 from Zeiss. The main difference is in how many diodes which are active, and what part of the spectrum which is reflected to these diodes. As mentioned earlier the radiance sensors only collects light from a specific field of view, and the irradiance sensors collects light from all angles.

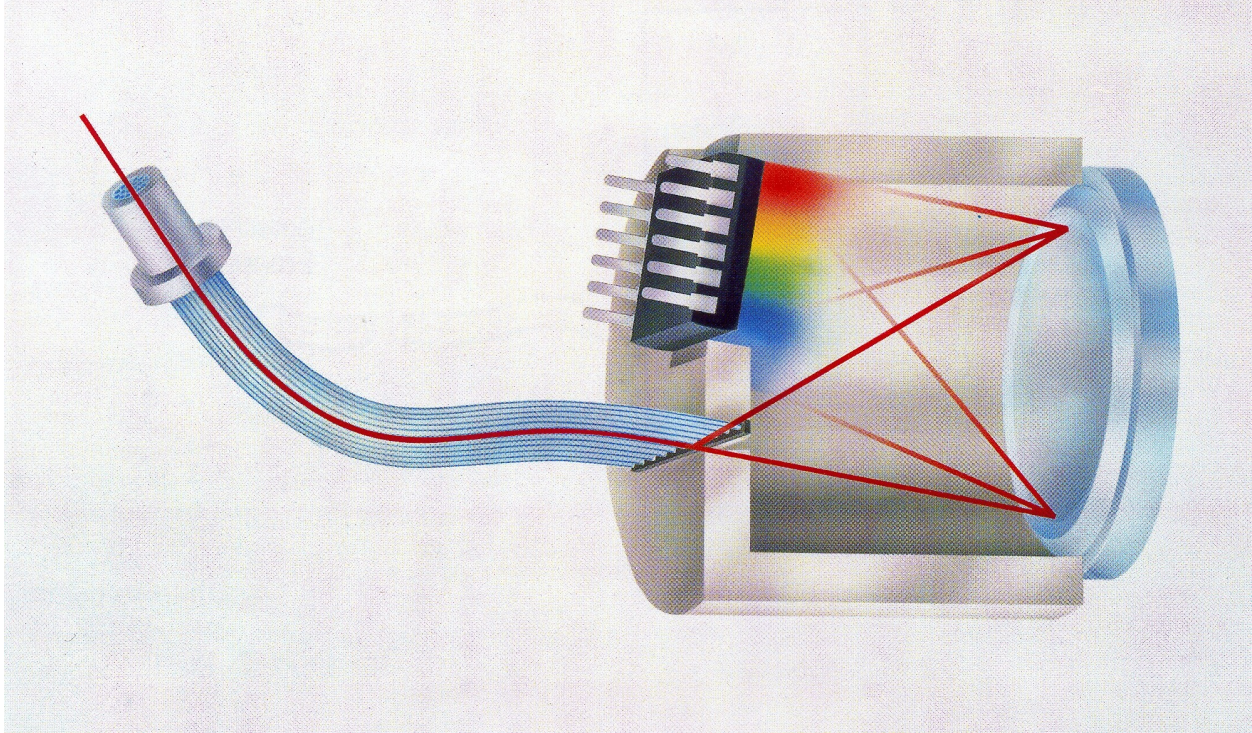


Figure 3.5: The layout of the Zeiss mms1 spectrometer. From: TriOS (2012).

If we follow the path of the light as shown in figure 3.5. The optics in the front of the sensor collects the light into the optical fibre then the light will hit the holographic grid. Which works like a diffraction grating separating the different wavelengths of the light. After being separated the light hits an array of 256 photo-diodes. Different wavelengths are directed to different diodes. And finally small circuit boards gives out the electrical output to the outside world (computer, data-logger etc.). The distance from the holographic grid to the diodes are designed to let light with one wavelength hit more than one diode giving us some overlap for some wavelengths, this reduces the chance of some wavelengths not registering at all but at the same time reduces the resolution or the ability to separate different lines when looking at a spectrum.

3.4 Data handling

Typical output from a sensor measuring the spectrum from a standard 100 W calibration lamp is shown in figure 3.6:

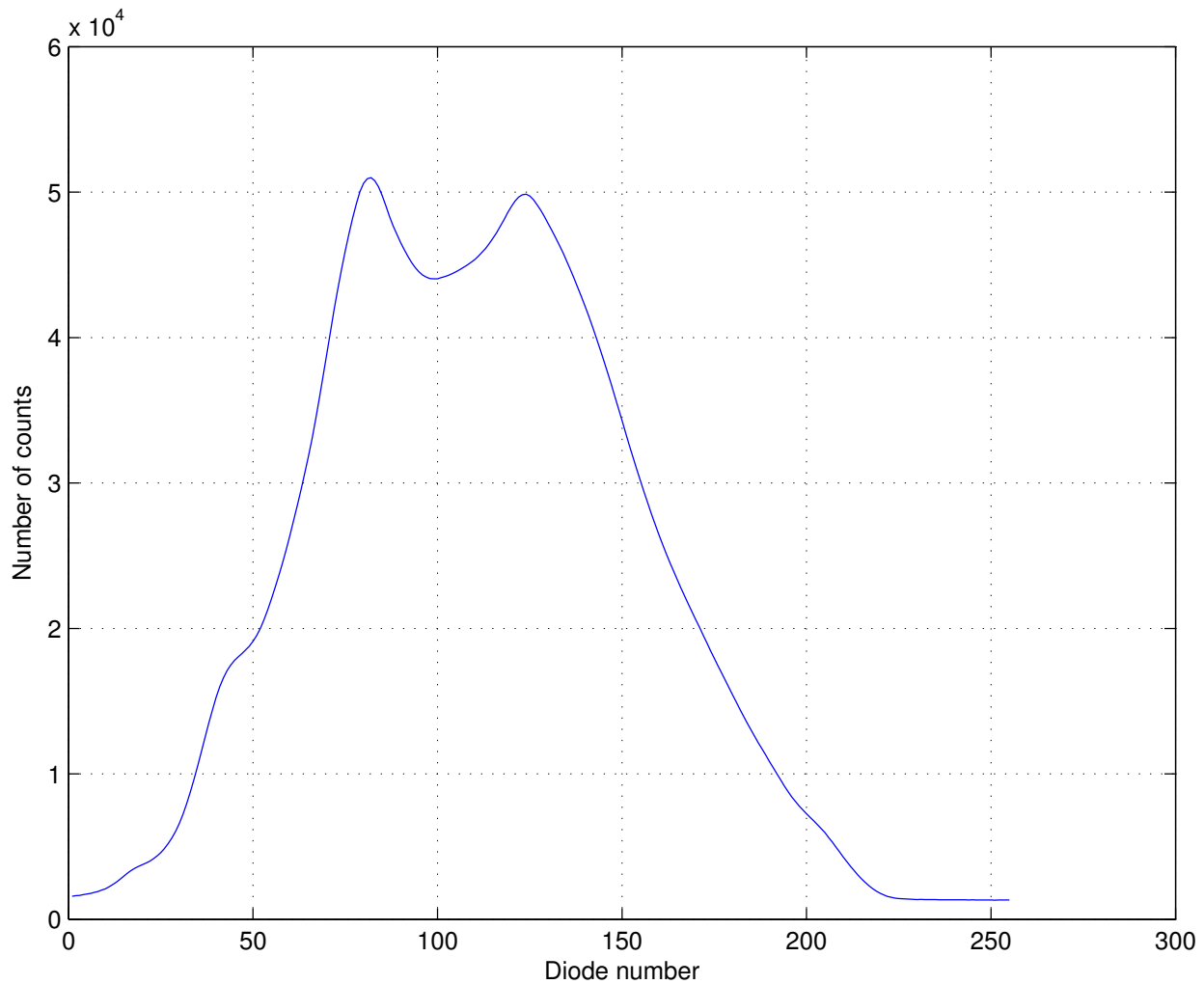


Figure 3.6: Example of the raw output from the 80E2 irradiance sensors when measuring light from the standard calibration lamp used in our laboratory experiments.

The output from the sensor is given as number of counts. Since this is not very useful without more information we want to convert number of counts to $\mu\text{W}/\text{m}^2/\text{nm}$. To convert the output to the desired units we need to know which diodes register which wavelengths and the sensitivity of the different diodes. Initially this is measured at the manufacturer

of the spectrometer, Carl ZEISS, but the instruments will require recalibration about once a year to remain accurate. Although there will be complications when trying to separate two lines that are closer than the resolution. In some cases this can be overcome, for instance if the incoming radiance is known to be only one wavelength (e.g. laser) the output registered by the sensor will be in the shape of a Gauss curve centered at the incoming wavelength. Which gives us the possibility to achieve higher spectral accuracy.

Dark current handling is important for instrument measuring light and it varies with temperature and integration time. The solution chosen for the Zeiss mms1 is that a portion of the 255 diodes are kept dark at all times, and used to measure the dark current for each separate measurement. Although this means that these diodes can never be used for measuring the light directly it has the advantage of less movable parts compared to the often used solution where a dark "wall" is used to obstruct the light, and then moved back and forth. For the mms1 this means one less thing that can break down, and longer lifetime for the instrument. In figure 3.6 diodes number 198 and above are used for dark current measurements.

There are some calculations necessary to get from raw data to irradiance. We need to import the correct calibration files, and the software will do all of the calculations for us. After processing the raw data we get the desired irradiance output of $mW/(m^2 \cdot nm)$. A typical spectrum is shown in figure 3.7. Here we used the raw data plotted in figure 3.6.

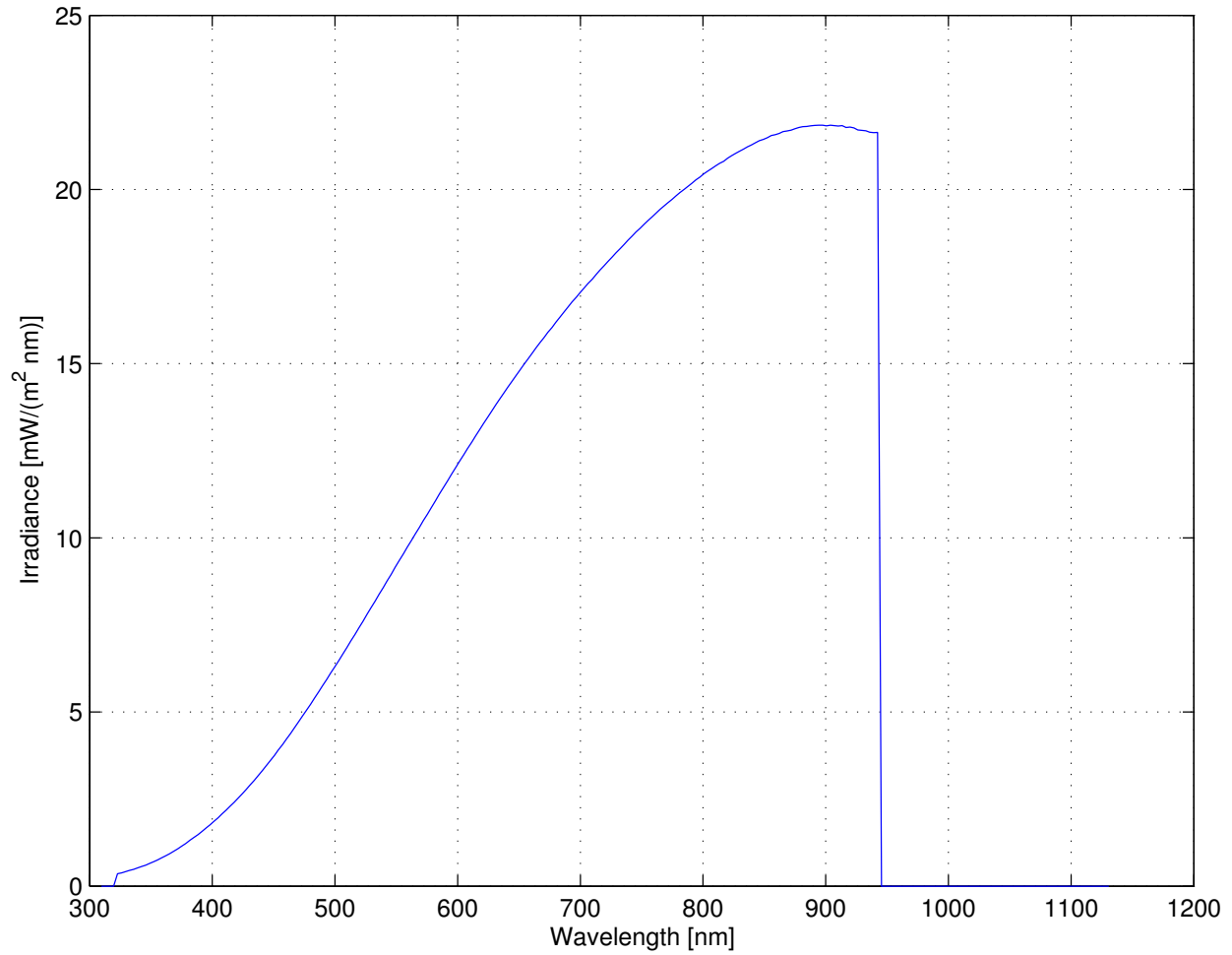


Figure 3.7: Example of calibrated spectrum from the raw data plotted in figure 3.6. Measurement of the calibration lamp used in the laboratory by the 80E2 irradiance sensor.

In figure 3.7 we see that the spectrum closely resembles Planck's law for black body radiation.

4 Data collected in the laboratory

In this section we will analyze some of the responses of the different instruments in a laboratory setting. The main areas that we will examine are:

- Spectral accuracy
- Field of view of the radiance sensors
- Cosine response of the three irradiance sensors
- Comparisons of the different sensors
- Uncertainty of the measurements

4.1 Setup

For all the measurements done in the laboratory we used the same setup:

- All of the equipment was mounted on an optical table.
- As a light source we used a standard 100 W calibration lamp.
- The different sensors were mounted on top of an optical breadboard rotating table from Thor labs. (It is much easier to accurately measure the angle when rotating just the sensor and keeping the lamp at a fixed position than the other way of moving the light source.)
- The rotating table and the calibration lamp was kept at fixed positions on the optical table. Leaving only the position of the sensor as a variable in the geometry of the setup.
- To ensure that the sensor was located exactly in the center of the rotating table a laser was aligned from the lamp to the sensor, then the sensor was carefully adjusted in such a way that when rotating the sensor the laser was always pointing directly at the center of the sensor, for all angles.

- To reduce any stray light that might have interfered with the experiments we put a black box with a small square opening over the calibration lamp and a sun-blocking curtain around the table.

The distance from the center of the sensor to the center of the lamp was measured to be 50.3 cm.

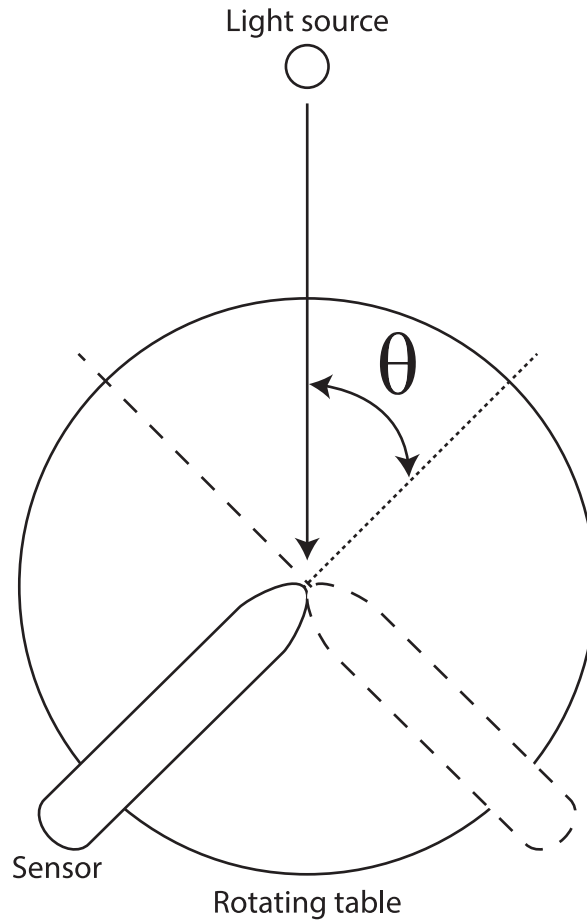


Figure 4.1: Illustration of the setup used for the measurements performed in the laboratory (showing the other rotating side in dashed lines). θ is the angle between the normal of the sensor and the incoming light.

In total we have five instruments, two radiance sensors (810C and 804A) and three irradiance sensors (80FB, 80E2 and 82E6). One of the irradiance sensors is a UV-sensor (82E6). As much as possible we have used all the instruments in all the tests. All of the instruments and their characteristics are listed in table 1, and will be referred to by their ID

number.

A quick note on all the measurements: The output of the sensor is an array with the center wavelengths of the diodes and the measured irradiance at those wavelengths. In most of the graphs where the entire spectrum is plotted, these points are drawn as a continuous line instead of several points. This style in the graphs was chosen because of the many points (about 190) in each line, and plotting all of the points would clutter up the graphs.

We measured each separate setting (e.g cosine response at 60°) 3-4 times, and used the average value in the data analysis. To reduce the chance of human/instrumentally induced change in the setup, we measured each characteristic of the sensor (e.g. cosine response of one instrument) in a short time interval without turning anything on or off. All of the instruments showed high degree of repeatability both for human and machine variables during a single cycle of measurements (see section 4.6). A recurring theme in all of the measurements was the big variations for wavelengths shorter than 400 nm. This might be a result of the much lower power output of the calibration lamp in this area (see figure 3.7), which could lead to lower saturation in those diodes and thus higher uncertainty. However it indicates that we need the more specialized UV-sensor (82E6) for precise measurements in this region.

4.2 Spectral accuracy

The laser used to align the setup of the experiments is a DPGLA 532.0 nm green laser. The combination of a given line width of less than 0.1 nm (need accurate input to the sensor to accurately measure the accuracy of the sensor), and the option to adjust the power (to avoid over-saturation) makes this laser a good tool for measuring the bandwidth and spectral accuracy of our sensors. The 532.0 nm output from the laser is outside the range of the UV sensor, so it was not included in these tests.

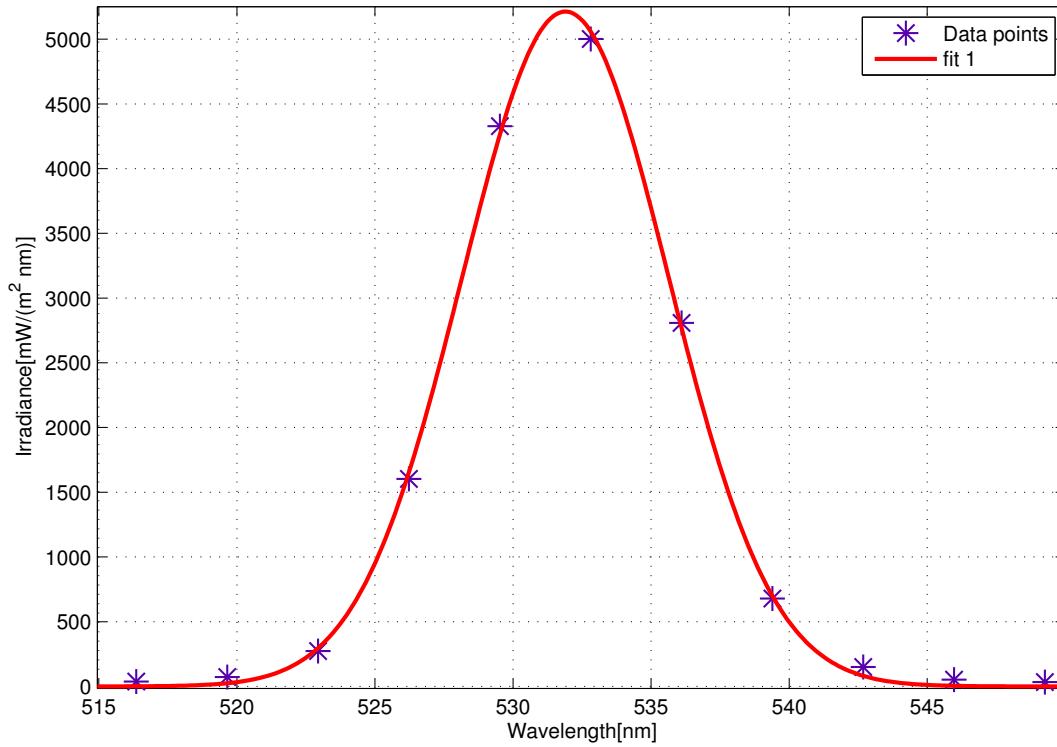


Figure 4.2: The spectrum (data points) of a 532.0 nm wavelength laser, and a Gaussian fit applied to the data points.

Figure 4.2 shows a Gaussian bell curve fitted to the the spectrum measured by the 80FB irradiance sensor. A Gaussian function is described by equation 4.1:

$$E(\lambda) = a * \exp(-((\lambda - \lambda_0)/\sigma)^2), \quad (4.1)$$

where a is the peak of the curve, λ_0 is the position of the center and σ is the standard deviation. When fitted to our results, this gives us the coefficients from equation 4.1 are presented in table 2.

Since there is only a manual adjustment available we can not be sure of the power output of the laser so a is not interesting at this point, and is most likely measured differently by the two sensor because the measurements were not made with the same power output of the laser. The center of the curve, λ_0 , at 531.9 nm for both instruments, is 0.1 nm away

	80FB	80E2
Peak of the curve [nm]	5214 (5190, 5238)	5707 (5675, 5738)
Position of the center [nm]	531.9 (531.9, 531.9)	531.9 (531.9, 531.9)
Standard deviation [nm]	5.29 (5.26, 5.32)	5.16 (5.13, 5.19)
Full width at half maximum [nm]	12.45 (12.39, 12.51)	12.15 (12.07, 12.22)
Rayleigh criterion [nm]	15.56 (15.49, 15.64)	15.19 (15.09, 15.28)

Table 2: Calculated characteristics from the measurement of a 532.0 nm laser for the two irradiance sensors. 95 percent confidence intervals in parenthesis

from the input of 532.0 nm. We considered this as a good result and consistent with the reported spectral accuracy of 0.3 nm. σ can be used to calculate the full width at half maximum (FWHM) for the Gauss curve, which in literature often is referred to as the bandwidth of a sensor:

$$FWHM = 2\sqrt{2\ln 2} \cdot \sigma, \quad (4.2)$$

The Rayleigh criterion is the requirement for separating two different lines and is related to the FWHM:

$$\text{Full width at half maximum} = 0.8 \text{ Rayleigh criterion}$$

For both irradiance sensors the Rayleigh criterion was calculated to be close to 15 nm. Meaning that the two irradiance sensors will face challenges when trying to measure structures in the spectrum that are finer than 15 nm.

4.3 Determining the field of view of a radiance sensor

To determine the field of view of the 804A radiance sensor it was mounted on the rotating table, and we measured the radiance for every 0.5° rotation of the sensor until the radiance dropped to zero. 0° is defined as the position where the light-beam is shining directly into the instrument. We rotated the instrument to both sides first to one side than to the other as a control of the setup. If there is any difference between the measurement results from either the left or the right side there might be an azimuthal dependence in the sensor, or more likely, some error has been made in the alignment of the sensor and/or the calibration lamp. Some differences between the two sides was found but nothing major. Indicating no big problems in the setup of the experiment. To reduce the uncertainty

of the angle we used the average value of both rotating directions. This approach was used for all angles measured. With the assumption that there is a very low azimuthal dependence in the sensors, the field of view will be the same in all directions.

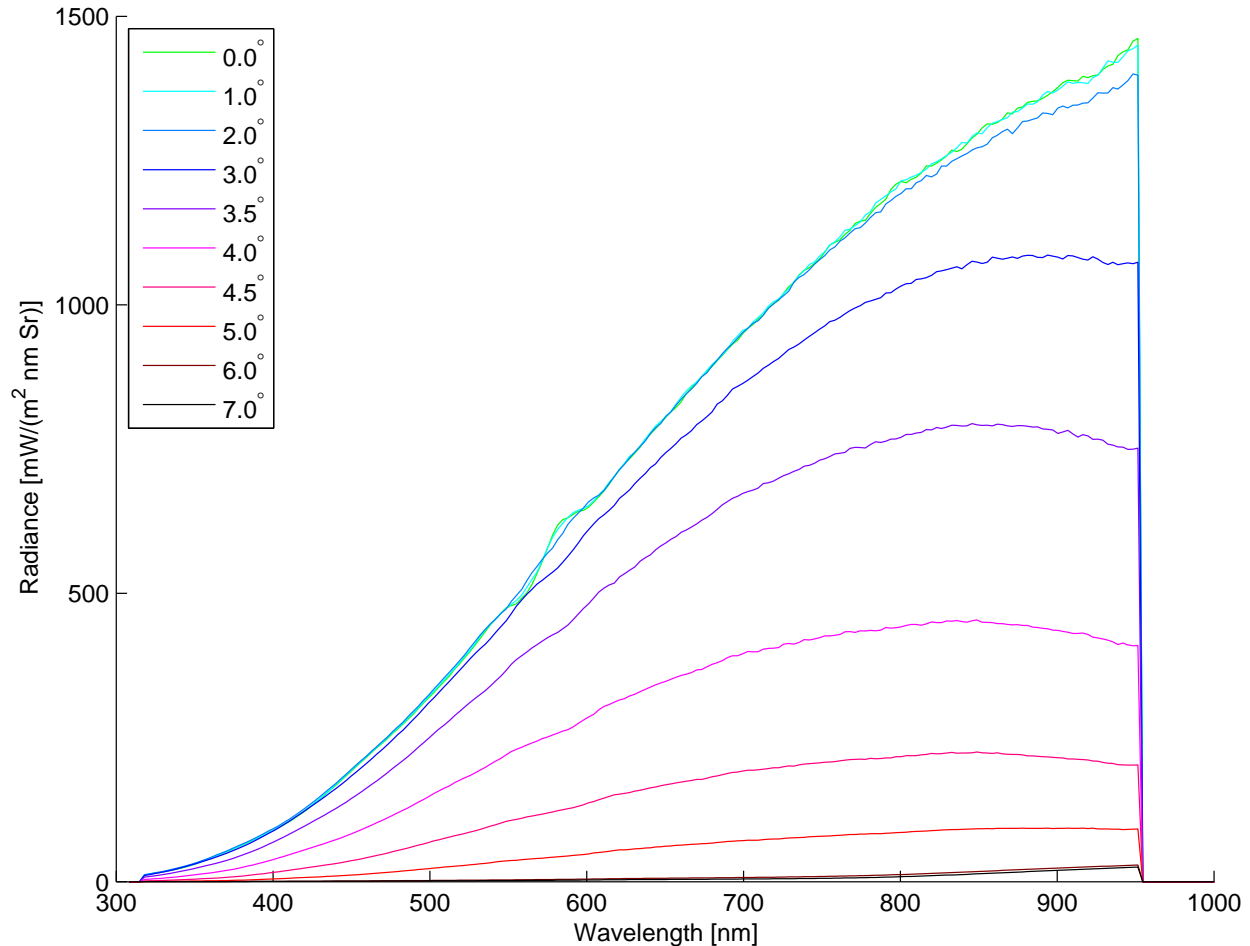


Figure 4.3: Plots of the different spectra measured by the radiance sensor 804A at different angles

Figure 4.3 shows the different spectra measured for the different angles. Most of the wavelengths behave in more or less the same fashion, but the radiance drops off slightly faster at the longer wavelengths. To get a clearer idea of where the drop in radiance becomes significant we take a look at the drop in radiance as a function of angle for a few sample wavelengths instead of the whole spectrum.

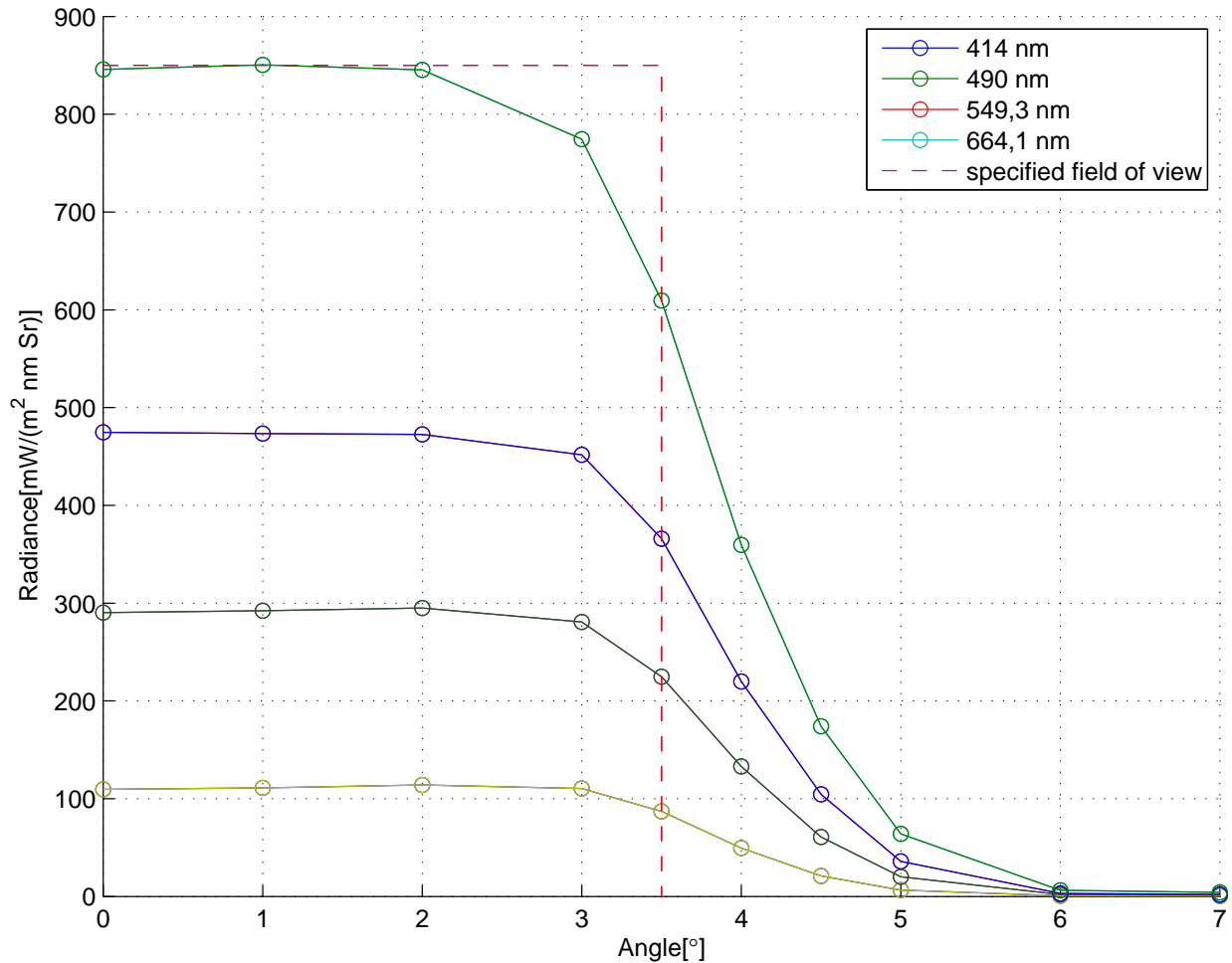


Figure 4.4: Radiance as a function of the angle between the normal and the incoming light for four selected wavelengths. Specified field of view determined as a theoretical 100% radiance inside, 0% outside the manufacturer’s specified field of view of 7°.

We see in figure 4.4 that the radiance is almost constant up to 2° for all wavelengths, for larges angles it starts to drop off, and at 6° it is close to zero for all wavelengths. This is somewhat consistent with the given field of view of 7° from the manual of the sensor, which in theory should give us output of 100% radiance up to 3.5° in all directions and 0 percent over 3.5°. Unfortunately this is unobtainable due to the optics of the instrument. The instrument is designed in such a way that the the focal point of the lens is behind the entrance of the optical fiber (see figure 3.3). This means that as the angle of the incoming light changes the same amount of light will illuminate the fiber, and we will measure the same radiance until we start to approach the cutoff point. Close to the cutoff point there

will be some angles where the light is refracted in a way that illuminates just part of the optical fiber. The entrance to the optical fiber is not a single point but has a defined radius of 0.5 mm. This explains why the radiance is not suddenly dropping from 100% to 0% but gradually falls off.

We defined our measured field of view by comparing the total radiance for all angles measured by our sensor and the total radiance a theoretical sensor would have measured. Assuming that the light is isotropic around the cutoff angle, we can solve equation 4.3 to determine the effective cutoff angle of the radiance sensor:

$$\int_0^{\pi} E_{measured}(\theta) d\theta = E_0 \cdot \theta_c, \quad (4.3)$$

where E_0 is the radiance measured at 0° and θ_c is our cutoff angle. The effective field of view of the instrument is then given as $2 \cdot \theta_c$. In figure 4.5 we have plotted this calculated field of view for all the wavelengths in the range of the sensor.

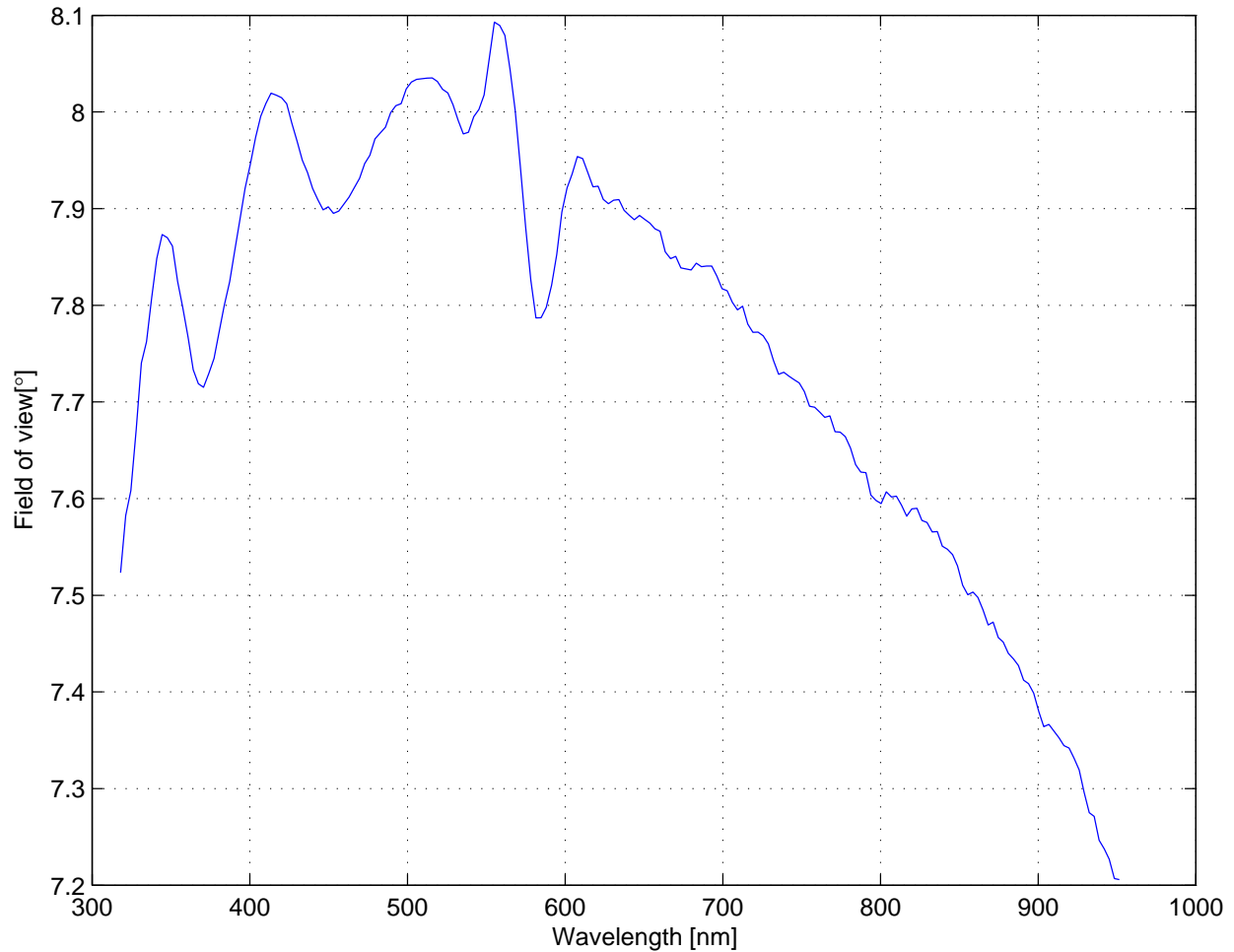


Figure 4.5: Calculated field of view from equation 4.3 of the 804A radiance sensor for all wavelengths in its range

Figure 4.5 shows around 0.8 degrees larger field of view than the one specified in the manual of 7 degrees. At this time it is not certain if this is due to a difference in how we have calculated the field of view or measurement methods between the manufacturer and the one we have chosen. There is a difference in the field of view for the different wavelengths. Since most materials have a wavelength dependent index of refraction this is as expected as the different wavelengths will be refracted differently by the lens. Different focal points for different wavelengths are produced because different wavelengths of light will behave differently when traveling through the lens. Different focal points give rise to different fields of view. This phenomenon is a common problem in optical systems, as shown by Sun et al. (2010), and is known as lateral chromatic aberration.

4.4 Cosine response of the 80FB and 80E2 Irradiance sensors

The setup described in section 4.1 with the instruments on the rotating table was also used in the measurements of the cosine response. We measured the spectra with the sensor looking straight into the calibration lamp and rotated the sensor in increments of 10° up to 60° and then in steps of 5° until 85° . This process was done for both rotating directions. The spectrum was recorded for each step. To account for any stray light that might have influenced the experiment we measured the light at 95° and defined this as the constant light-pollution present in the room, and subtracted this value from all of the measurements done at the other angles. On closer examination of this light-pollution spectrum, we noticed that it was practically zero for all of the visible light spectrum (400-700 nm), but had a slight effect on the infrared region (700-1000 nm). It is not entirely sure what caused this "pollution", but a likely explanation is that the dark cardboard and curtains placed around our experiment were slightly reflecting at infrared wavelengths. For every angle we have used the average value of the two rotating directions.

We calculate the error in the cosine response by comparing the measured radiance at different angles to the ideal Lambertian cosine response

$$E_{ideal}(\theta) = E_0 \cdot \cos(\theta), \quad (4.4)$$

where E_0 is the irradiance at normal incidence, and θ is the angle between the incoming light and the normal. The cosine response error ϵ in percent for all the wavelengths can now be calculated as a function of θ :

$$\epsilon(\theta) = \left(\frac{E_{measured}(\theta) - E_{measured}(95^\circ)}{E_{ideal}(\theta)} - 1 \right) \cdot 100\%, \quad (4.5)$$

where $E_{measured}(95^\circ)$ is the measurements of stray light in the laboratory (see figure 4.19 for detailed spectrum).

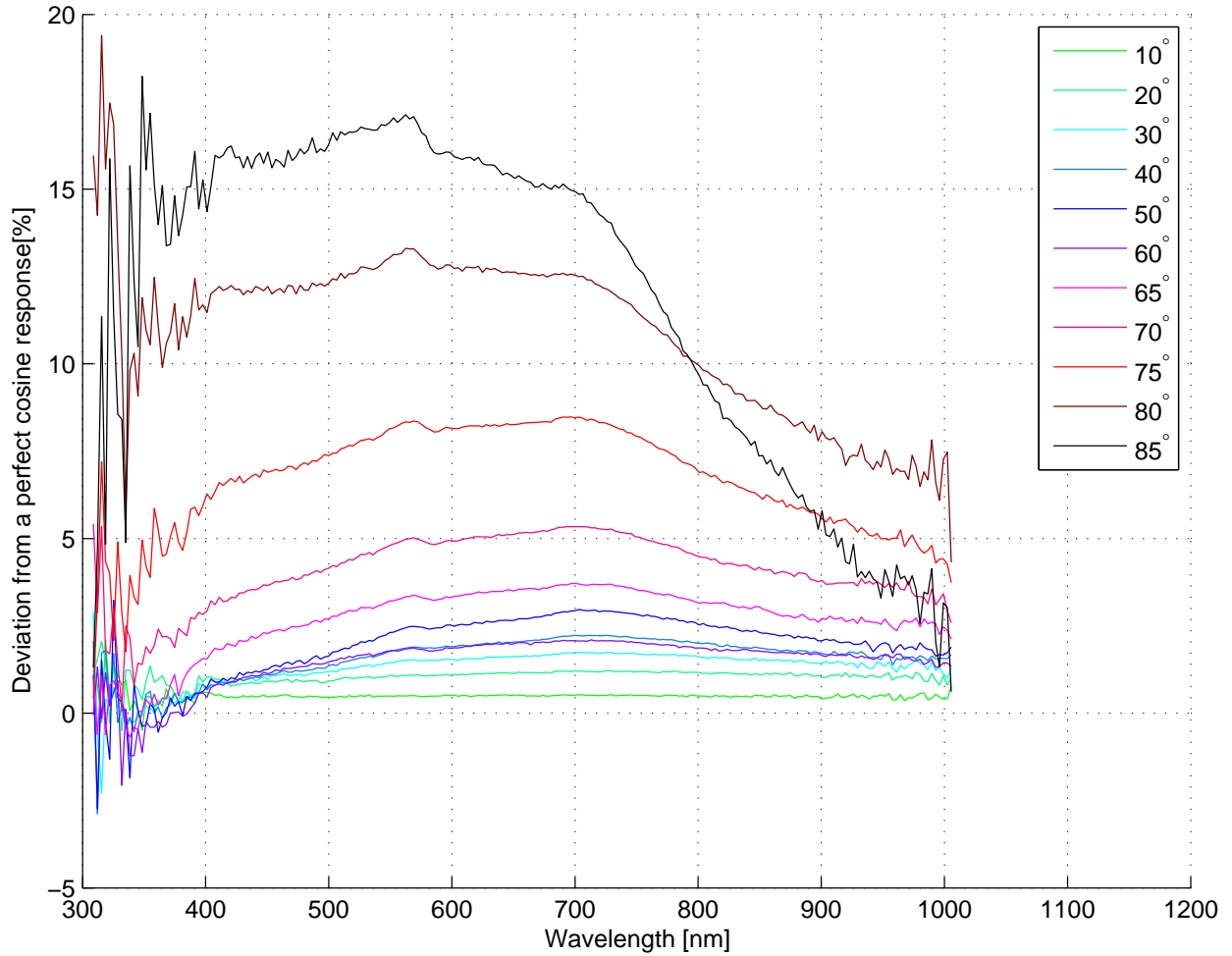


Figure 4.6: The cosine response error, $\epsilon(\theta)$, in percent, of the 80FB irradiance sensor at light coming in at various angles, for all of the wavelengths in its range

Figure 4.6 shows the cosine response error, in percent, compared to an ideal cosine response. A positive value indicates that the instrument is measuring too much light, and negative value indicates too little light. Only the measurements done at 80° and 85° are outside the 7-10% uncertainty range given by the manufacturer TriOS (2012). We suspect that the optics in the light collector is the main contributor to this error. Another option is to use the measurements to calculate a correction factor

$$C(\theta) = \frac{E_{ideal}(\theta)}{E_{measured}(\theta) - E_{measured}(95^\circ)} \quad (4.6)$$

for the different incoming angles, which can be used to improve the measurements as

long as $E(\theta)$ is known. With no azimuthal dependence this means that for isotropic light, one can integrate $\epsilon(\theta)$ over all of the angles to get a total error:

$$\epsilon_{isotropic} = \frac{1}{\pi} \int_0^{2\pi} \int_0^{\pi/2} \epsilon(\theta) \cos\theta \sin\theta d\theta d\phi, \quad (4.7)$$

for our two irradiance sensors, that would mean about 2-3% over estimation of the total irradiance, with a slight dependence on the wavelength of the incoming light. This error is consistent with the 7-10% accuracy given by Trios TriOS (2012). Figure 4.7 shows a plot of equation 4.7 for the entire spectrum of wavelengths in the sensor range.

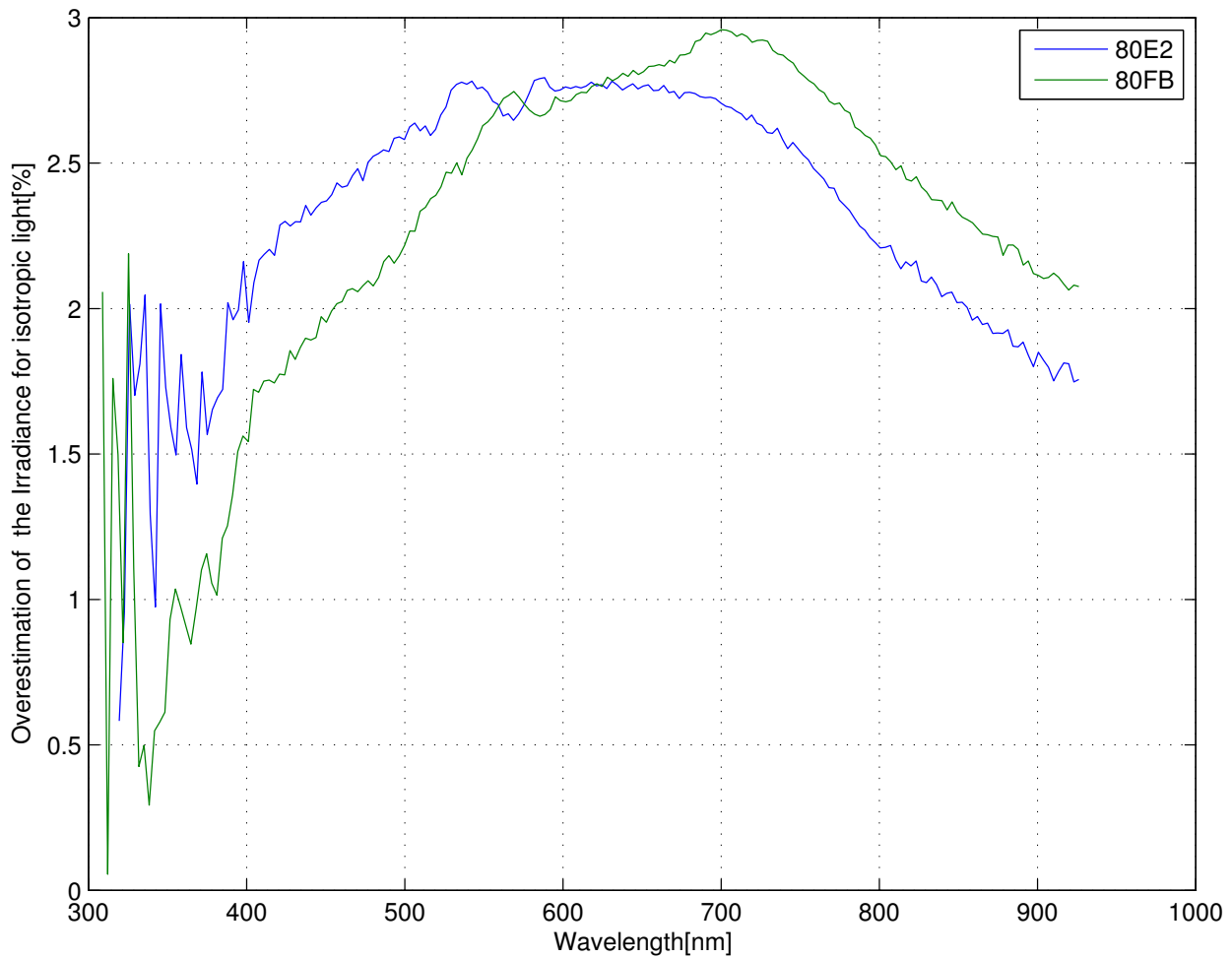


Figure 4.7: Calculated $\epsilon_{isotropic}$ for the entire spectrum of the two irradiance sensors 80FB and 80E2

$\epsilon_{isotropic}$ is the same value as DIN5032 as given by the German Institute of Standardiza-

tion. DIN5032 is used as an index of the quality of the cosine response. Our findings of below 3% error for both irradiance sensor are acceptable results and better than many commercially available sensors that often show above 4% error, even with corrections as documented by Bernhard and Seckmeyer (1997) and Gröbner (2003).

When doing measurements out in the field, the incoming solar radiation will not be isotropic but also include a direct part. If we are able to either by measuring, or with the use of a model, to determine which fraction of the radiation comes from the direct part and what part of the solar radiation is isotropic, we can use our measurements of the cosine response error to make corrections to the original measurements.

The diffuse light is in general not entirely isotropic and to take this into account will require more complicated calculations and better modeling of the solar radiation than used in this thesis. As we will show in chapter 6, the biggest problem when applying these corrections to the field measurements comes from the uncertainty in alignment of the sensors. If the instrument instead of being completely vertical is tilted just a couple of degrees towards or away from the sun it will give significantly different results.

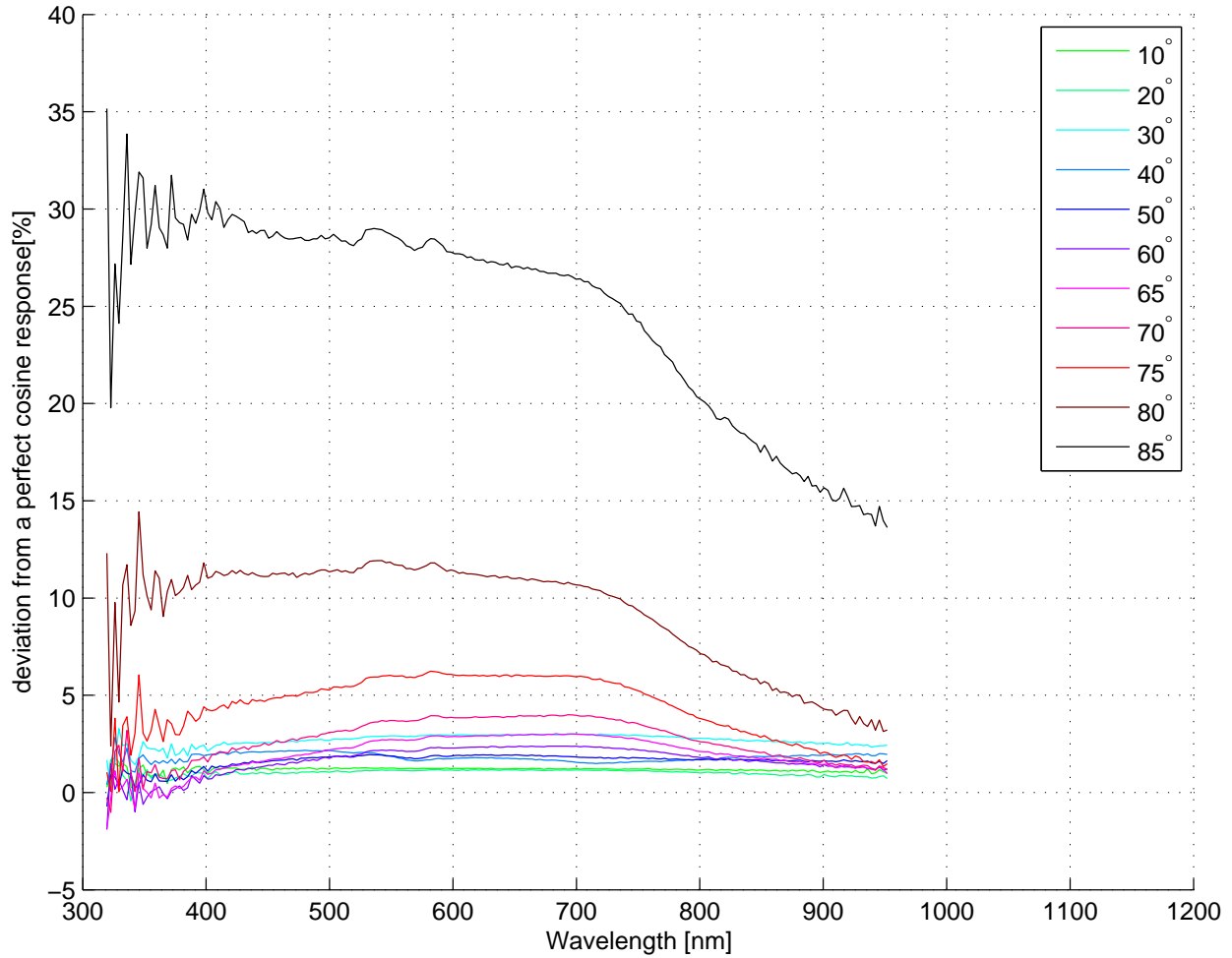


Figure 4.8: The cosine response error, $\epsilon(\theta)$, of the 80E2 irradiance sensor at various incoming angles of light, in percent, for all of the wavelengths in its range.

Figure 4.8 shows the measured cosine response error, $\epsilon(\theta)$, for the 80E2 irradiance sensors. We found a similar cosine response error as the 80FB with quite accurate results for angles between the normal and the incoming light of lower than 80° . The fact that we find similar cosine response errors for both instruments suggests that we are getting results close to the actual cosine response of the sensors.

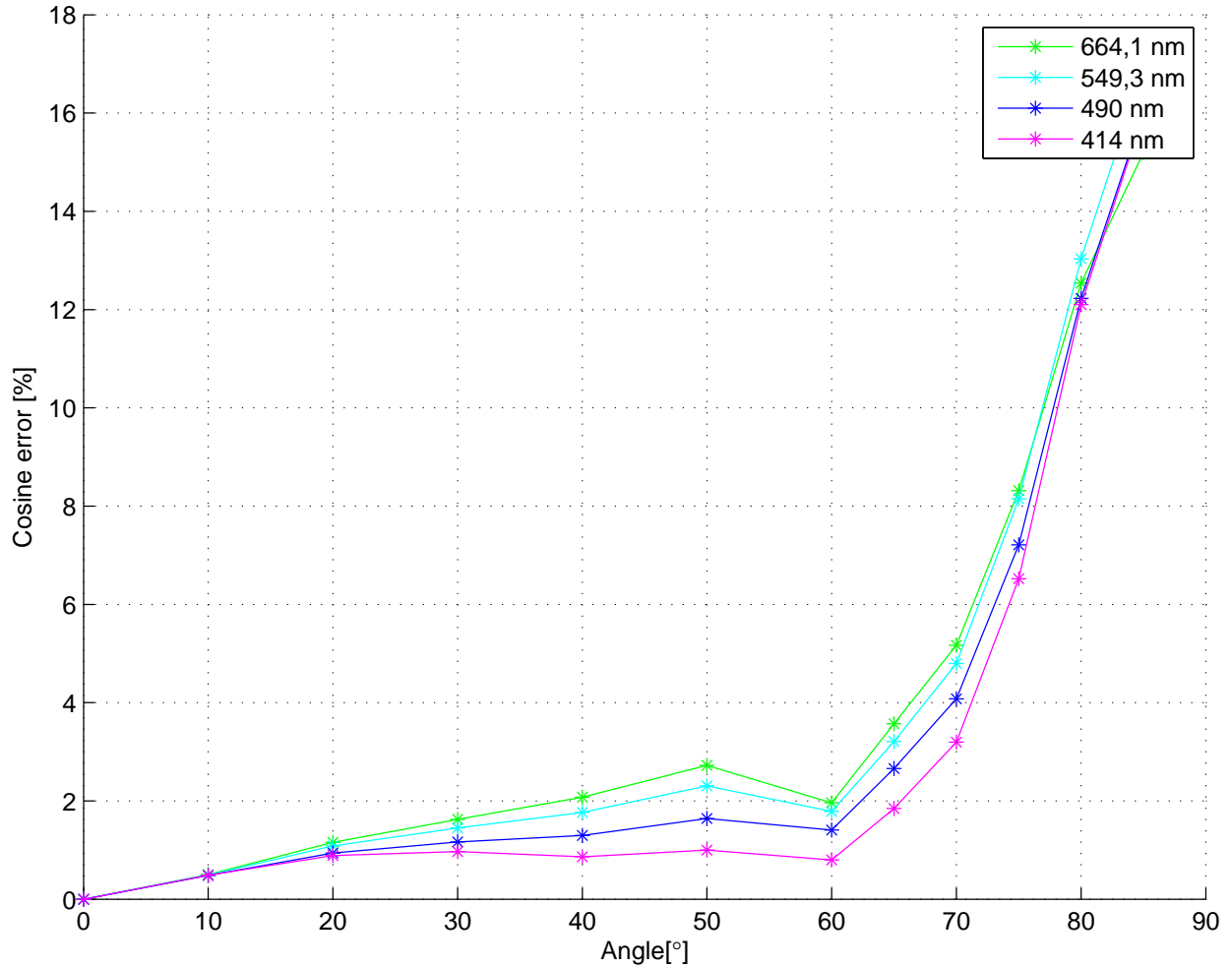


Figure 4.9: The cosine response error $\epsilon(\theta)$ as a function of the angle between the normal and the incoming light. Presenting four selected wavelengths of the light. As measured by the 80FB irradiance sensor.

As with most results there are several ways to present the same data. We will now look at a couple of alternative ways of presenting the cosine response error of an instrument. The main motivation for making these graphs was to make it easier to compare our results with the ones we could find in other papers. All of the different styles of graphs use the same data for the same instruments, but highlight different areas of the results. Figure 4.9 and figure 4.10 shows common ways of presenting the error in the cosine response similar to the ones found in Zibordi and Bulgarelli (2007), Bais et al. (1998a), Bais et al. (1998b) and Grainger et al. (1993), but showing only four selected wavelengths. Our results are

comparable to the results for the radiometers studied in Zibordi and Bulgarelli (2007). However some of the wavelengths are more accurate and others are less accurate. Note that the percentage error increases fast as the angle increases towards 90 degrees. Even small changes in the absolute value will give a huge percentage error, since the ideal cosine response approaches zero at 90°.

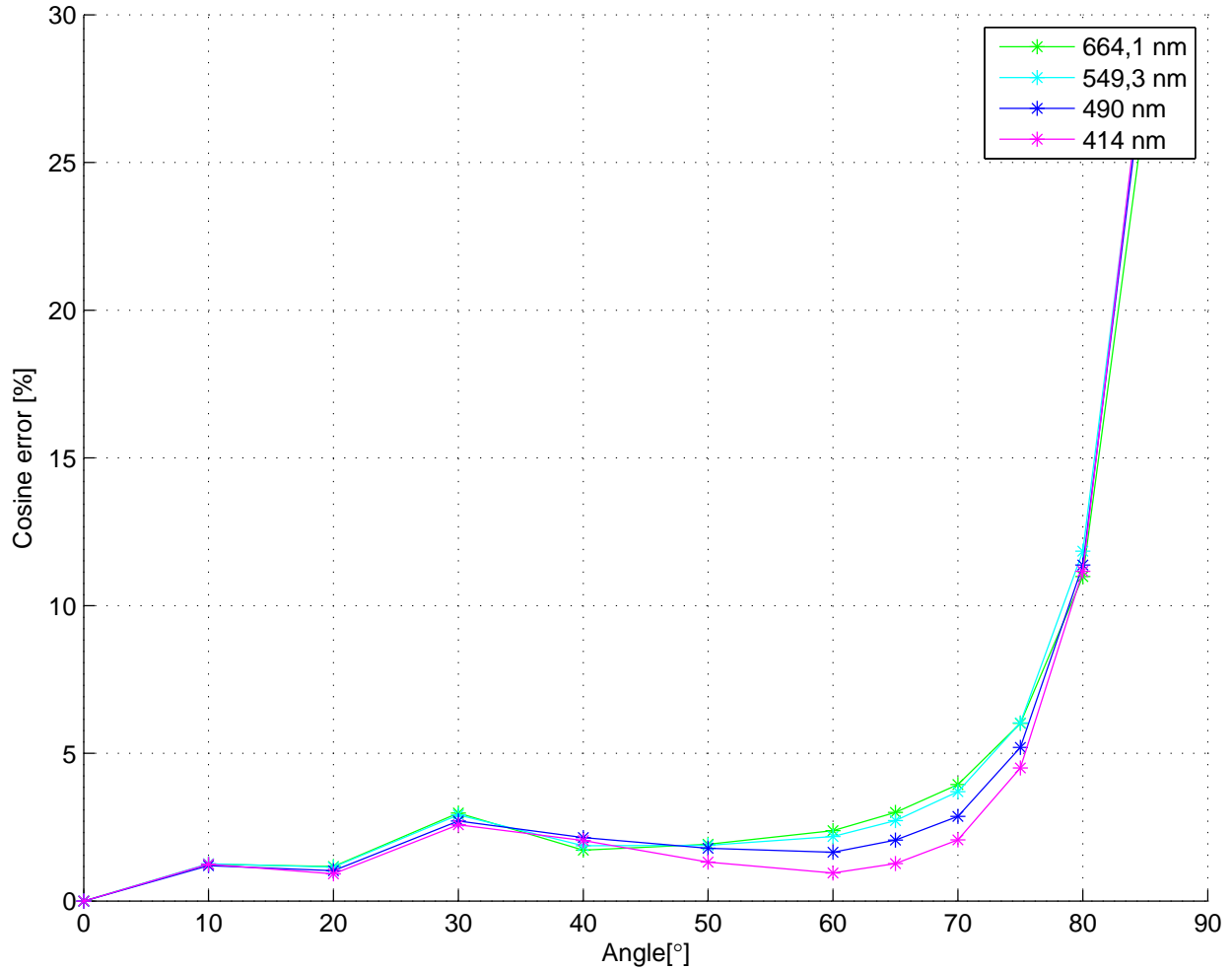


Figure 4.10: The cosine response error $\epsilon(\theta)$ as a function of the angle between the normal and the incoming light. Presenting four selected wavelengths of the light. As measured by the 80E2 irradiance sensor.

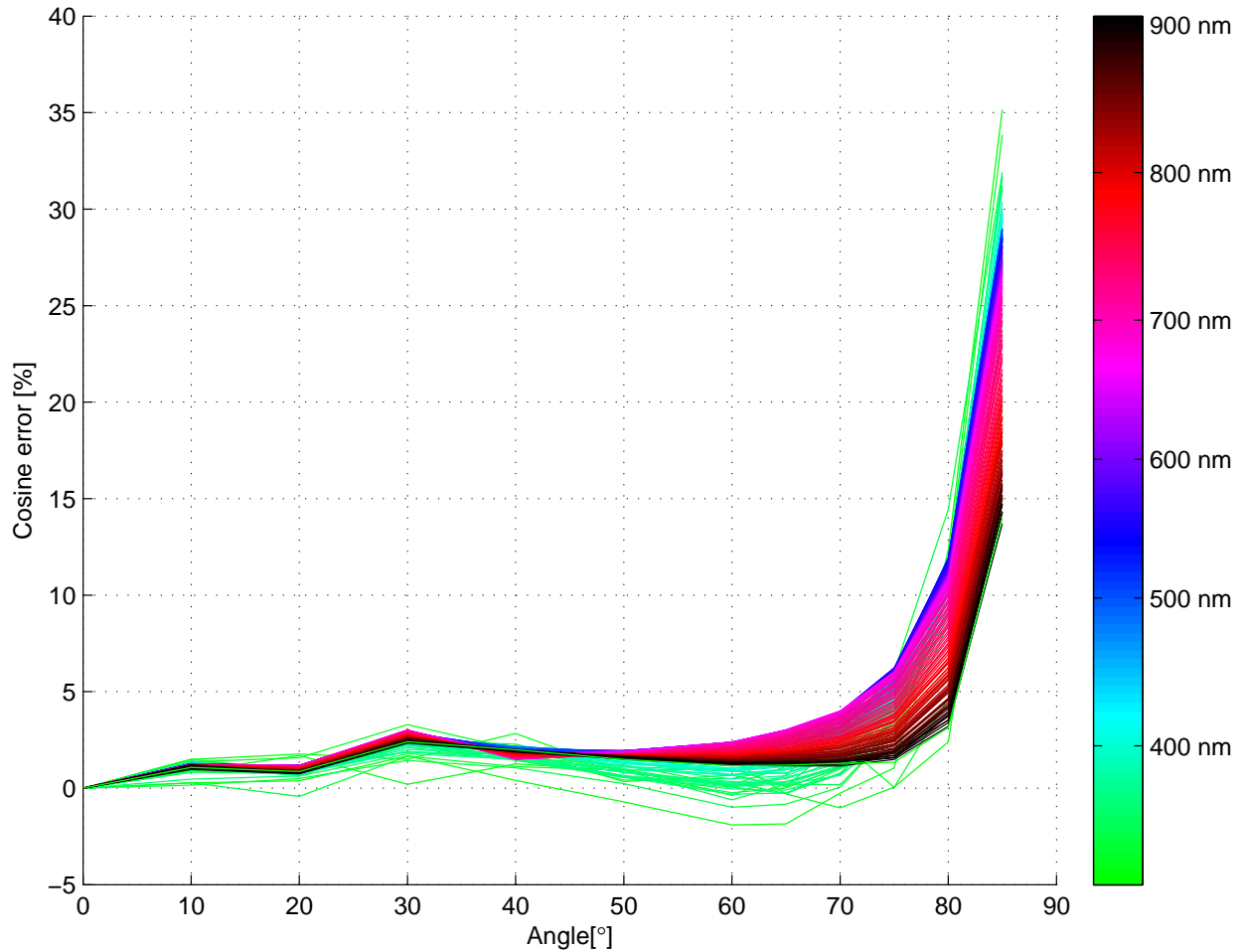


Figure 4.11: The cosine response error of the 80E2 irradiance sensor as a function of angle. Plotted for all of the wavelengths in its range. With a colorbar to identify the different wavelengths

Figure 4.11 shows all of the different wavelengths plotted for cosine response error $\epsilon(\theta)$ against the angle of the incoming light. The different wavelengths are color coded as shown in the colorbar, the lowest 320 nm in light green to the highest 950 nm as black. Below 50° there is little variation, but for higher angles the cosine response error, $\epsilon(\theta)$, is bigger for the shorter wavelengths and smaller for the longer wavelengths.

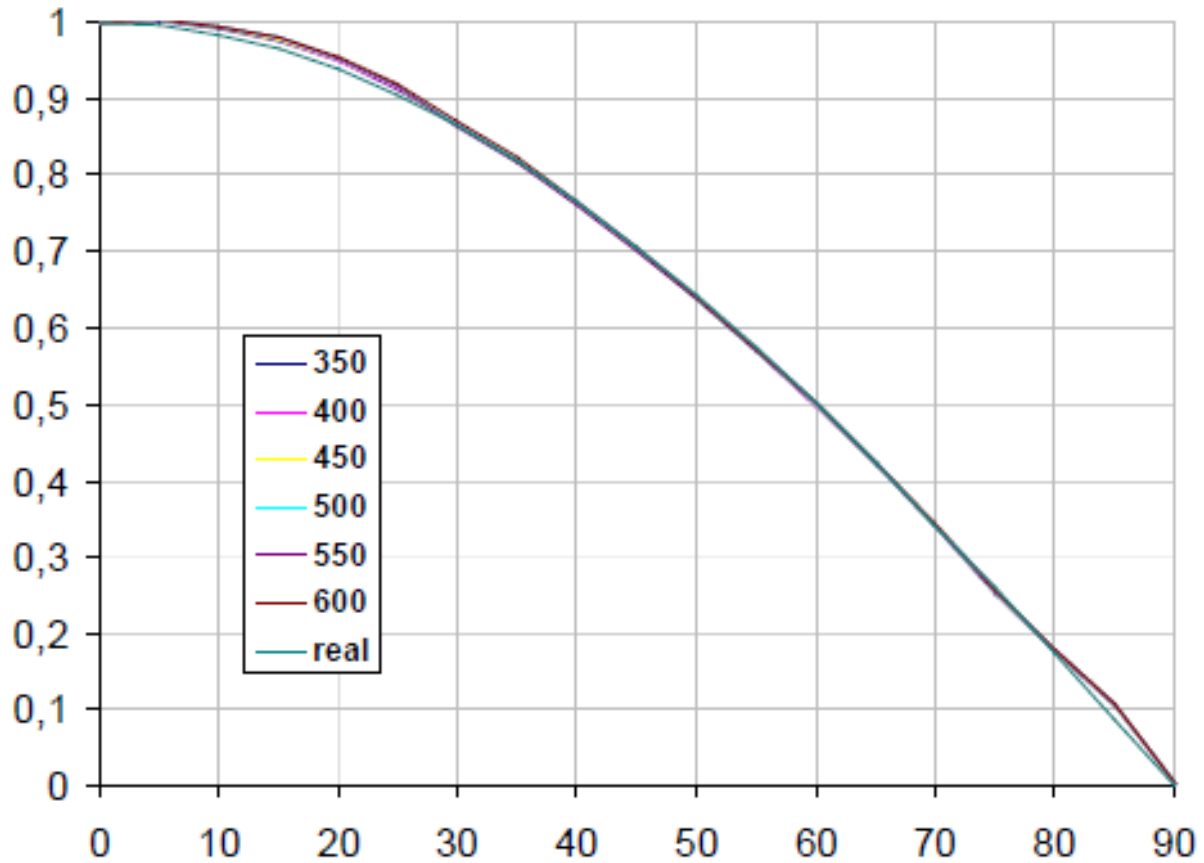


Figure 4.12: From the Trios Ramses manual TriOS (2012): A typical cosine response curve for the Ramses sensors.

Another way of presenting the cosine response of an instrument is shown in figure 4.12 and figure 4.13. In this case we are comparing the plot of a cosine curve to :

$$\frac{E(\theta)}{E_0}, \tag{4.8}$$

which according to Lambert's cosine law 2.8 should be equal to $\cos(\theta)$.

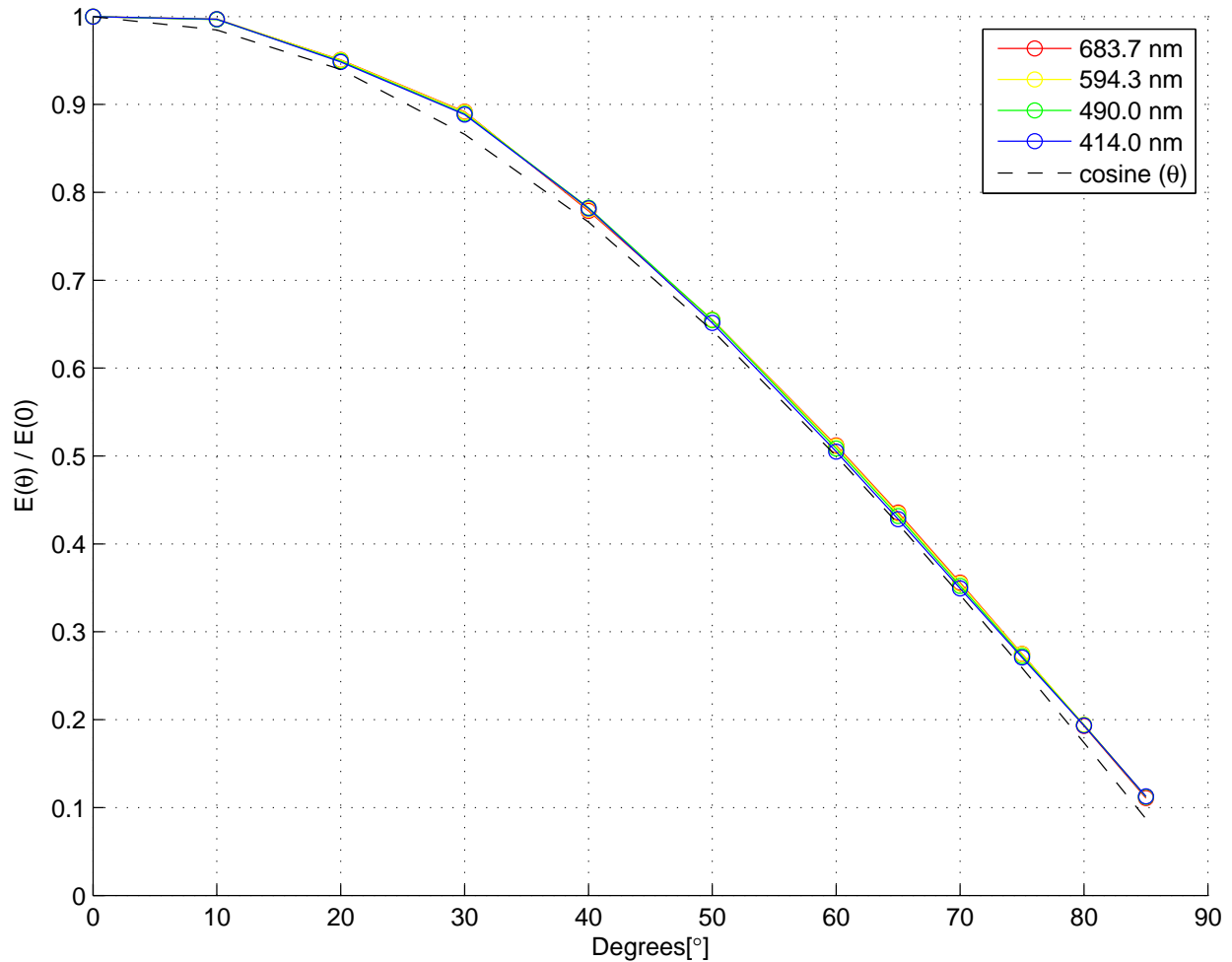


Figure 4.13: Comparison of cosine response measurements of the 80E2 sensor and an ideal cosine curve.

When comparing our measured cosine curve (figure 4.13) to the one found in the manual (figure 4.12) we can see that it has a similar shape and is very close to the ideal cosine curve from 40° to 70°, with have an over estimation at low and high angles. Examining the image from the Ramses manual (figure 4.13), it is in general showing less cosine response error than the ones we have measured for the two irradiance sensor 80FB and 80E2. One can speculate if this presentation technique was chosen because it will make the sensor appear very close to ideal, as opposed to showing the error in percent. We are of course looking at the same measurements, but it can be easy to forget that even though the error seems very small on the graph in figures 4.12 and 4.13 , there is quite a big error in percent at higher angles.

One final way of examining the cosine response of the sensors is displayed in figure 4.14. Here we are showing the absolute difference between equation 4.8 and the cosine curve. The difference in this case is that we have only subtracted the values calculated in 4.8 from the cosine curve, instead of looking at the percentage difference. For completely isotropic light, this can give us an understanding of which angles will give the biggest contribution to the error of the total measured irradiance.

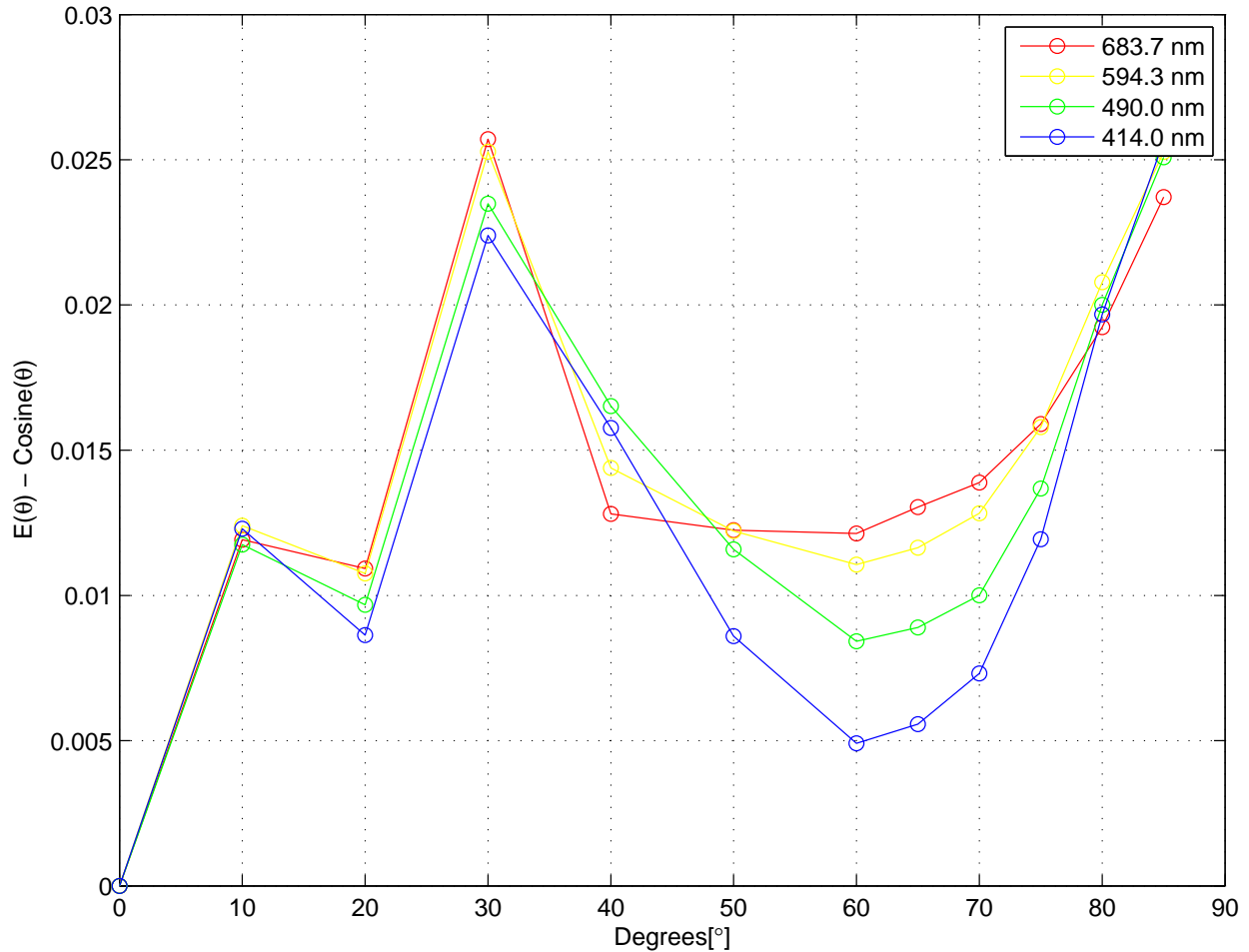


Figure 4.14: Deviation from cosine response in absolute values for 80E2 irradiance sensor at for selected wavelengths.

In the results shown in figure 4.14, we see that for isotropic light the absolute error is just as big from 30° as it is from 85°. Which is explained by the fact that a much bigger fraction of the light, 87%, incoming at 30 degrees will reach the sensor, than the from the light at

85° , 8.7%. This why the absolute irradiance error is equal for the $\epsilon(30^\circ)$ of 2.5% to the $\epsilon(85^\circ)$ of 25%. As long as the incoming light of both angles has the same energy.

This thesis focuses mainly on the problems that occur when measuring light incoming at high angles compared to the normal of the sensor. Looking at the various ways of presenting the cosine response of a sensor increases our understanding of how different aspects of a spectrometer are important for different settings. A big weakness for one type of measurements can be quite small for another. This highlights the usefulness of careful testing of sensors for various settings.

4.5 Comparing the different sensors

In this section we are examining how the different sensors compare to each other when measuring the same calibration lamp. In addition three of the sensors (80E2, 82E6 and 810C) were re-calibrated at Justervesenet (The Norwegian Metrology Service) at 04. December 2012. We have included the effect these new coefficients have had on the output of the different sensors.

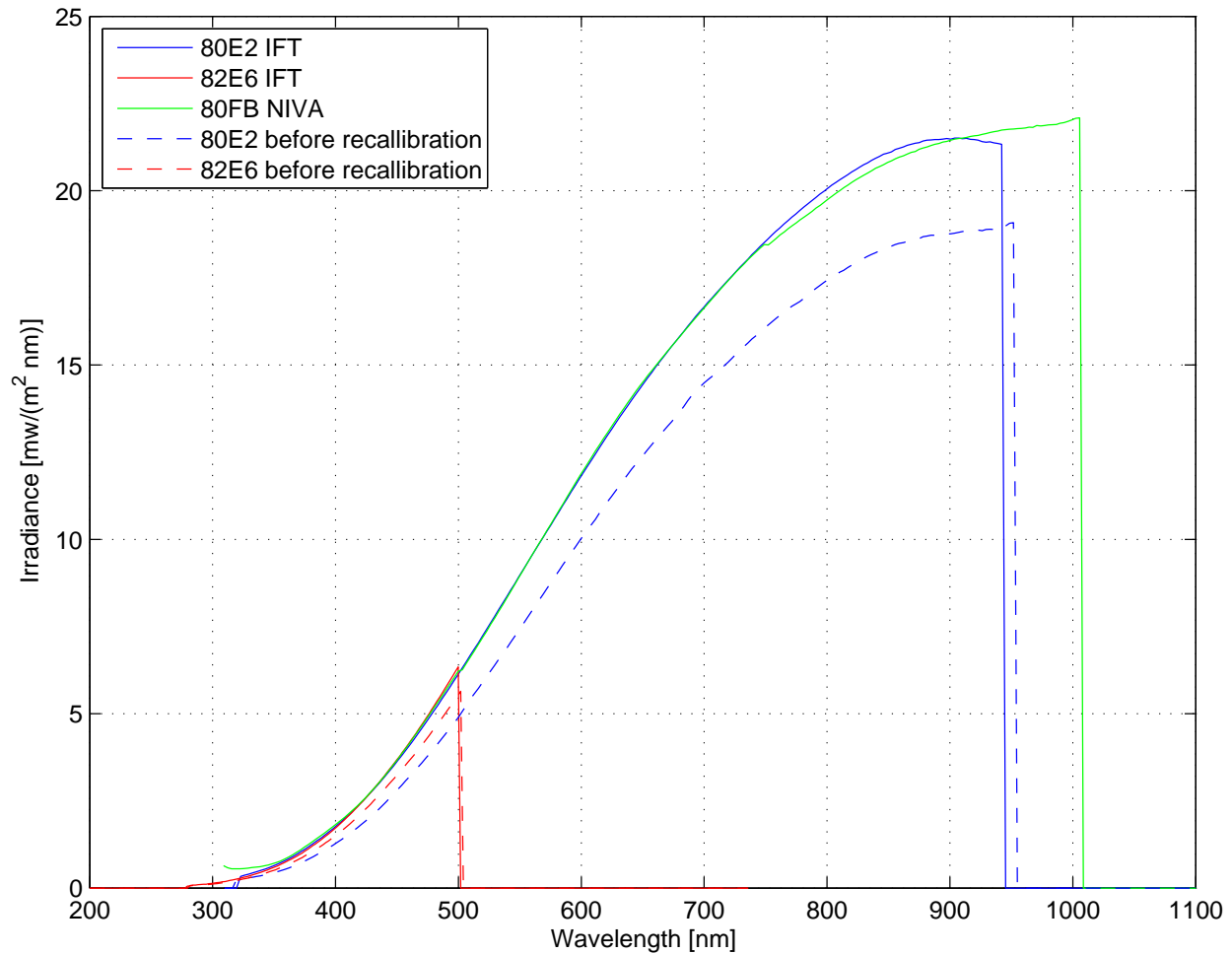


Figure 4.15: The spectrum of the calibration lamp as measured by the three different irradiance sensors. Including the spectra without recalibration coefficients

At the start of our experiments one of our irradiance sensors (80E2) measured the calibration lamp at about 20% lower value as compared with the other irradiance sensor (80FB), shown in the blue dotted line in figure 4.15. The 20% difference was the same for all wavelengths, and were found both in the laboratory and when measuring the sunlight outside. But after recalibration of one the instruments at Justervesenet!, they were measuring similar spectra as shown in figure 4.15. This clearly illustrates the need for regular recalibration of the different sensors.

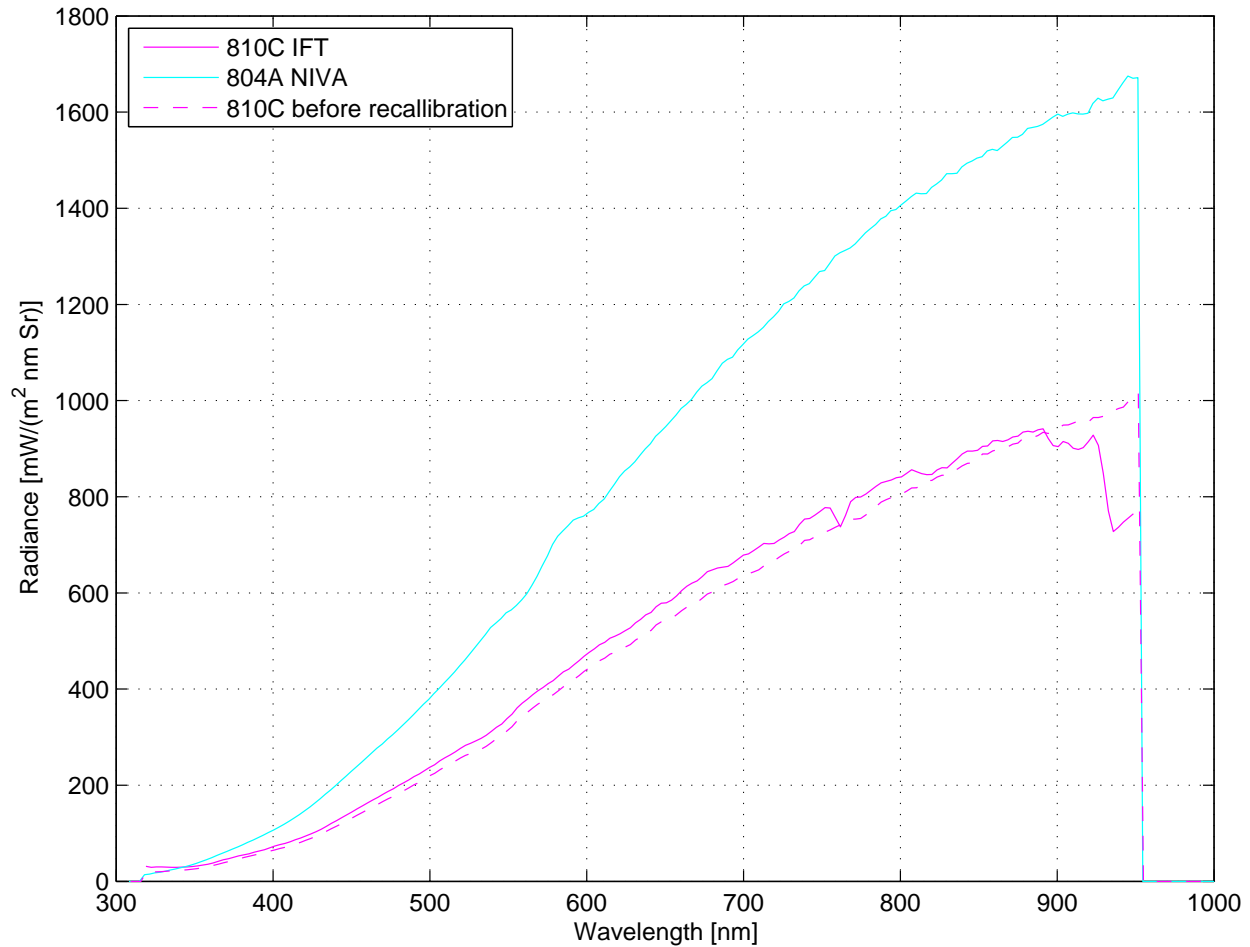


Figure 4.16: The spectrum of the calibration lamp as measured by the two radiance sensors (804A and 810C). Including new calibration coefficients for the 810C sensor.

As we can see in figure 4.16 there appears to be some error with the new coefficients for the 810C sensor (the solid magenta line), as we have shown in section 2.2 there is no reason to believe that the calibration lamp is unstable. In general the spectrum measured by the radiance sensors is not as smooth and not quite the same shape as the spectrum measured by the irradiance sensors. In addition the difference between the two radiance sensors are larger in our laboratory than the ones we found when measuring natural sunlight (see figure 5.3). All this might be an indication of a problem with the experiment. One potential problem might have been that the radiance measured is close to the saturation limit of the sensors, given as $1W/(m^2nmSr)$. Especially the 804A sensor is showing values above this limit.

To avoid the issue with over-saturation we attempted another method of calibration, where we measured the light reflected of a spectralon reflectance standard. This method has the advantage that the measured radiance will be equal for all distances and angles from the spectralon as long as the radiance sensor is only measuring light from the spectralon, and that the surface is perfectly reflecting in all directions. The decrease in the radiance of the light as we move the sensor away from the white surface is the same as the increase in the amount of light coming in due to the increased area of the spectralon that the sensor is measuring. For a perfectly Lambertian surface the scattered light will be equal in all directions, the radiance measured will then be equal to the incoming irradiance divided by pi.

By multiplying this measured radiance by pi we can convert the radiance measured to irradiance to compare radiance sensors to irradiance sensors. This comparison is plotted in figure 4.17 and figure 4.18

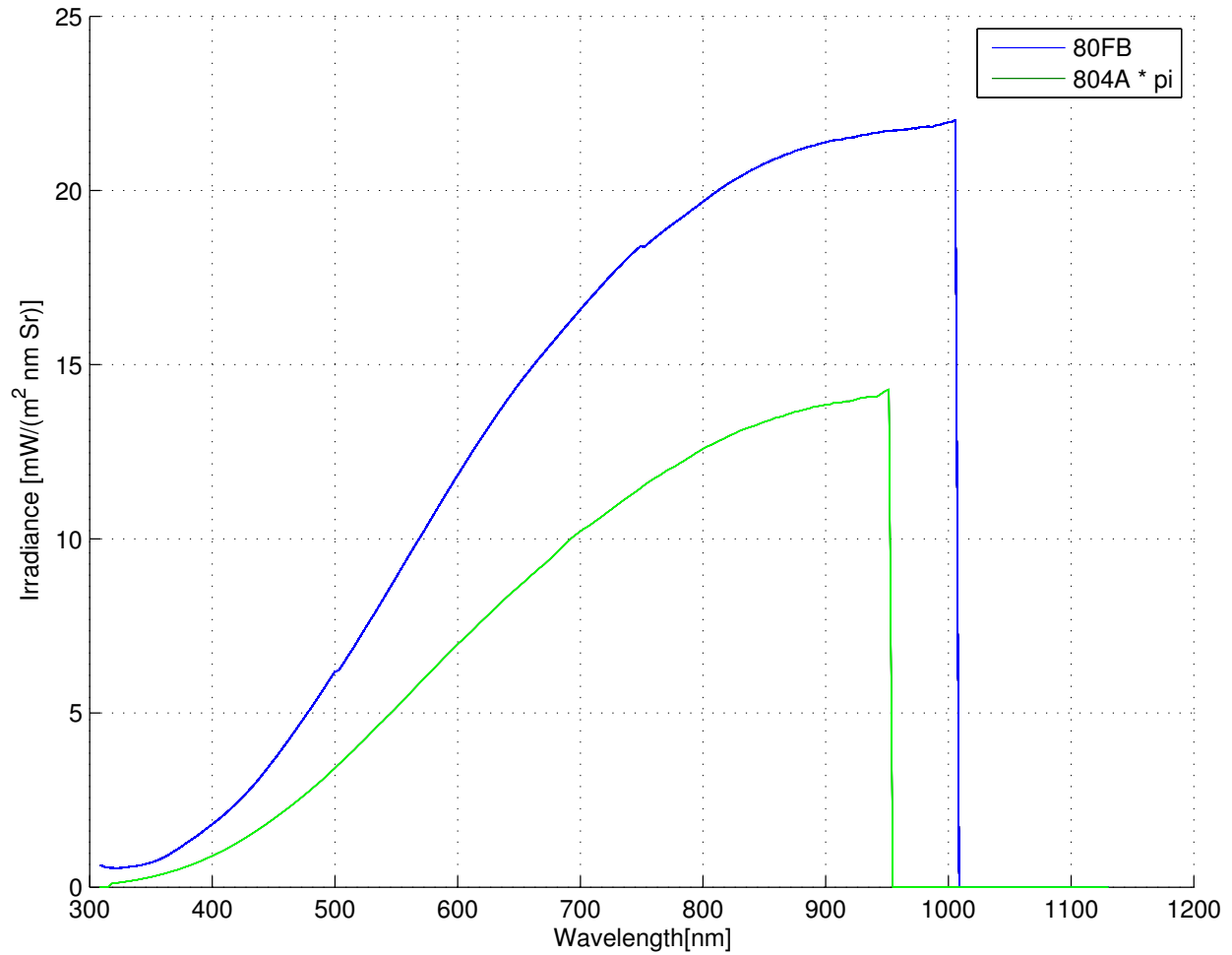


Figure 4.17: The spectrum of the calibration measured by the irradiance sensor 80FB compared to the spectrum measured by the radiance sensor 804A of white reflector (multiplied by pi).

Figure 4.17 shows a big difference between the expected outcome and our actual results. Since there is no perfectly white reflector we expect to measure a slightly lower radiance than the theoretical one, but this can not explain this big difference.

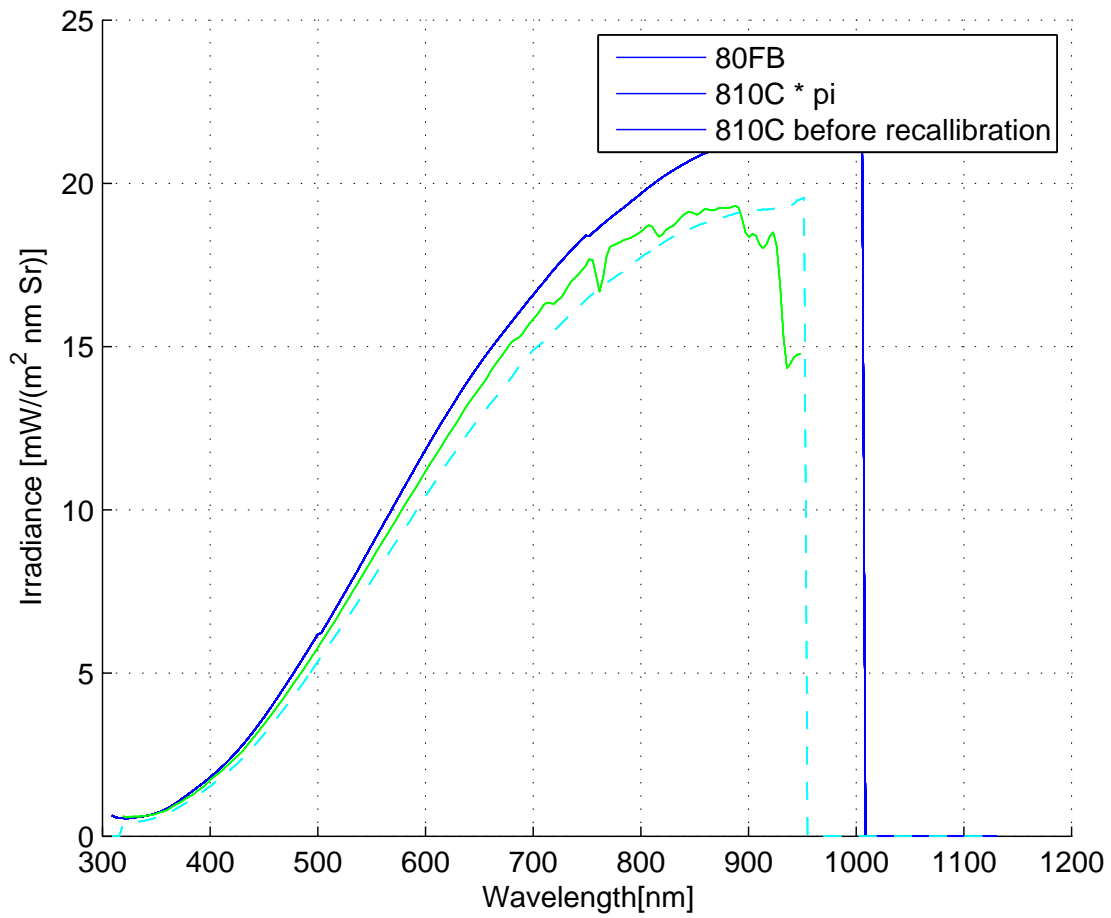


Figure 4.18: The spectrum of the calibration measured by the irradiance sensor 80FB compared to the spectrum measured by the radiance sensor 810C of white reflector (multiplied by π).

There is a big difference between the results obtained with this method as well. The 810C radiance has shown much better results. But the need for new calibration coefficients for these sensors are clear.

4.6 Examining possible problems in the setup, and determining the uncertainty of the measurements

At the start of the experiments we got some results that were hard to understand and was inconsistent. The difference between the two rotating sides was quite big, and a bit of light was recorded at 95° which should be zero for all wavelengths, if no stray light was present. There also were some inconsistencies when trying to reproduce the various results. Some effort went into looking for things that could be wrong, and two main issues (stray light and inconsistencies) were resolved. Solving the inconsistencies in the cosine response was a matter of being more meticulous in the setup of the experiments. Here we present the results obtained from the different tests we performed to check for possible errors in the setup of the experiment.

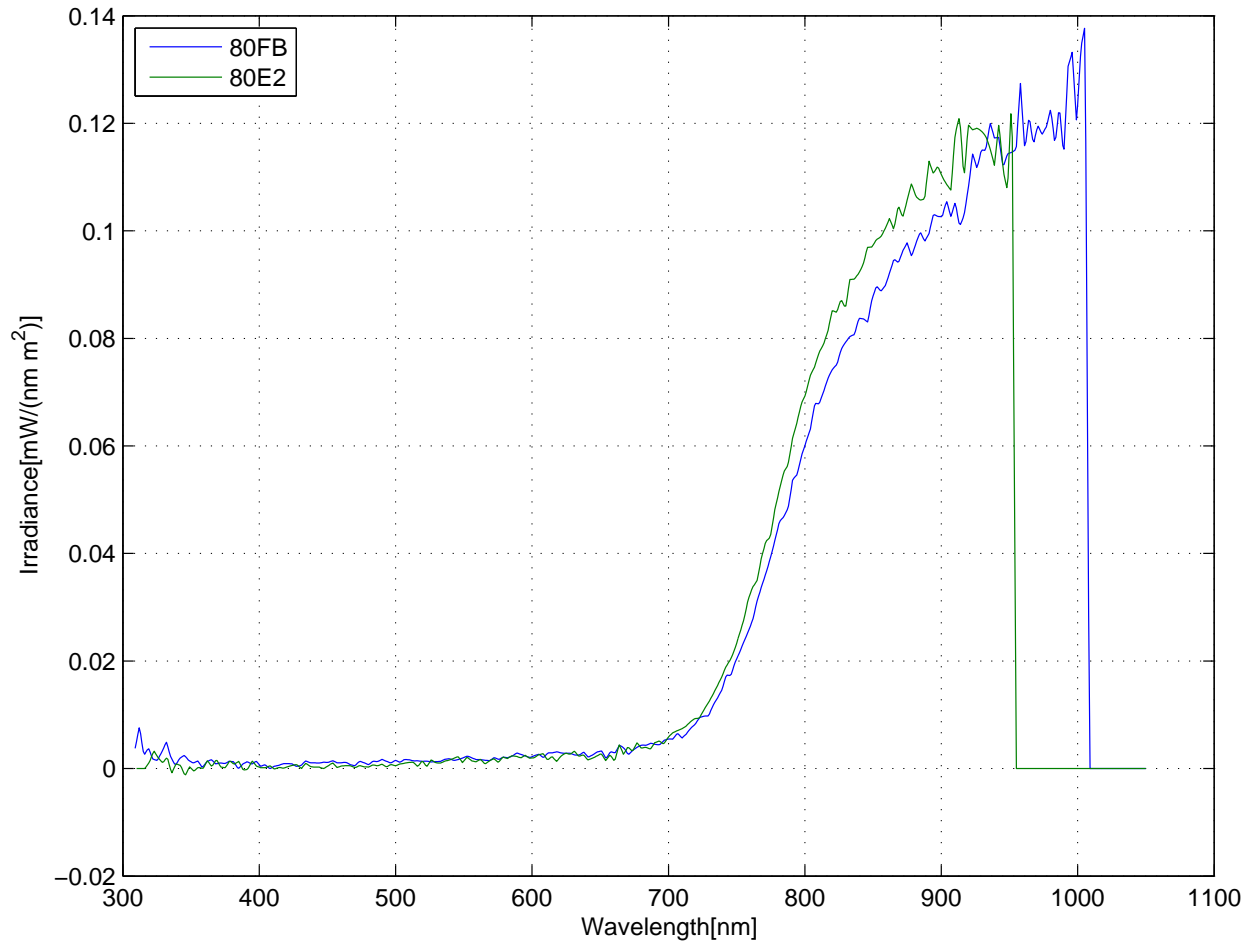


Figure 4.19: The spectra measured at $\theta = 95^\circ$ or $E_{measured}(95^\circ)$ by the 80FB and 80E2 irradiance sensors.

Figure 4.19 shows the spectrum we measured at 95° , when we were determining the cosine response error, $\epsilon(\theta)$, of the irradiance instruments. We have been able to remove all incoming stray light below 700 nm. The maximum irradiance measured in the infrared region is about 0.5 percent of the incoming light at 0° . This is a small fraction of the total irradiance but it is not insignificant compared to the spectra measured for (θ) over 80° . A plausible hypothesis for why the irradiance is different from zero in the infrared part of the spectrum, is that the dark curtains we had placed around our optical table is designed to only stop visible light. This leads to the longer wavelengths of the light being reflected inside the room.

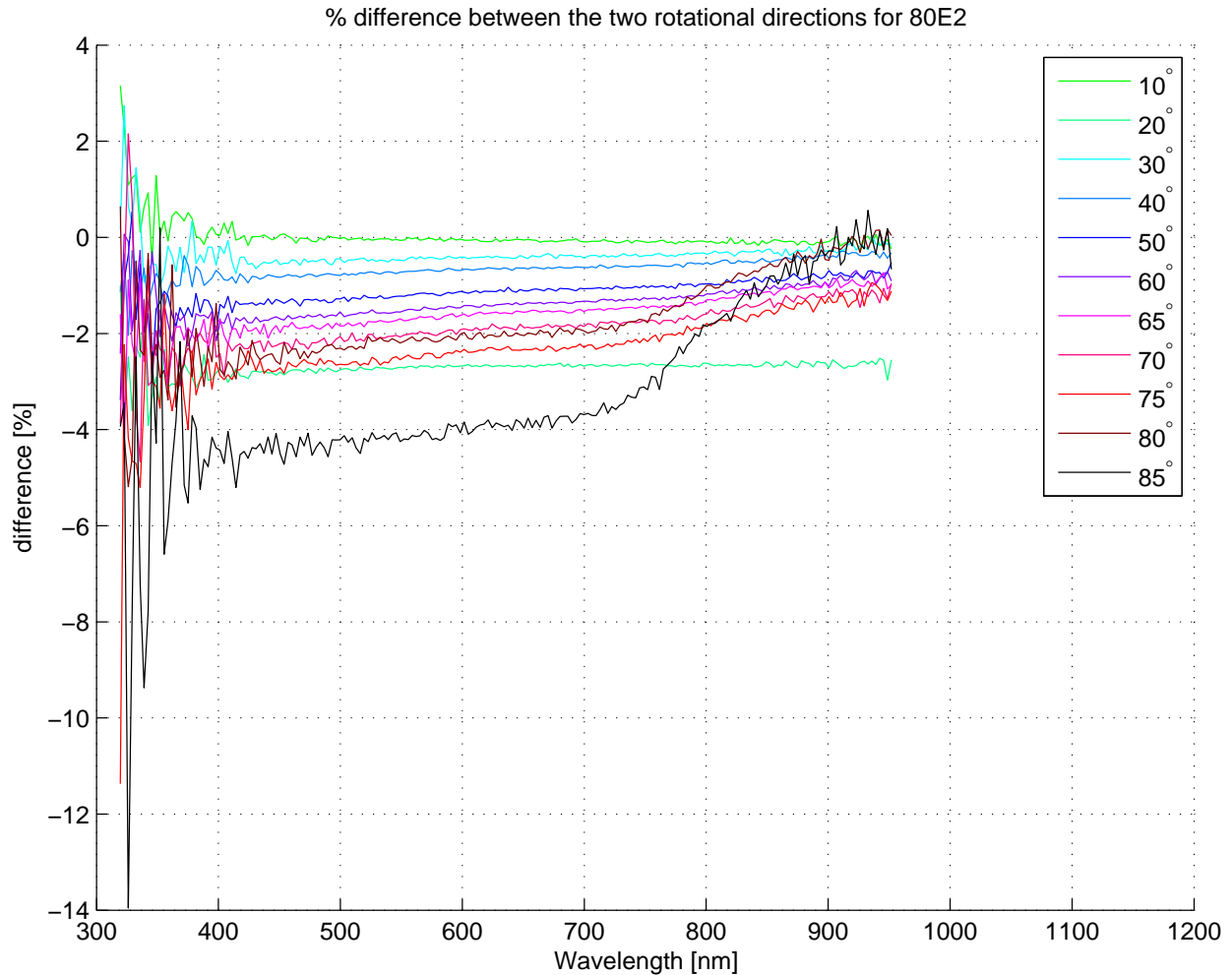


Figure 4.20: The percentage difference, for the entire spectrum, between the two rotational directions for the 80E2 irradiance sensor. Found when measuring the cosine response at the selected angles.

As a test of the quality of the setup we look at the difference between the two rotational directions of the sensor on top of the rotating table. If the sensor is exactly in the center of the rotating table then measuring the irradiance with the sensor turned 10 degrees to the left should be the same as measuring the irradiance with the sensor turned 10 degrees to the right. This is true as long as there is no azimuthal dependence in the sensor.

At the start of our measurements we found a change of more than 30 percent between the two directions for some angles. This indicated an error either in the setup, or in the

sensor itself. After several rounds in the laboratory improving the position of the sensor and laser we were able to reduce this difference quite significantly, but as shown in figure 4.20 we were not able to remove it completely. The fact that we were able to reduce the difference between the two rotating sides by paying more attention to details in the setup leads us to conclude that a likely explanation for any remaining difference is in the quality of the setup. One explanation for this high sensitivity of the experiment is found in Lambert's cosine law and the high rate of change in the cosine function for angles close to 90 degrees. An error in the setup where the sensor was misaligned by 0.2 degrees in the starting position would result in a 4 percent difference between the two sides at $\theta = 80$ degree and 8 percent at $\theta = 85$ degree. This can be seen in equation 4.9, by averaging the irradiance from both rotational directions any error induced by the determination of the angle $\theta = 0^\circ$ will be almost removed.

$$\frac{E_0 \cdot \cos(80.2^\circ) + E_0 \cdot \cos(78.8^\circ)}{2} \approx E_0 \cdot \cos(80^\circ). \quad (4.9)$$

The method of using the average value will also help reduce any random errors (see section 2.2).

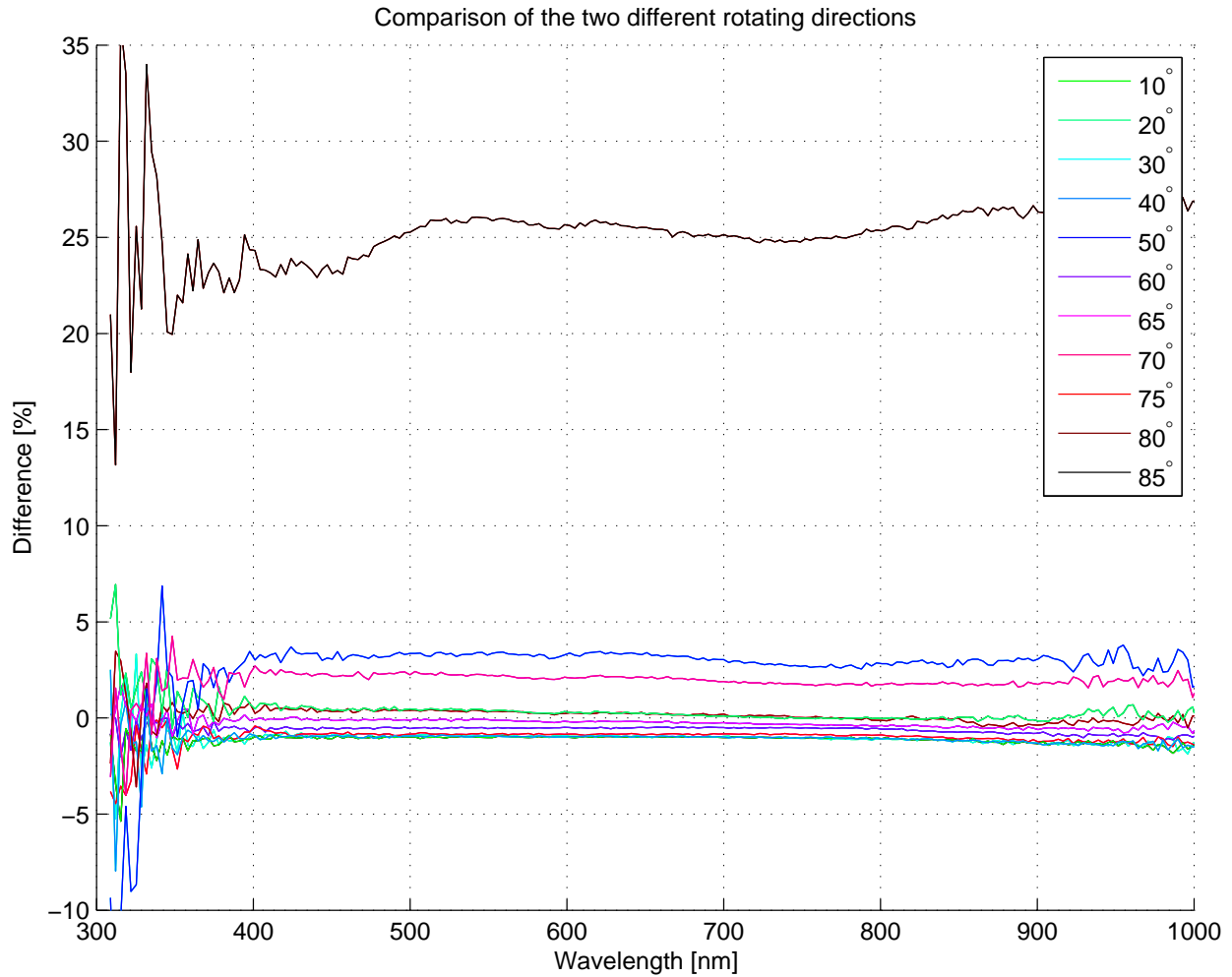


Figure 4.21: The percentage difference, for the entire spectrum, between the two rotational directions for the 80FB irradiance sensor. The difference was found when measuring the cosine response at the selected angles.

As shown in figure 4.21 we found similar differences between the two rotational directions for both instruments. With the exception for $\theta = 85^\circ$ which is much more sensitive to changes than the other angles. The similarities between the quality checks in figure 4.20 and figure 4.20 for the two instruments gives an indication of the uncertainty in θ as below 0.2 degrees.

4.6.1 Uncertainty in the measured output of the calibration lamp

We examined three uncertainty factors that could influence the measured irradiance of the calibration lamp:

- Change in the output of the calibration lamp over time.
- Change in the distance between sensor and calibration lamp.
- Change in the voltage of the power supply to the calibration lamp.

These measurements were only made with the 80FB irradiance sensor. But we expect similar results for the other sensors.

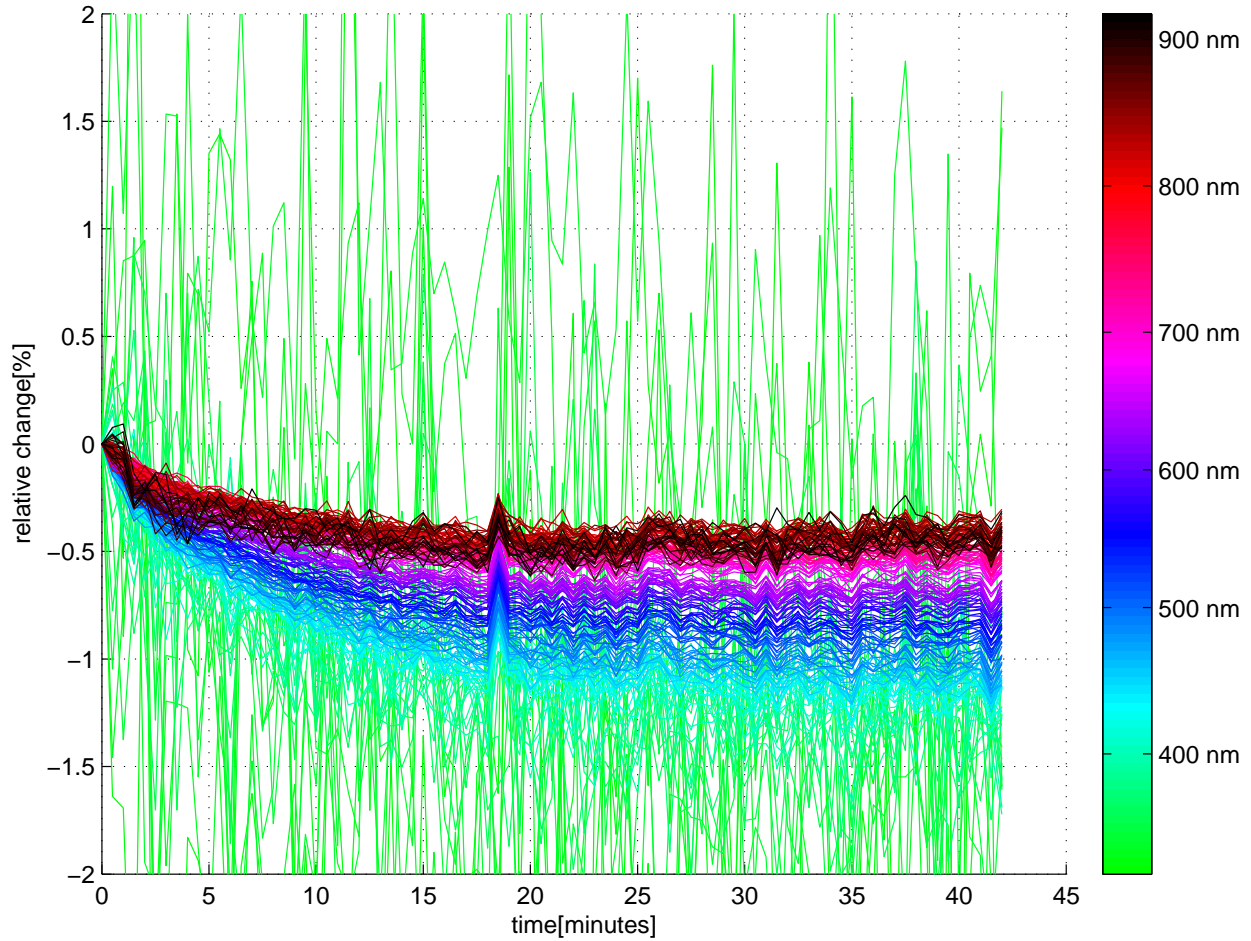


Figure 4.22: Change in measured irradiance over time for the calibration lamp. The voltage of the power supply was kept continuously at 15.000 V. Measurements were obtained by the 80FB irradiance sensor.

Figure 4.22 is a plot of the irradiance over time for the calibration lamp at $\theta = 0^\circ$. Where the time 0 is immediately after the lamp was turned on. There is a quite big variation for the different wavelengths but we see a drop in the irradiance of about 0.5 percent for the first five to ten minutes before stabilizing. This drop in irradiance is explained by the rising temperature of the lamp. In conductors increasing temperature means increasing resistance. In all of the experiments the calibration lamp was turned on at least 10 minutes before starting measurements. To determine the uncertainty in the output of the calibration lamp we calculate the standard deviation of the measurements after the 10 minute mark.

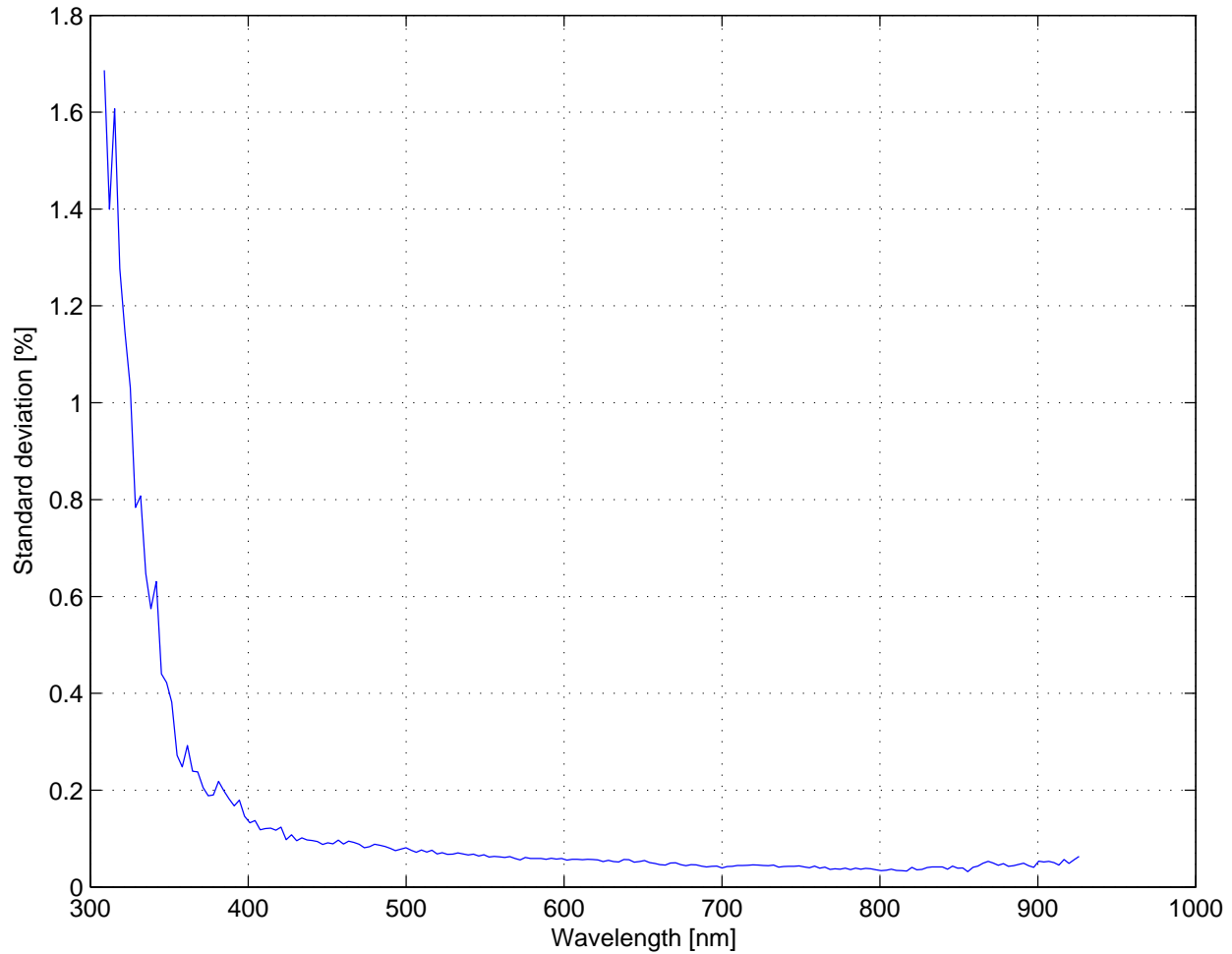


Figure 4.23: The standard deviation of the calibration lamp in percent for the entire spectrum. This result was calculated from the measured irradiance from 10 minutes after the lamp was turned on. Measurements were obtained by the 80FB irradiance sensor.

As shown in figure 4.23 there is very low variance in the measured irradiance for wavelengths longer than 400 nm indicating a stable output. We estimated the uncertainty that arises from the time factor to be equal to the standard deviation.

Note: this calibration lamp is also used to calibrate UV-sensors. We therefore make the assumption that their instability in the measured irradiance below 400 nm is not caused by the calibration lamp.

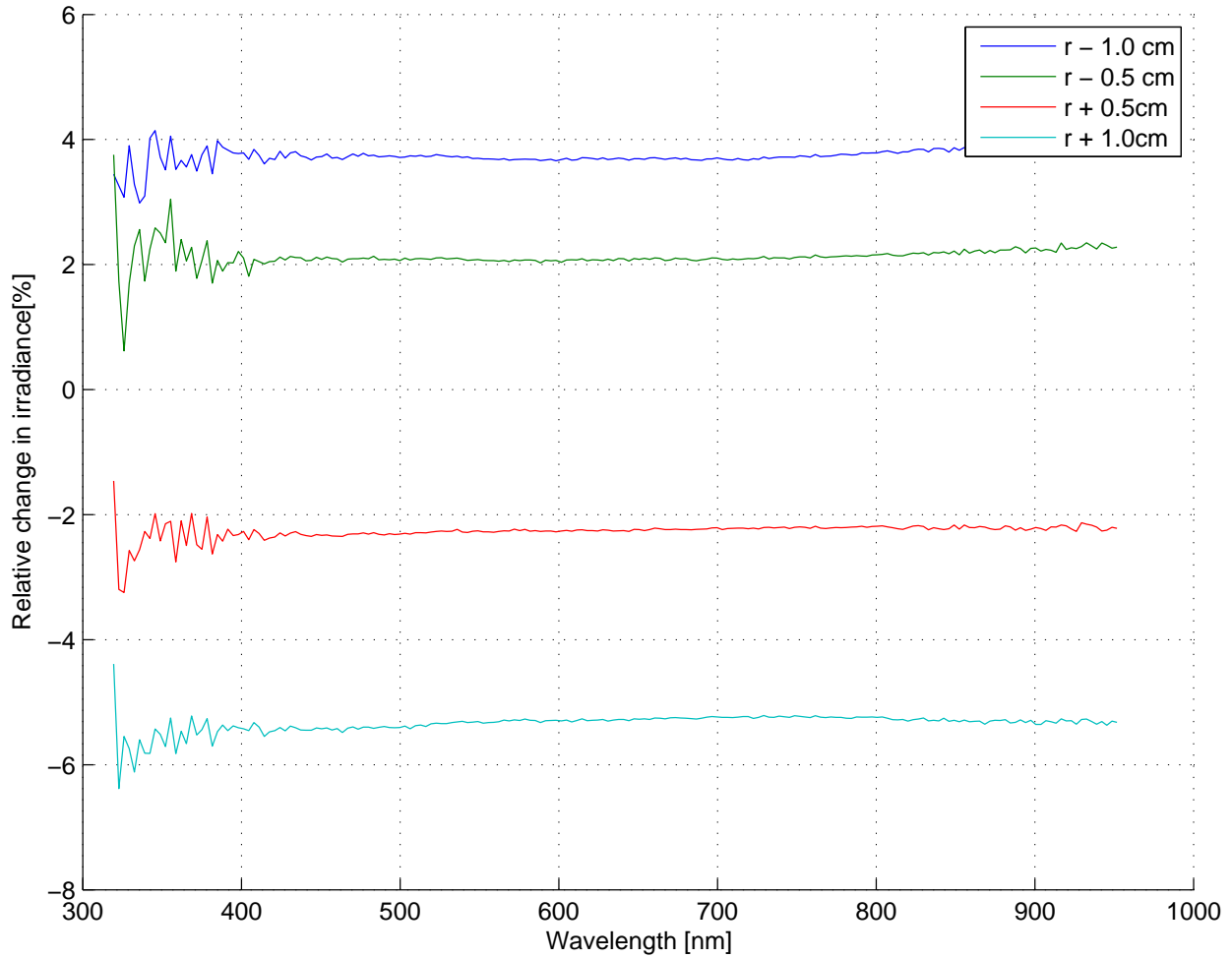


Figure 4.24: Change in measured irradiance for different distances r between the calibration lamp and the sensor compared to the default position of r equal to 50.3 cm.

Figure 4.24 is a plot showing the effect of moving the sensor towards or away from the calibration lamp. The irradiance measured follows the inverse square law 2.5. For all measurements the distance, r , from the calibration lamp to the sensor was measured to be 50.3 cm. Equation 4.10 is a sample calculation of the change in irradiance according to the inverse square law for $r - 0.5$ cm (green line):

$$\Delta E = \left(\frac{E_1}{E_0} - 1 \right) \cdot 100\% \Rightarrow \left(\frac{1/49.8\text{cm}^2}{1/50.3\text{cm}^2} - 1 \right) \cdot 100\% = 2.02\%. \quad (4.10)$$

Due to the careful alignment with lasers. Always having the rotating table and lamp kept at the same position. There was very little variation in the distance for the measurements done when measuring the cosine response. We determined the uncertainty in the distance to be about 0.05 cm. When applied to the inverse square law this leads to an estimated 0.2 percent uncertainty in the irradiance for all wavelengths.

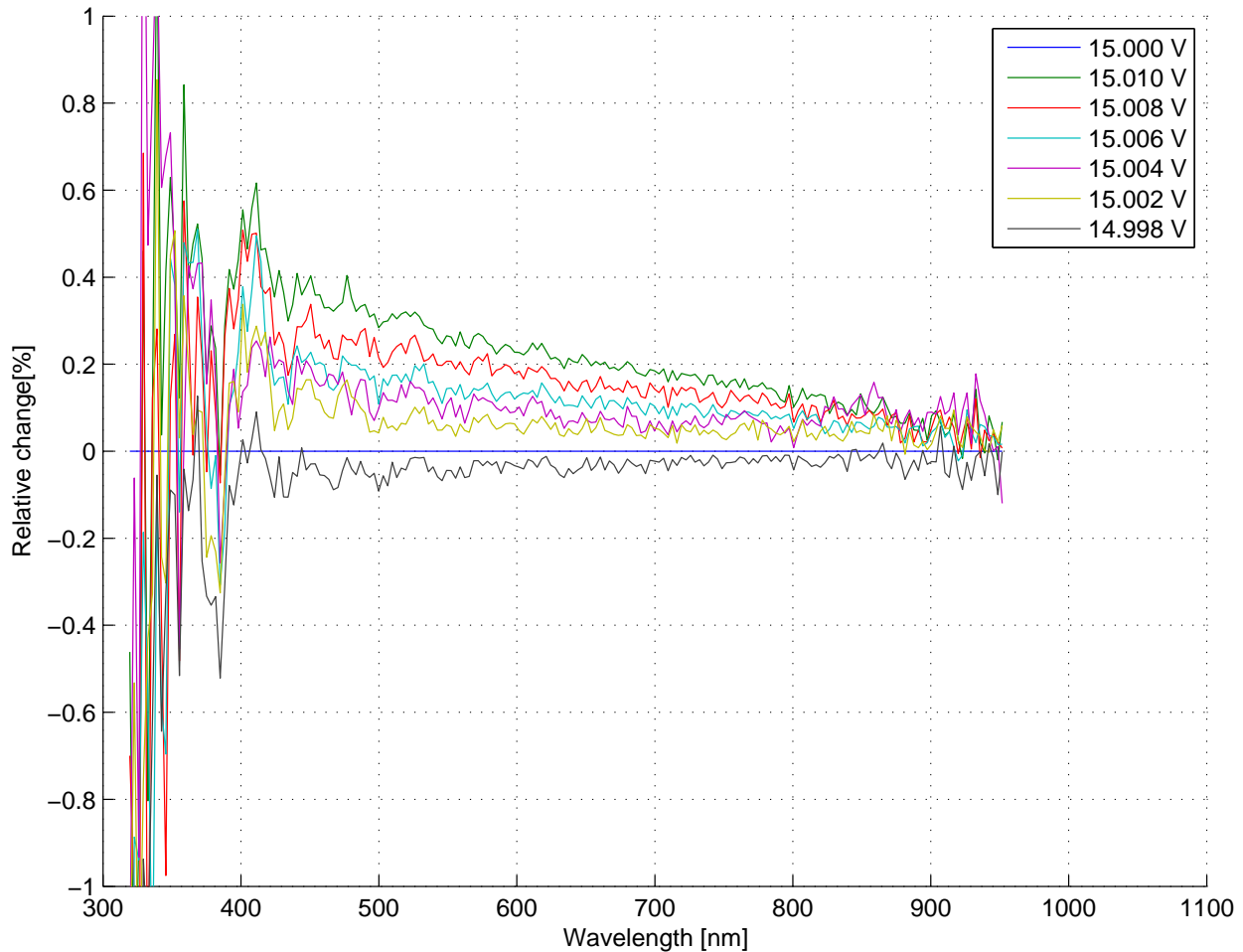


Figure 4.25: The relative change in the measured irradiance for different voltage output of the power supply.

There was some concerns about the stability of the power supply. Therefore several spectra was measured for different voltage outputs. Figure 4.25 is a plot showing how changing the voltage effects the measured irradiance. In our experiments the voltage was kept within 14.998-15.002 V for all measurements. We estimate the uncertainty from the power

supply factor to be equal to the difference between the measured spectra measured at 14.998 V(black line) and 15.002 V(yellow line). For most of the spectrum this gives below 0.1 percent uncertainty in the irradiance from this factor.

4.7 Uncertainty of the measurements

Based on the data plotted in figure 4.23, figure 4.24 and figure 4.25 we have found the uncertainties for the three uncertainty factors: time, distance and voltage. By using equation 4.11 we can estimate the combined uncertainty Δ in the measured Irradiance for the entire spectrum by using equation 2.10.

$$\Delta(\textit{combined}) = \sqrt{\Delta(\textit{time})^2 + \Delta(\textit{distance})^2 + \Delta(\textit{voltage})^2}. \quad (4.11)$$

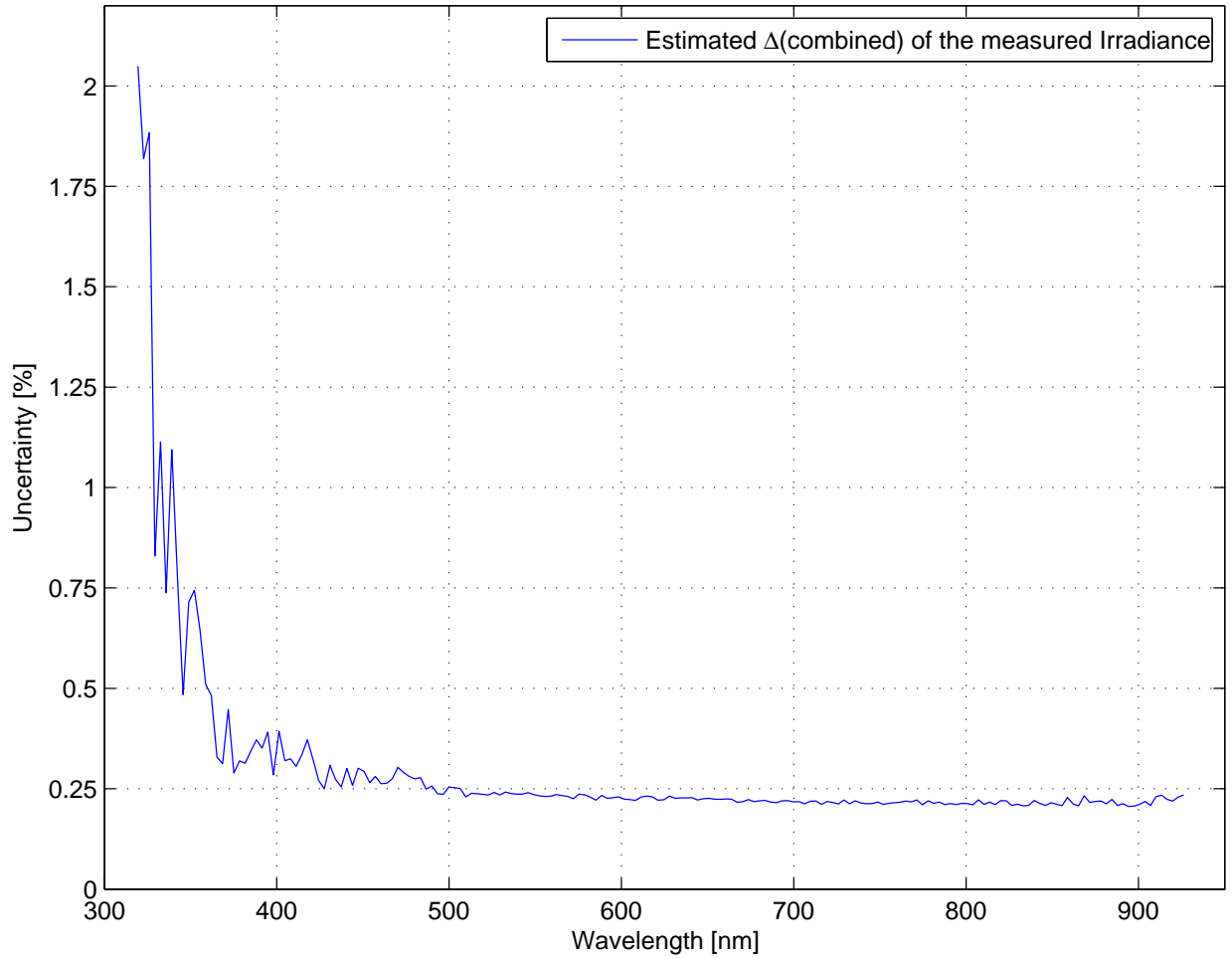


Figure 4.26: The combined uncertainty in the measured irradiance, at $\theta = 0^\circ$, calculated for the entire spectrum. Calculated from equation 4.11.

In figure 4.26 there is about 0.25 percent uncertainty for wavelengths longer than 400 nm in the measurement of the irradiance at normal incidence (E_0).

Next we calculate the uncertainty in the measured irradiance at the different angles. The measured irradiance is a function of both the incoming irradiance and the cosine of the angle (Lambert's law 2.1.5). We find the uncertainty in a function from equation 2.11:

$$\Delta^2(E) = \left(\frac{\partial E}{\partial E_0}\right)^2 \cdot \Delta^2(E_0) + \left(\frac{\partial E}{\partial (\cos\theta)}\right)^2 \cdot \Delta^2 \cos(\theta). \quad (4.12)$$

Solving for the uncertainty in percent gives:

$$\frac{\Delta E}{E} = \sqrt{\left(\frac{\Delta E_0}{E_0}\right)^2 + \left(\tan(\theta)\Delta(\theta)\right)^2}. \quad (4.13)$$

Based on the difference between the two rotational directions (figure 4.20 and 4.21) we have determined $\Delta(\theta)$ to be below 0.2° for both irradiance sensors.

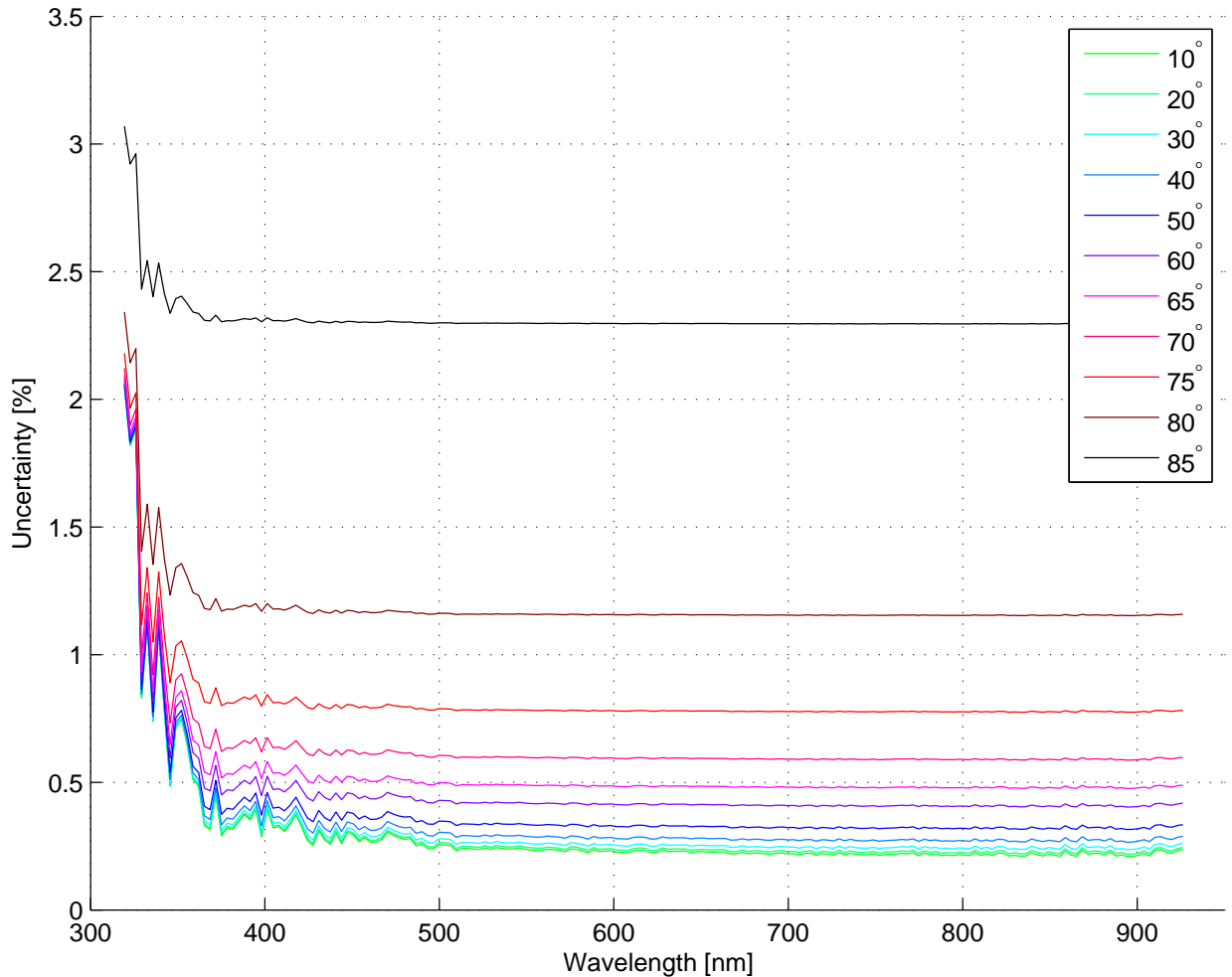


Figure 4.27: Uncertainty in the measured irradiance, for both sensors, at the various angles between the normal of the sensor and the incoming light. Calculate from equation 4.13.

In figure 4.27 we see that the uncertainty in the measured irradiance is increasing with increasing angle. The main contributor to the uncertainty is the uncertainty in the de-

termination of the angle. By looking at equation 4.5 we see that the uncertainty in the measured irradiance will be closely linked to the uncertainty in our cosine response error. As we see from figure 4.6 and figure 4.8 the uncertainty in our measurements will not have a big effect on the calculated cosine response error. Due to time constraint these uncertainties have therefore not been included in the calculations of the cosine response error.

4.8 Drift of the sensors

To see if any drift in the sensors could be observed we measured the spectrum of the calibration lamp for $\theta = 0$ with the three irradiance sensors. These measurements were made from January to March. Since we mostly measured with three sensors at the same dates we could more easily determine if any drift was due to a change in the sensors or the calibration lamp. If all three sensors started to measure less and less irradiance we are most likely looking at a change in the calibration lamp. If only one of the sensors starts measuring a different irradiance we can be almost certain that it is a change in the sensor.

Figures 4.28, 4.29 and 4.30 are plots of the differences in the measured irradiance over time for all three sensors compared to the average value of the series. The measurements show some small, but interesting variations for different wavelengths.

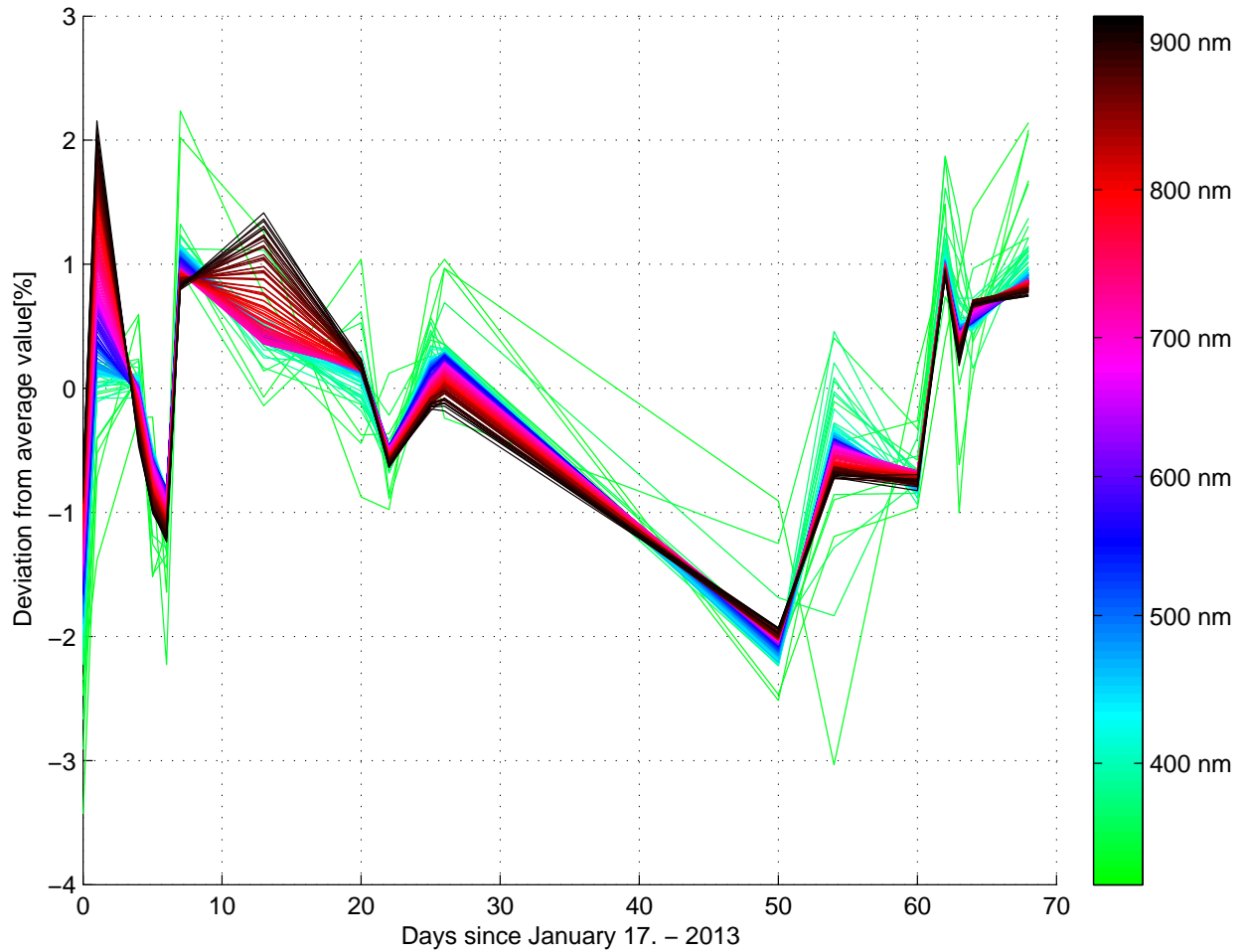


Figure 4.28: Change in the measured irradiance over time as measured by the 80E2 sensor. Every wavelength are plotted separately with a colorbar to identify them. All measurements are performed in the same position, and with the same standard calibration lamp.

The measured irradiance of the 80E2 sensor, at normal incidence of the light, in figure 4.28 shows little variation. Both for differences between the wavelengths and total irradiance. A sensor showing repeated measurements around 1% variation for over two months, should be consider to be stable.

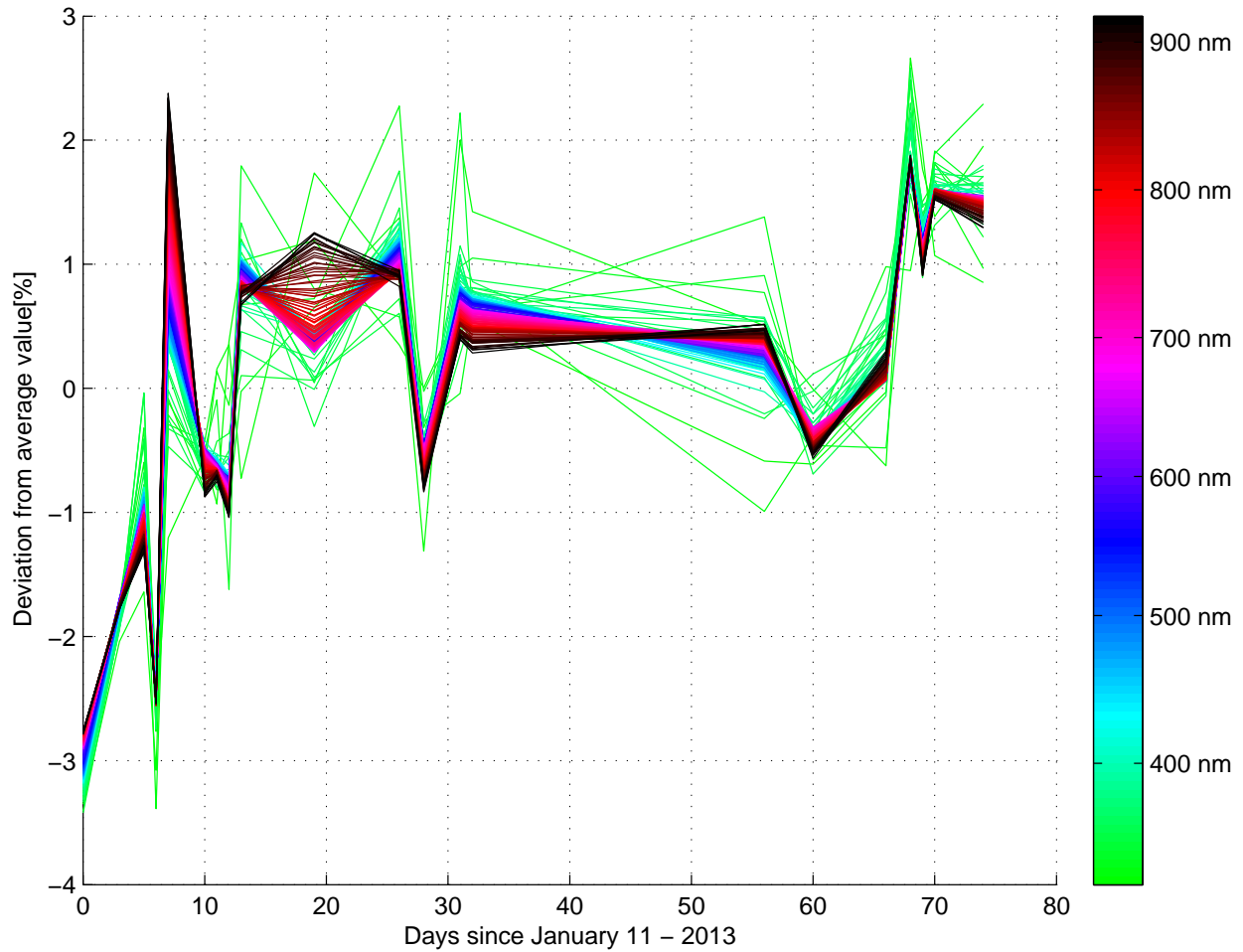


Figure 4.29: Change in the measured irradiance over time as measured by the 80FB sensor. Every wavelength are plotted separately with a colorbar to identify them. All measurements are performed in the same position, and with the same standard calibration lamp.

The change in the irradiance of the 80FB irradiance sensor, in figure 4.29 appeared to show an indication of measuring higher and higher values for the first 7 days. However the stability in the measurements from day 10 to day 70 might be an indication that the first few measurements were inaccurate.

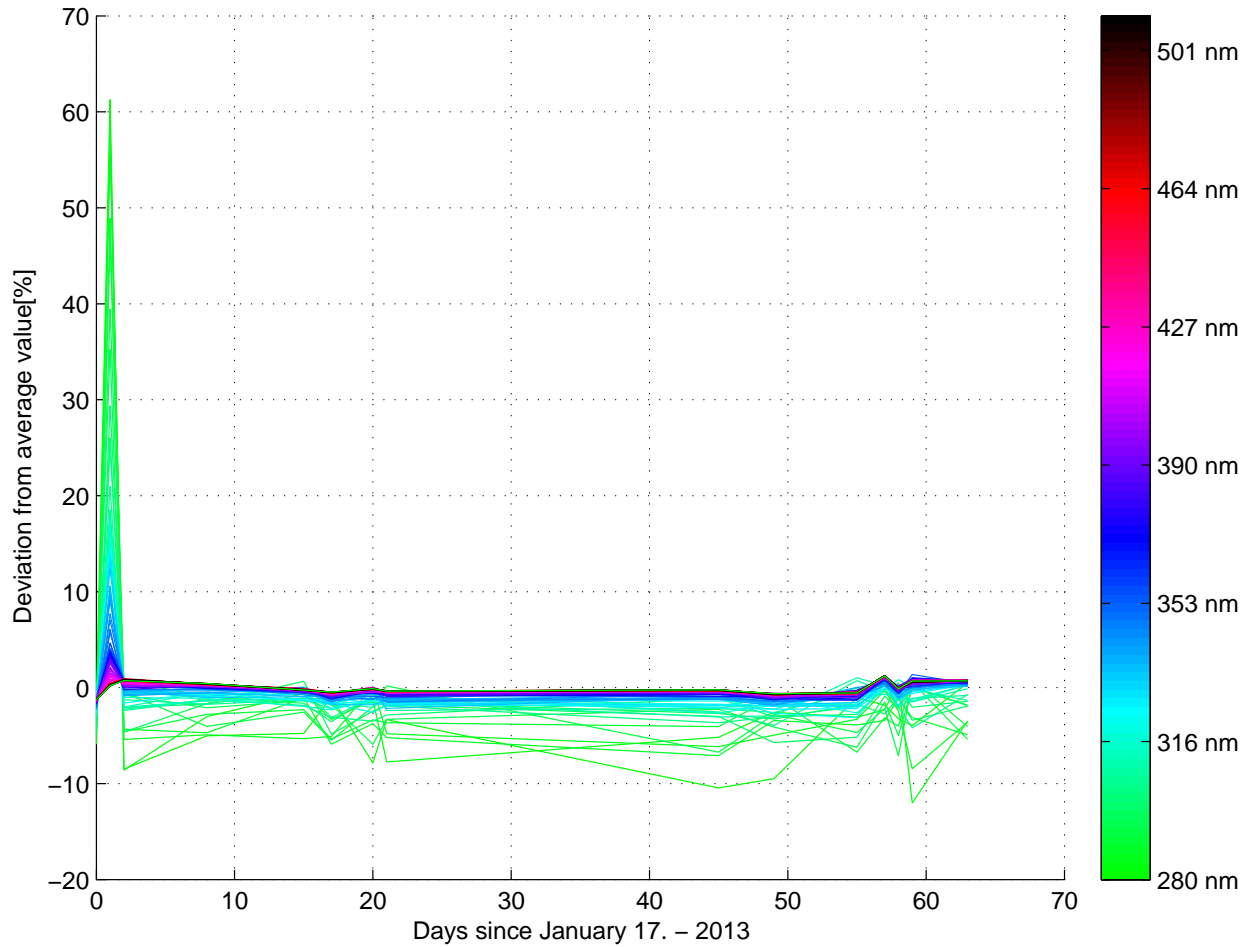


Figure 4.30: Change in the measured irradiance over time as measured by the 82E6 sensor. Every wavelength are plotted separately with a colorbar to identify them. All measurements are performed in the same position, and with the same standard calibration lamp.

In figure 4.30 we see that the UV focused 82E6 irradiance sensor is showing slightly more variation in its measurements. There is an especially big change early in the measurements. At this time we don't know what caused this big change.

For all three sensors there are few wavelengths showing more than 2 percent deviation from the average value. This must be considered an acceptable result. No clear pattern can be made to determine any drift in any of the sensors.

5 Measurements in natural sunlight

In this section we have examined how the sensors compare to each other when measuring natural sunlight. To ensure the sensors were measuring in the same direction they were fastened with screws to a metal plate and mounted on top of a tripod. A spirit level was used to ensure that the tripod was vertically adjusted.

One of the reported problems of the sensors were sudden jumps of up to 30 percent in the irradiance, which could not be explained by natural causes. Therefore we attempted to measure for long periods of time to see if any anomalies in the output could be detected. The software included an option to have the sensor automatically measure at set time intervals. For 5 out of the 6 days the software gave various error messages after some time (20 minutes to 2 hours) had passed, and the sensor stopped measuring. Various attempts to correct this problem was made but we were unable to fix it. It is unclear if this is a problem with the sensors, software or the laptop used in the experiments.

In this section we will examine four measurement sets from the following dates:

- Thursday 17. January: Two radiance sensors. Weather: clear sky.
- Thursday 07. February. Comparing two irradiance sensors. Weather: clear sky.
- Tuesday 12. February. Comparing two irradiance sensors. Weather: shifting cloud cover.
- Wednesday 20. March: Comparing UV-index measurements.

The site for all the measurements was the roof of the University of Bergen - Department of Physics and Technology. Allegaten 55.

5.1 17. January, clear sky weather conditions

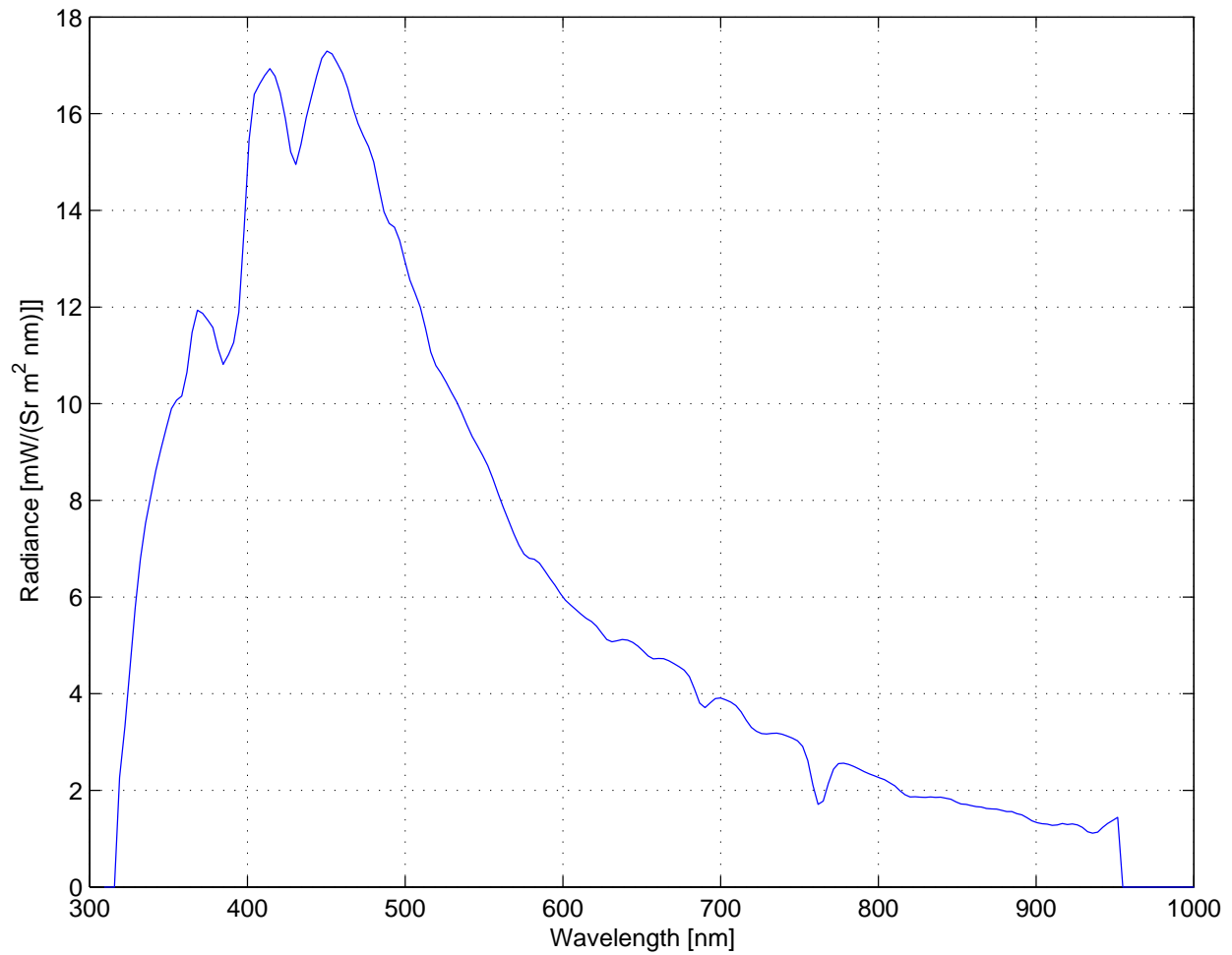


Figure 5.1: Radiance measured by the 810C radiance sensor on 17. January at 13:15. Weather conditions was clear sky.

Figure 5.1 is a sample of a natural sunlight radiance spectrum measured by the 804A radiance sensor. The sensor was vertically adjusted to measure the radiance from $\theta = 90^\circ$.

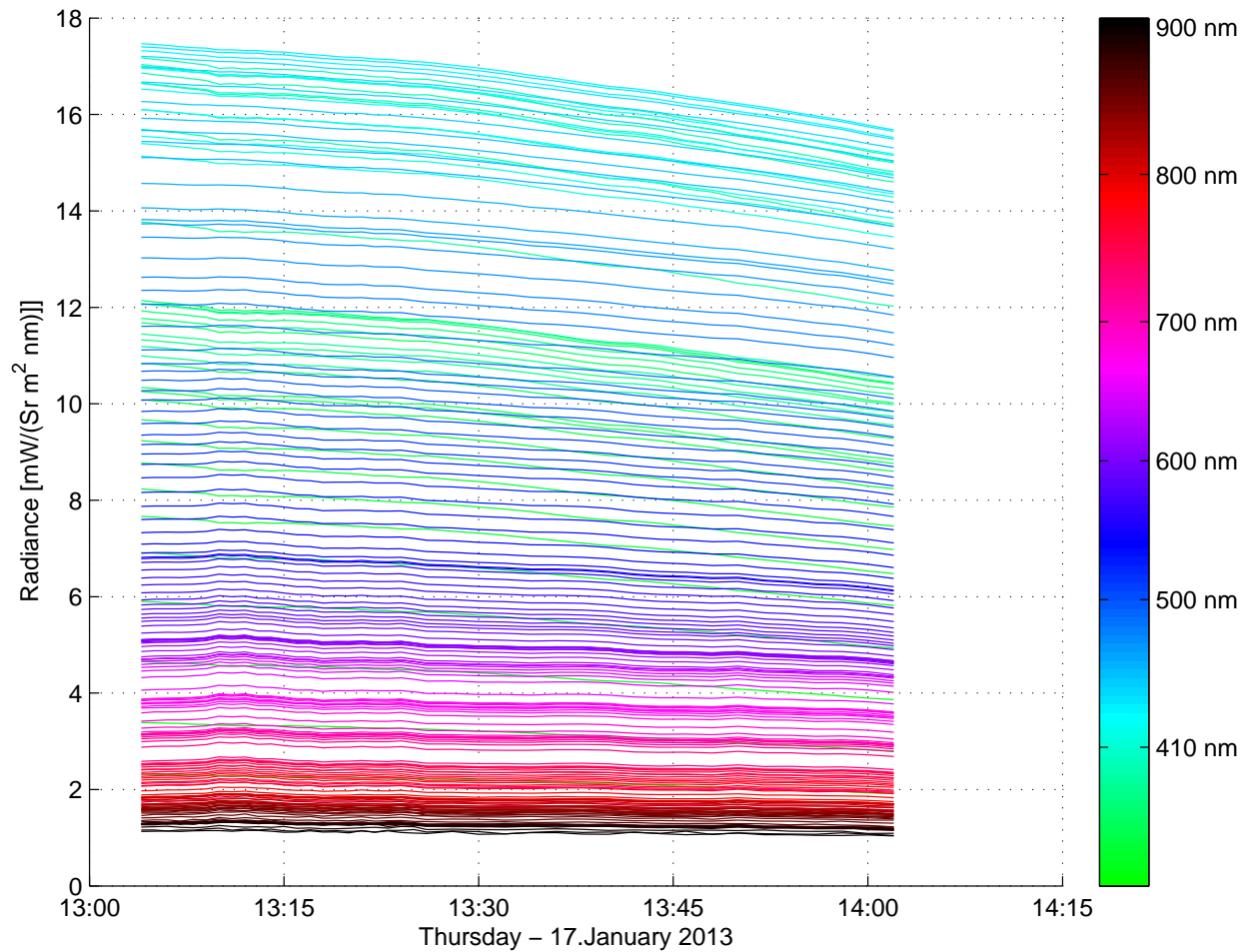


Figure 5.2: Radiance measured by the 810C radiance sensor on 17. January. Each line is the difference for a single wavelength over time, with a colorbar to identify the wavelengths. Weather conditions was clear sky.

Unfortunately we only got about one hour worth of measurements from this day. In figure 5.2 we observe a slight drop in the radiance, but it remains quite stable for the entire hour.

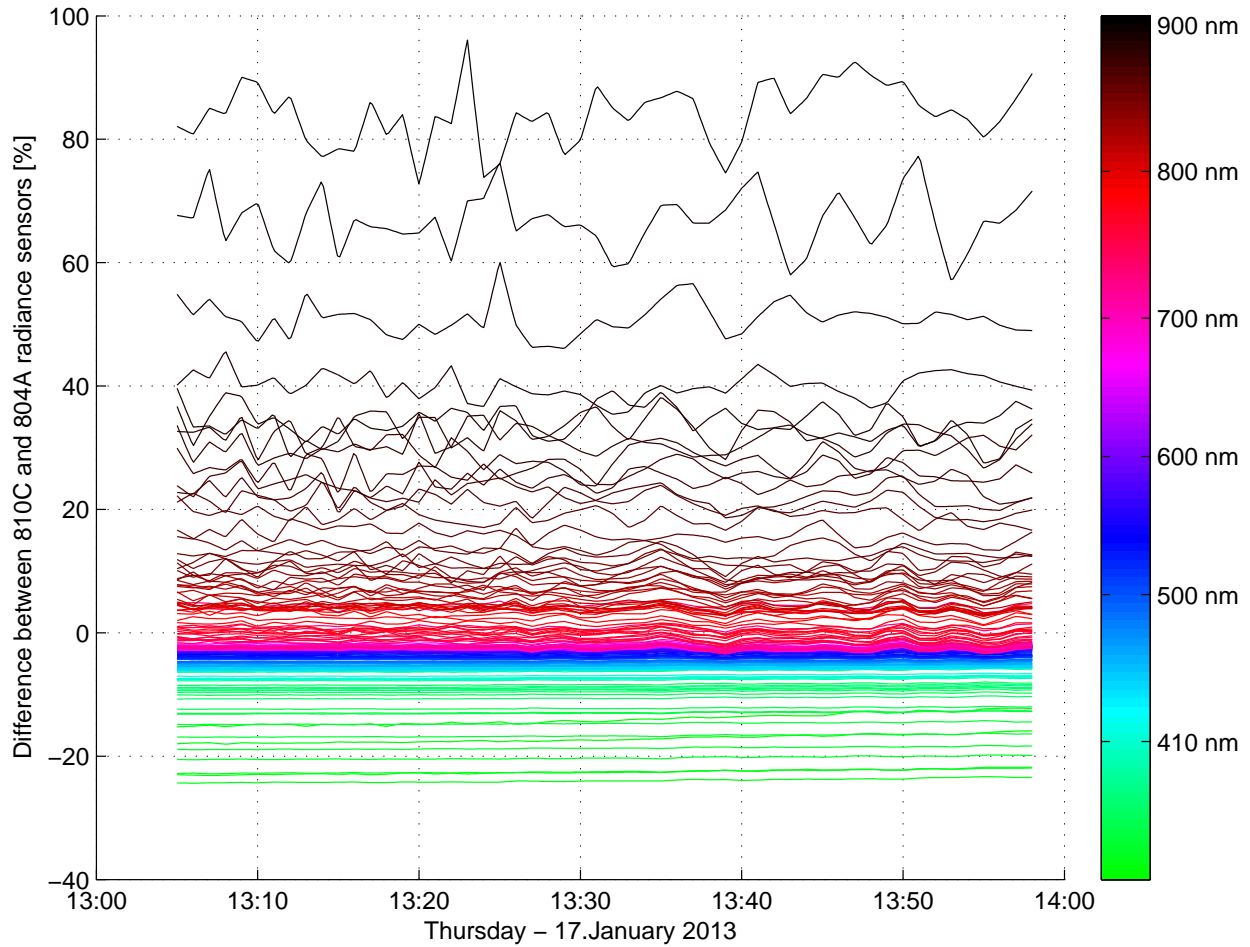


Figure 5.3: The difference, in percent, between the two radiance sensors (804A and 810C). Each line is the difference for a single wavelength over time, with a colorbar to identify the wavelengths. Both instruments were making measurements at the same time and in the same position. Weather conditions was clear sky.

Figure 5.3 shows that the big difference between the two radiance sensors is also present when measuring natural sunlight. The 804A is measuring lower radiance at shorter wavelengths and much higher at longer wavelengths. The difference for the shorter wavelengths remains quite stable, but for longer wavelengths we see some variation.

5.2 07. February, clear sky weather conditions

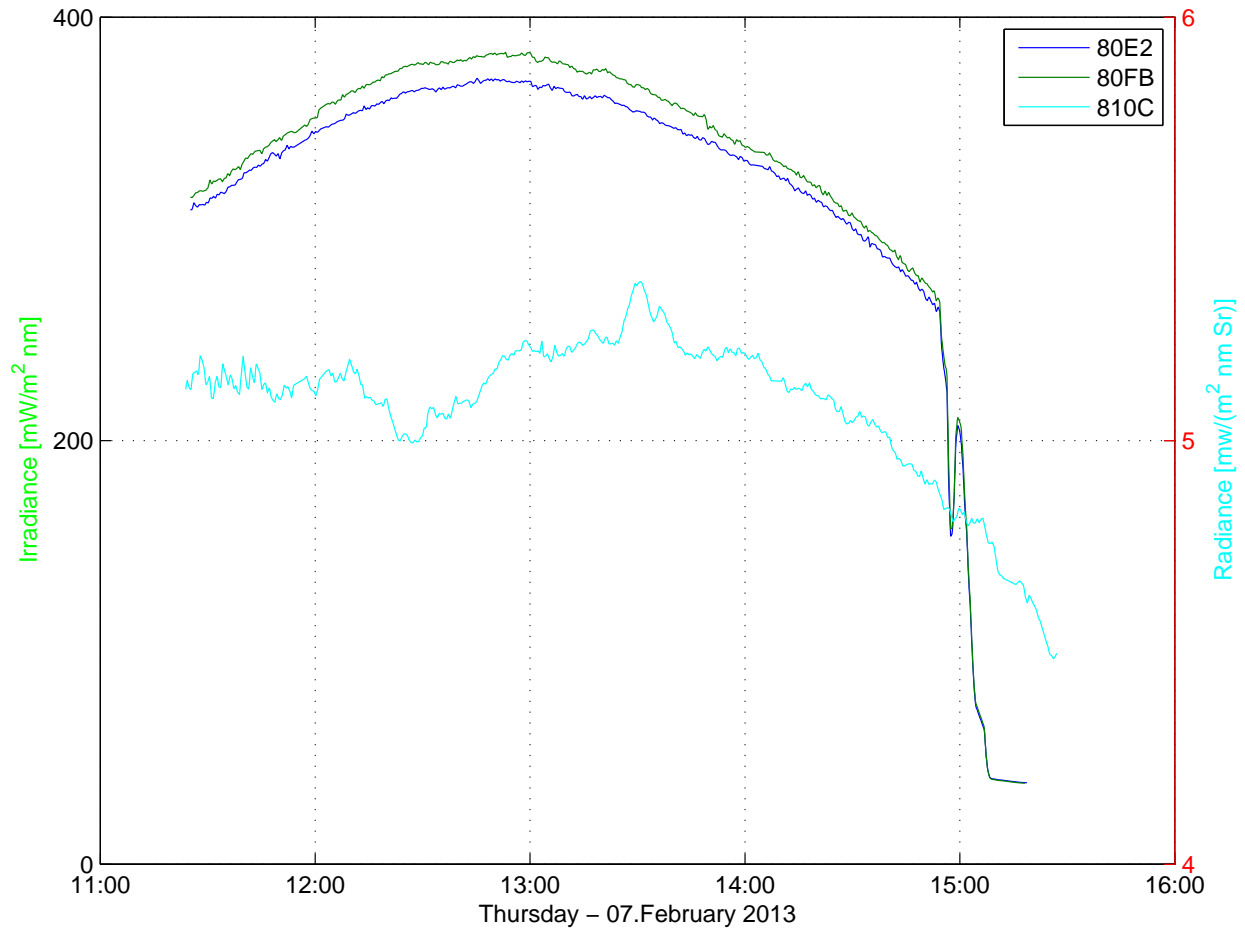


Figure 5.4: Example of a single wavelength, 664.1 nm, as measured by the two irradiance sensors (80FB, 80E2) and the radiance sensor (810C). Weather conditions was clear sky. Note: different y-axis used for the radiance.

In figure 5.4 the irradiance value follows the trajectory of the sun varying with the solar zenith angle (SZA). The radiance at this wavelength (664.1 m) is relatively stable compared to the irradiance. This can be explained by the fact that the radiance coming from straight above will be scattered diffuse light, and therefore not as dependent on the solar zenith angle.

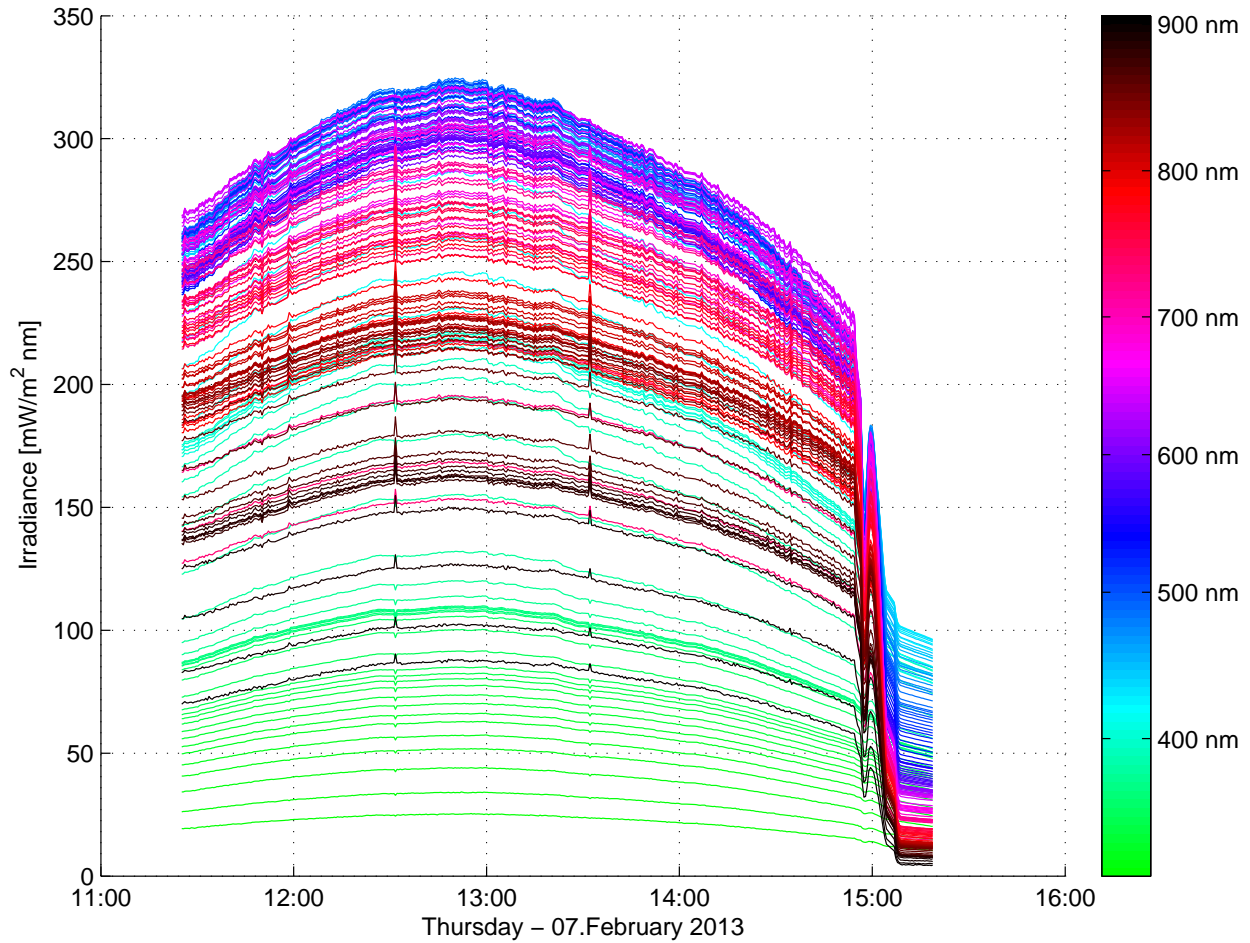


Figure 5.5: 07. February. Plot of the solar spectrum as it was measured throughout the day by the 80E2 irradiance sensor. Weather conditions was clear sky.

Figure 5.5 shows the irradiance measured on 07. February 2013. There are two anomalies around 12:30 and 13:30, where some wavelengths are showing higher irradiance and some are showing lower. We have so far not been able to explain this behavior by the sensor. The dips that are close to sunset around 14:50 might be caused by something shadowing the sensors at the time.

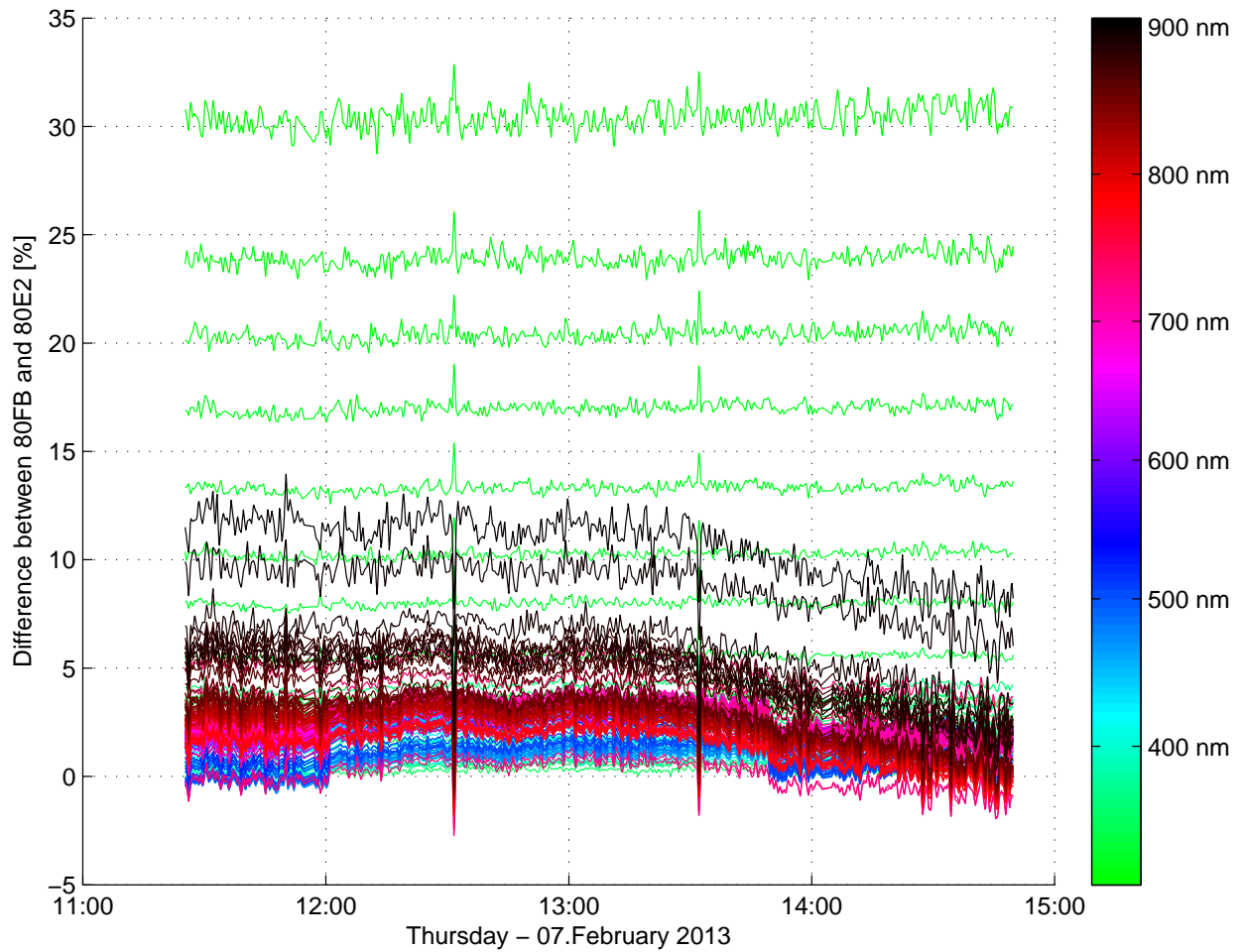


Figure 5.6: The difference, in percent, between the two irradiance sensors (80FB and 80E2). Each line is the difference for a single wavelength over time, with a colorbar to identify the wavelengths. Both instruments were making measurements at the same time and in the same position. Weather conditions was clear sky.

As shown in figure 5.6 the difference between the measurements made by the two irradiance sensors (80FB and 80E2) remain relatively stable for most wavelengths. And increases for wavelengths lower than 400 nm and higher than 850 nm. This increased difference at both ends of the spectrum might be related to the lower irradiance at both ends (see figure 5.5)

5.3 12. February, shifting weather conditions

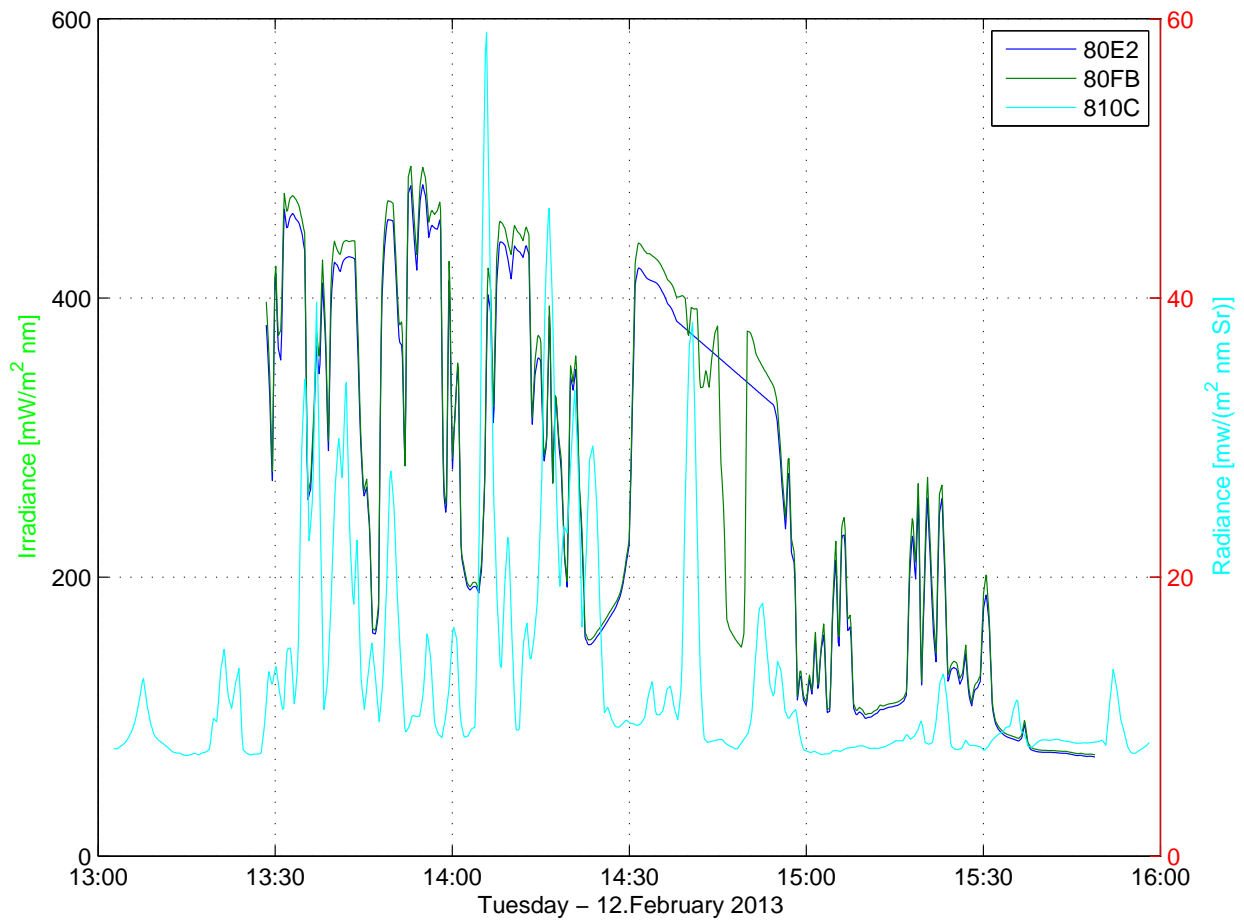


Figure 5.7: Example of a single wavelength, 664.1 nm, as measured by the two irradiance sensors (80FB, 80E2) and the radiance sensor (810C). Weather conditions were shifting cloud cover. Note: different y-axis used for the radiance.

On February 12th we used two irradiance sensors and one radiance sensor to observe the change induced by variations in the cloud cover. As can be seen in figure 5.7 (for a sample wavelength of 664.1 nm) there was big variations, both in the radiance and in the irradiance reaching the ground, throughout the day.

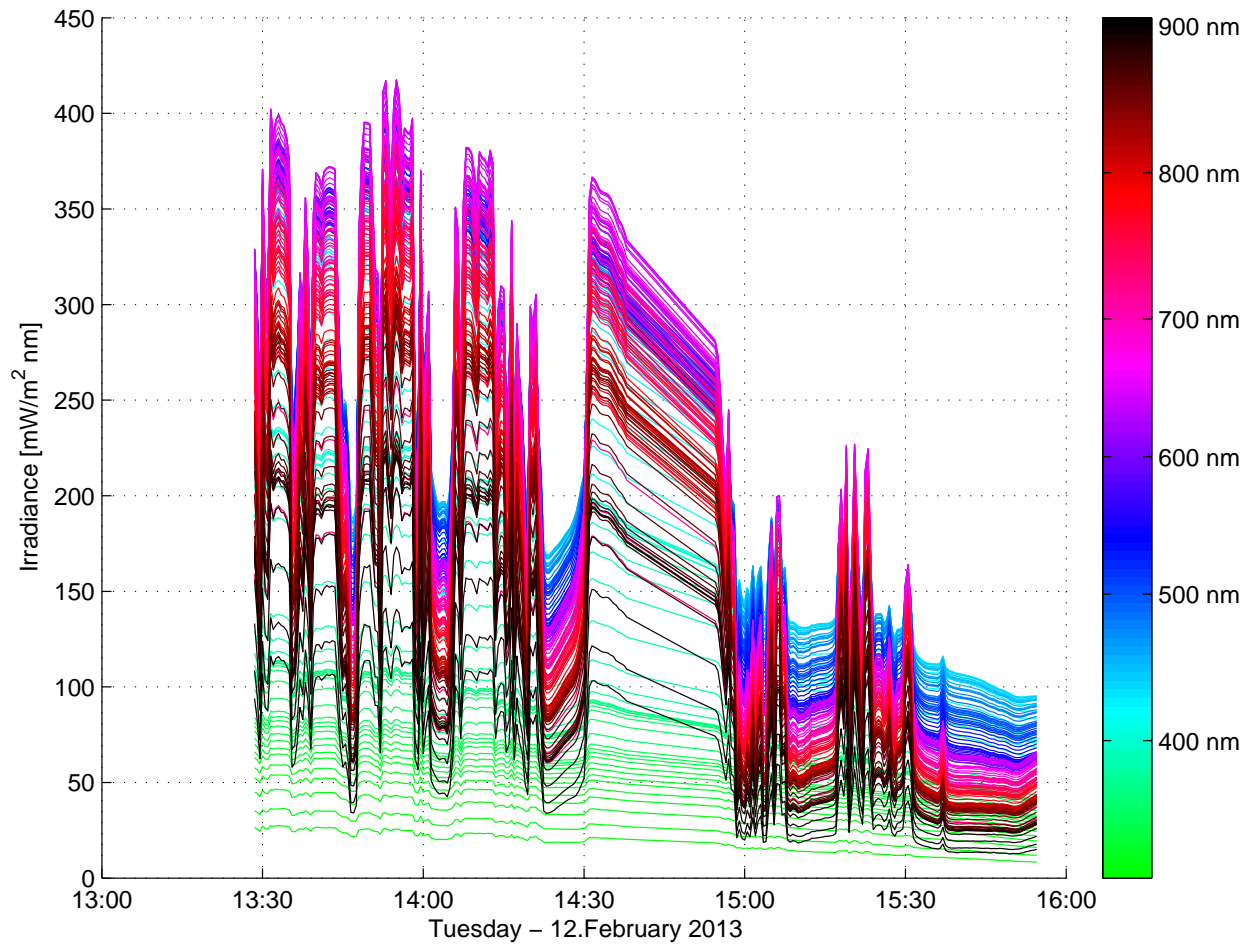


Figure 5.8: 12. February. Plot of the solar spectrum as it was measured throughout the day by the 80E2 irradiance sensor. Weather conditions were shifting cloud cover.

Figure 5.8 shows the change in irradiance for the 80E2 sensor. We see that almost the entire spectrum is greatly effected by the variations in cloud cover.

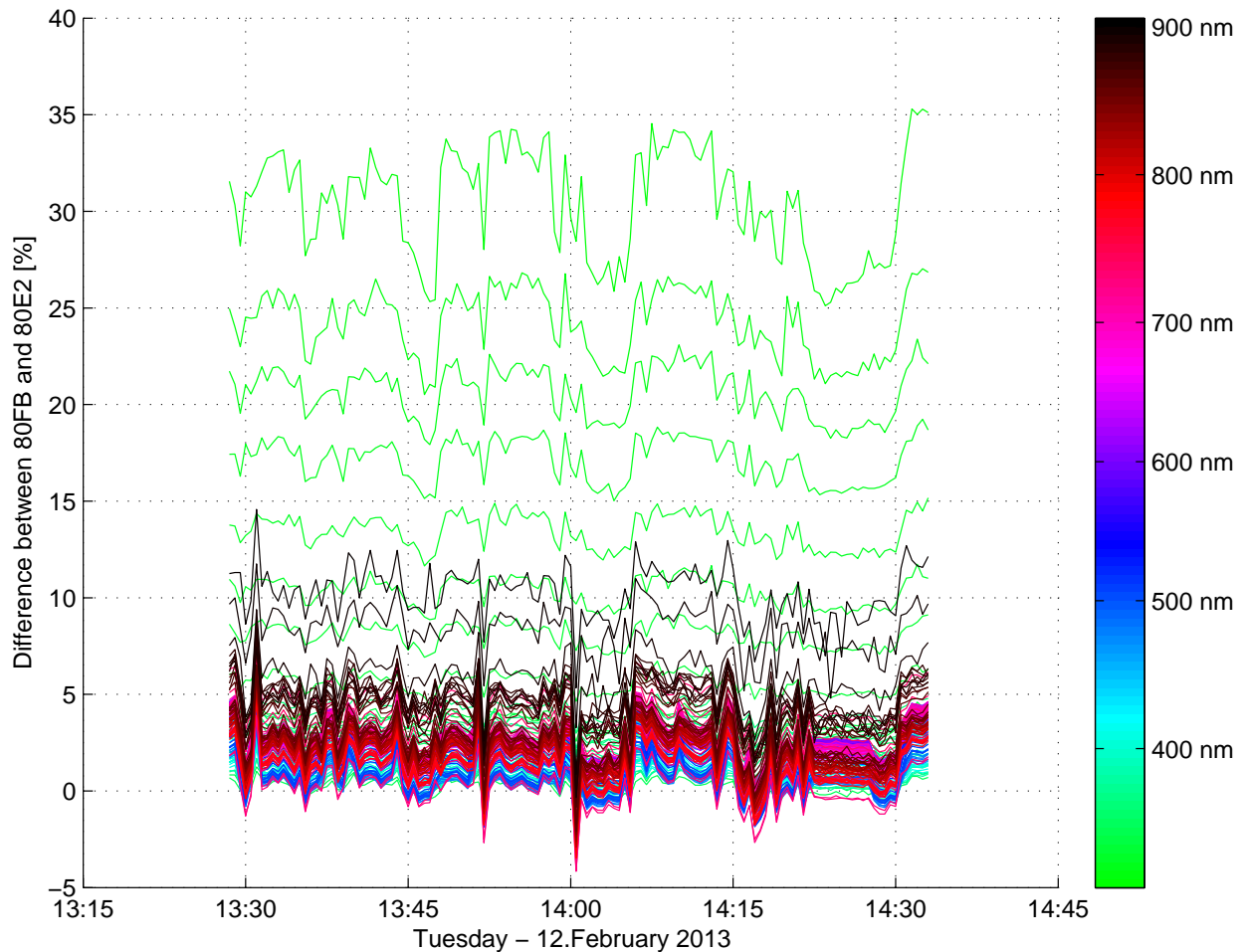


Figure 5.9: The difference, in percent, between the two irradiance sensors (80FB and the 80E2). Each line is the difference for a single wavelength over time, with a colorbar to identify the wavelengths. Both instruments were making measurements at the same time and in the same position. Weather conditions were shifting cloud cover.

Figure 5.9 shows that the difference between the two sensors remains relatively stable with shifting cloud covers. A stable difference indicates that with re-calibration of the 80FB sensor we could achieve even better results. Had the difference between the two sensors instead showed big variations with time it could have indicated a more serious fault with either one of the sensors.

5.4 Measured UV-index

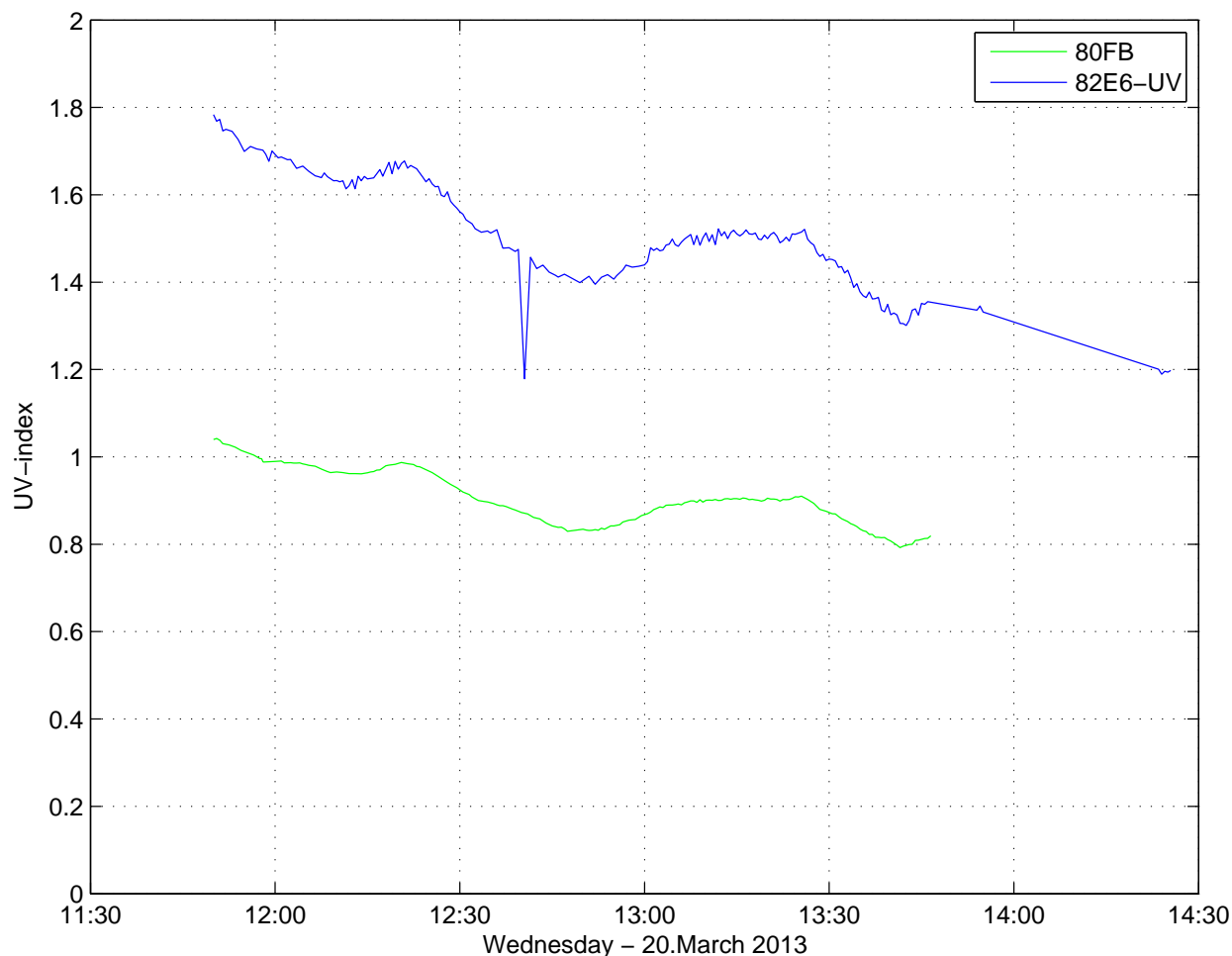


Figure 5.10: Calculated UV index based on measurements by the 80FB irradiance sensor and the 82E6 UV-irradiance sensor. Note that the 80FB sensor does not include measurements below 320 nm, it can not be considered a complete UV-index.

Figure 5.10 shows the calculated UV index based on the measured irradiance multiplied by the CIE-action spectrum (2.2). When comparing to the UV-index of around 0.7 in Bergen on 20. March 2013 as given by the Norwegian radiation protection agency (<http://www.nrpa.no/uvnett/dagsverdier.aspx?Stasjon=Bergen&Dato=20/03/2013&Zoom=True>). The 82E6 UV sensor are measuring higher values. One explanation for this over-estimation of the UV-index is that the bandwidth of the 82E6 sensor have not been taken

into account. There is reason to believe that more careful calculations would yield better results.

6 Model

In this section we will present a model called c-disort. This model is well documented and well tested numerical code that models radiative transfer in the coupled atmosphere-ocean system. Then compare these modeled results to our measurements.

When performing large scale monitoring of the ocean, only doing measurements on site fast, becomes too expensive and difficult due to the large scales involved. Satellites are very useful for this purpose as they can cover large areas. However, using satellite data to get information about local variations can be difficult. The light reaching the satellite has traveled through the atmosphere down to the ocean, before being scattered up to the satellite again. There are a number of variables that could influence the results. It is not trivial figuring out what different parameters will lead to the spectrum the satellite is recording. This is often referred to as the inverse problem, because there exists a forward problem that is much easier to solve. The direct or forward problem is solving what the satellite sensor will measure at different wavelengths with given concentrations of aerosols and atmospheric gases. Often the easiest way to solve the inverse problem is solving lots of direct problems. Therefore we need models to relatively quickly calculate the different spectra of atmospheric and ocean variables in order to figure out which combinations corresponds with the spectrum registered by the satellite sensor (K. Stamnes (2013)).

6.1 C-disort

One such tool for solving the direct problem is c-distort, which is a numerical code that models the ocean-atmosphere coupling and radiance at user-specified heights. The inclusion the ocean, the atmosphere and the coupling between them is a great advantage of this model compared to other radiative transfer simulations. Most models available for atmospheric applications calculates the radiance field for either the atmosphere or the ocean K. Stamnes (2013). This results in having to use one model to calculate the input

to the other model (Hamre (2013)). C-distort calculates the radiance field in the following way:

- Divides the ocean/atmosphere into horizontal layers. And estimate that inside a single layer all the optical properties are the same (see figure 6.1).
- Solves radiative transfer equations for all layers down to the ocean.
- Applies Snell's law and the Fresnel equations at the boundaries between the different layers
- Converts the radiative transfer equation into coupled ordinary differential equations
- Applies boundary conditions to the top of the atmosphere and bottom of the ocean

- Hamre et al. (2013)

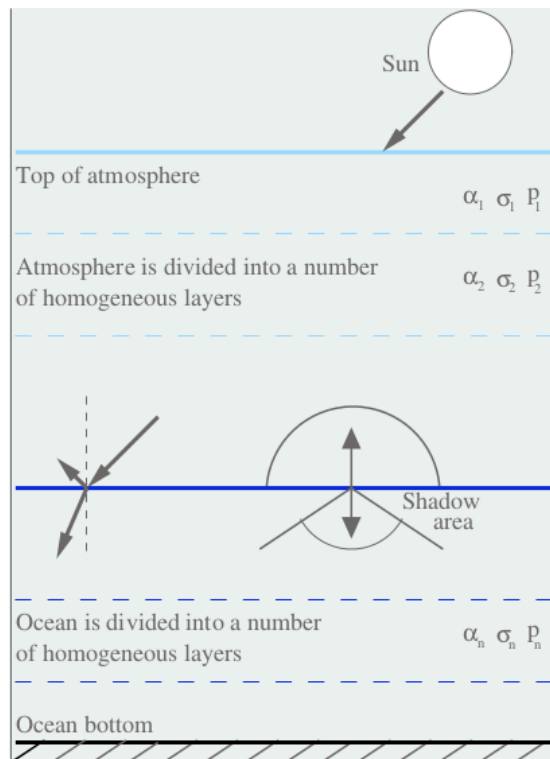


Figure 6.1: Illustration of the radiative transfer model used in the c-distort model to calculate irradiance. Dividing the atmosphere and ocean into homogeneous layers.

Comparisons with Monte Carlo simulations have shown that the c-disort model is numerically accurate - K. Stamnes (2013). Meaning that with the same optical input parameters we get the same results from both Monte Carlo and c-disort. In addition there is a big advantage in lower number of calculations/speed for the c-disort model. C-disort uses different input parameters to calculate upward, downward and direct radiance. The input parameters can be sorted into three different categories:

Information about location and atmospheric conditions: Earth-Sun distance, solar zenith angle, type of atmosphere, atmospheric gas concentrations and aerosols, optical properties of sea-bottom and various algae concentrations.

What to compute: Number of polar angles used, at what heights the different homogeneous layers will be both in the atmosphere and in the ocean, at what heights the irradiance should be calculated.

Specifications of the detector: The size of the bandwidth of the detector and at what wavelengths, azimuth/polar angles the detector measures.

The information about the location are mostly constant for a given day but, we have the option to modify atmospheric gas, aerosols, and algae concentrations to solve the inverse problem.

Since all the parameters can be calculated, at any desired accuracy level, as long as time and computational power are available, what to compute is mostly a time vs accuracy question. The more accurate calculations the longer the time.

The specifications of the detector parameters are included in c-disort to make it easier to compare the output of the model with different real life detectors as well as increasing the speed of the calculations.

A typical output of a c-disort simulation is shown in figure 6.2 with input parameters from table 3.

Table 3: Input parameters to the C-disort model used for calculations of the irradiance displayed in figure 6.2

Atmospheric type	Sub arctic summer
Weather conditions	clear sky
Solar zenith angle	45 degrees
Bandwidth	1 nm
Detector wavelengths	200:1:2000 nm

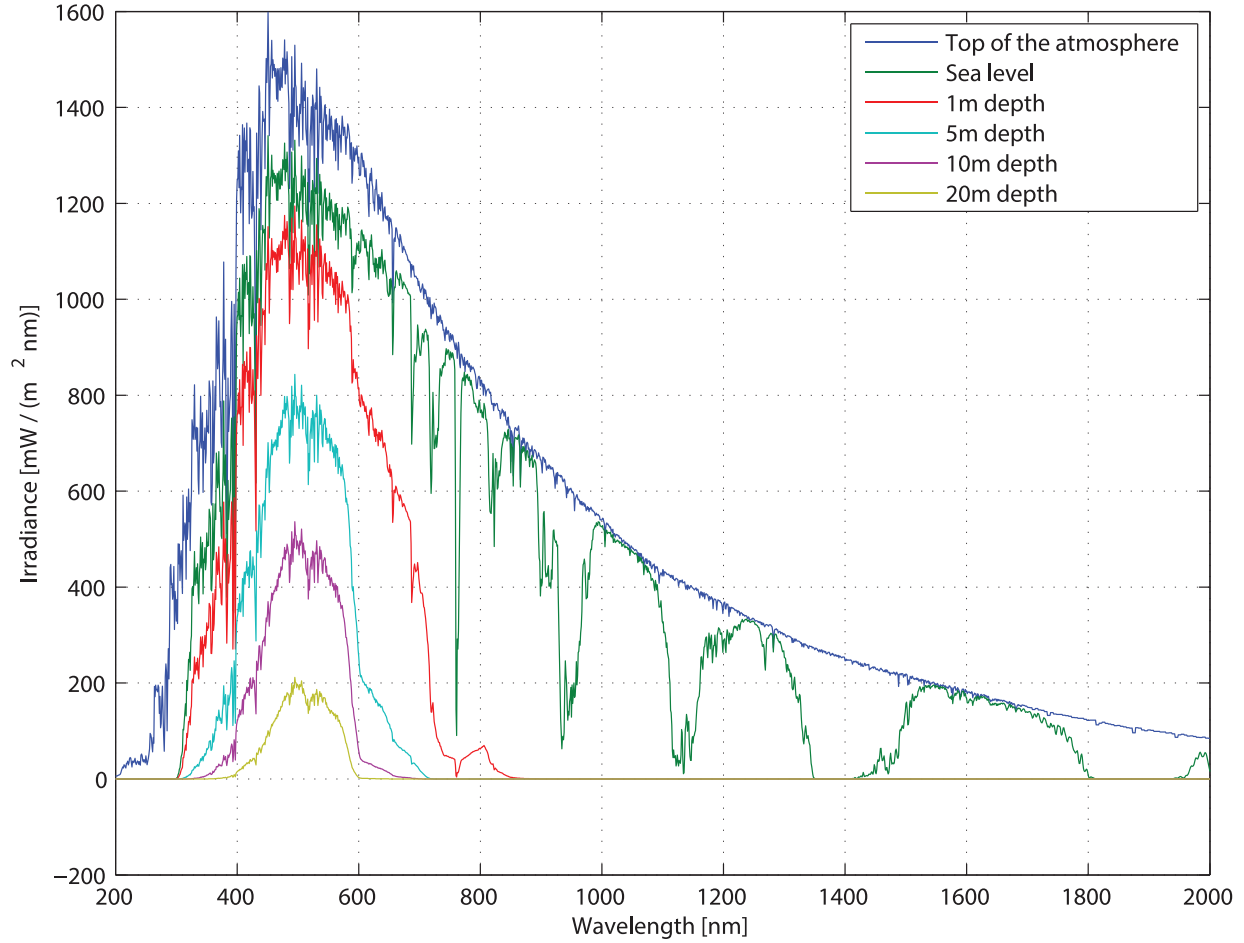


Figure 6.2: Example of different solar light spectra calculated by c-disort model, at the top of the atmosphere, sea level and for various depths in the ocean.

Table 4: Input parameters to the C-disort model used for calculations of the irradiance displayed in figure 6.3

Atmospheric type	Sub arctic winter
Weather conditions	clear sky
Solar zenith angle	75.5 degrees
Bandwidth	12 nm
Detector wavelengths	320:3.3:950 nm

6.2 Sample comparison of model and measurements

To test how the model compared to our measurements we take a closer look at a sample measurement, and have chosen from one of the field measurements on 02. February - 2013 13:00 taken at the roof of the university (University of Bergen - Department of Physics and Technology, Allegaten 55). The solar distance and solar zenith angle was found from an online solar zenith angle calculator at <http://solardat.uoregon.edu/SolarPositionCalculator.html>. Solar zenith angle was 75.5 degrees and earth radius factor 1.0287. We enter the data for the selected time into C-disort and calculate the downward irradiance at sea level both for a detailed 1 nm band spectrum and one comparable to our sensor with a bandwidth of 12 nm. These results are shown in figure 6.3 together with our measured spectrum. When comparing the higher bandwidth modeled and measured spectra to the 1 nm bandwidth spectrum we see that a lot of the finer details are lost. To make a reasonable comparison between model and measurements we compare the spectrum calculated by the model when selecting the same bandwidth and detector wavelengths as our instrument. These spectra have a similar shape but the differences was still bigger at certain absorption lines than we would expect. This increased difference we attribute to bandwidth handling. C-disort approximates bandwidth by averaging the optical properties of the atmosphere inside the bandwidth. This method saves time but it would appear that some details are lost.

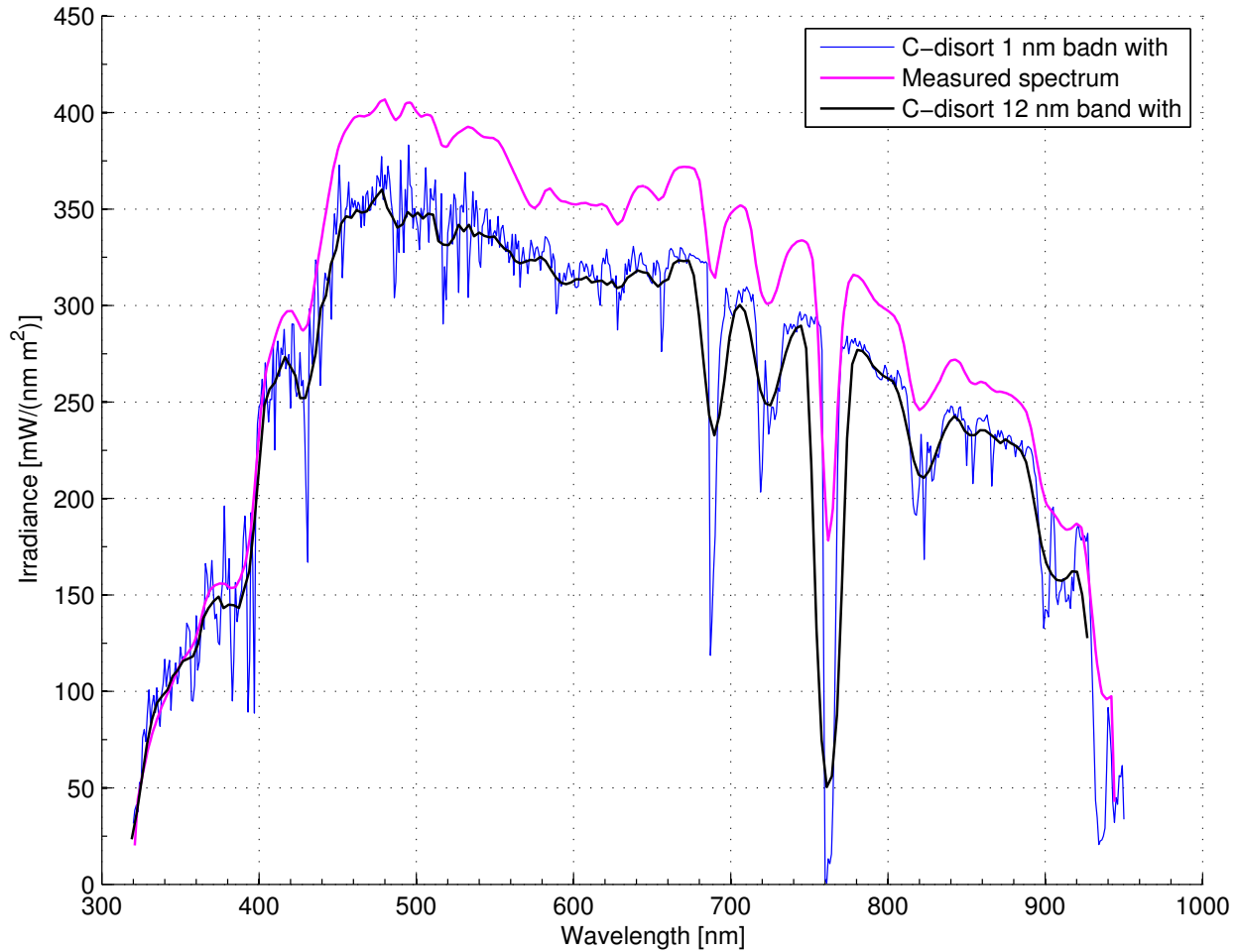


Figure 6.3: Comparison of the measured irradiance on the roof of the IFT university building in Bergen to the output both for 12 and 1 nm bandwidth, from the C-disort model. The input to the model mimicked the actual conditions for the sample day. the input is displayed in table 4.

Our measurements are about 15 percent higher than the modeled value for most of the spectrum and the difference increases around peaks and low points of the spectrum. This difference is outside of the 7-10 percent uncertainty that Trios has reported for the instrument. It is not clear if the problem lies with the input of our model or with the sensors themselves. Further examinations are needed.

6.3 Corrections

We can improve both the modeled spectrum and our measured spectrum. The modeled spectrum is improved by applying the Gaussian distribution (normal distribution) of our Ramses sensor to the accurately modeled spectrum. The Gaussian distribution function is given as:

$$E(\lambda) = \frac{1}{\sigma\sqrt{2\pi}} e^{-\frac{(\lambda-\lambda_0)^2}{2\sigma^2}}, \quad (6.1)$$

where E is the measured irradiance, λ_0 is the center wavelength and σ is the standard deviation.

We use the measured cosine response of the instrument to get a more accurate spectrum. By using the assumption that the scattered light is completely isotropic we can calculate a correction factor C to apply to our measured irradiance spectrum with the following equation:

$$E_{corrected}(\lambda) = E_{measured}(\lambda) \cdot C(\lambda) = E_{measured}(\lambda) \cdot \left(\alpha \cdot \epsilon_{direct}(\lambda, \theta) + (1 - \alpha) \cdot \epsilon_{diffuse}(\lambda) \right) \quad (6.2)$$

Where C is the total correction factor and ϵ_{direct} is the cosine correction factor we measured in the lab, $\epsilon_{diffuse}$ is the correction factor we calculated for isotropic light and α is the fraction of the direct part to the total irradiance. Due to the high solar zenith angle the correction factor, C , will mostly be dependent on the direct part of the sunlight. Both the incoming angle (SZA) and what fraction of the total irradiance comes from the direct part (α). To estimate α we turn to c-disort, as it already includes the spectrum from the direct part in its output. The solar zenith angle can be found from various online calculators. The diffuse part of the sunlight is not completely isotropic as has been shown by Arnfield (1986). However we expect this error to have a small impact on the total correction factor.

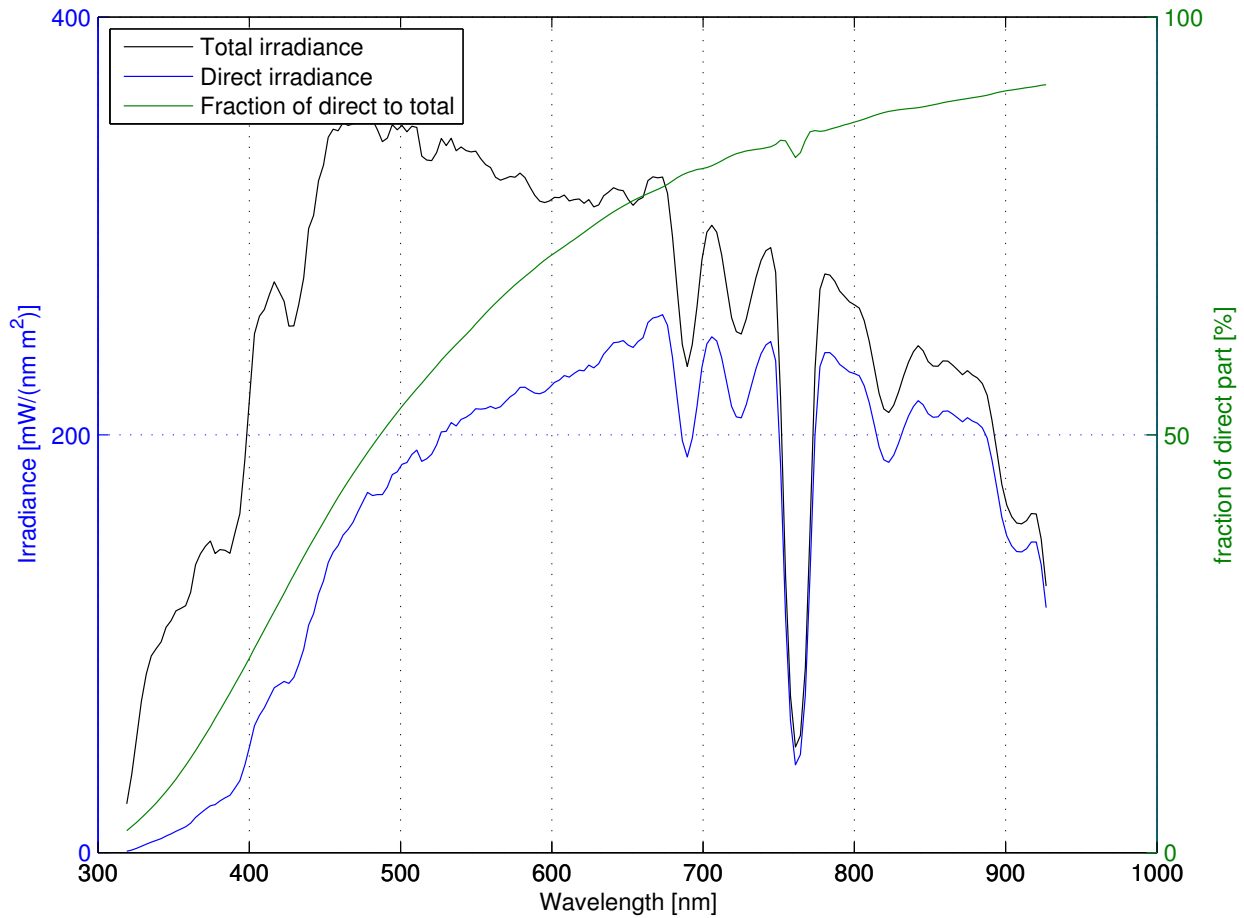


Figure 6.4: Calculated solar spectrum from the c-disort model. Including the irradiance from the direct part of the solar spectrum and what fraction of the solar irradiance comes from the direct part.

We see from figure 6.4 That the direct part becomes more and more dominant with longer wavelengths. This is to be expected since Rayleigh scattering is inversely proportional to the wavelength. High concentrations of aerosols could influence this result but are not included here.

We have plotted the correction factor for the different wavelengths in figure 6.5 with α , and solar zenith angle as found from our sample measurement. Now that we have found a correction factor it is easy to calculate a new and more accurate spectrum which is included in figure 6.6.

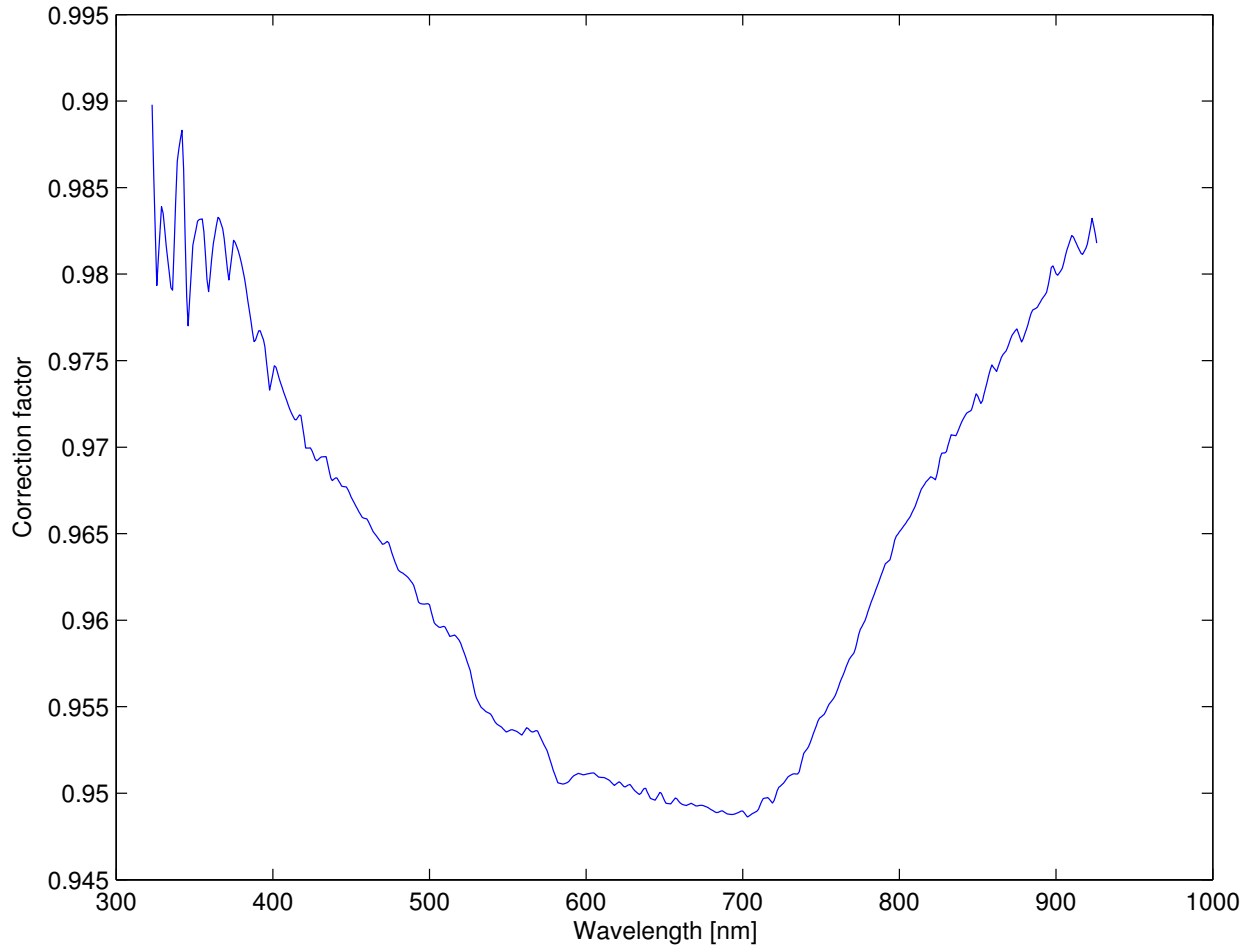


Figure 6.5: The correction factor C for the 80E2 sensor. From equation 6.2. With α as calculated by c-disort. ϵ_{direct} and $\epsilon_{diffuse}$ from the measurements in the laboratory (see figure 4.7 and figure 4.8)

From figure 6.5 we see that for our sample the biggest correction is made in the visible range and the smallest at both ends of the spectrum. This might be counter-intuitive as we would expect a sensor to be less accurate close to the ends of its range. The UV-region needs less correction because this is dominated by the diffuse part and the correction factor is small for the NIR-region because the cosine response error of the sensor is smaller in this region.

We also want to get a better spectrum from the model to compare with our sensor. Therefore we attempted another method by applying the Gaussian response curve of the instrument to the highly accurate spectrum. As we can see in figure 6.7 this resulted in the biggest differences being reduced while for the rest of the spectrum they remained about the same.

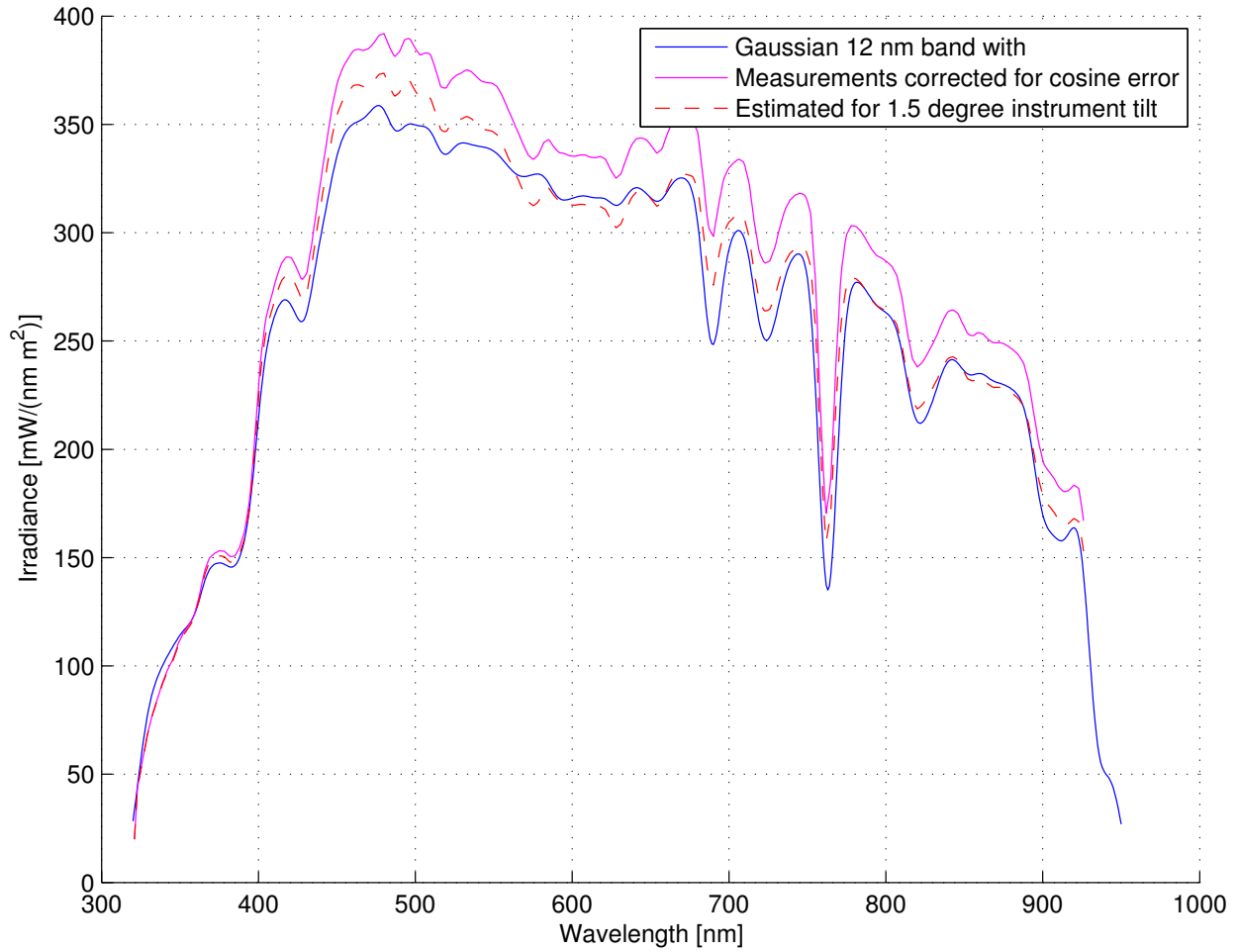


Figure 6.6: Comparison of the measurements corrected for cosine error and the spectrum calculated from the accurate model with a 12 nm bandwidth. Also included is an estimated correction for a 1.5 degree tilt of the instrument towards the sun.

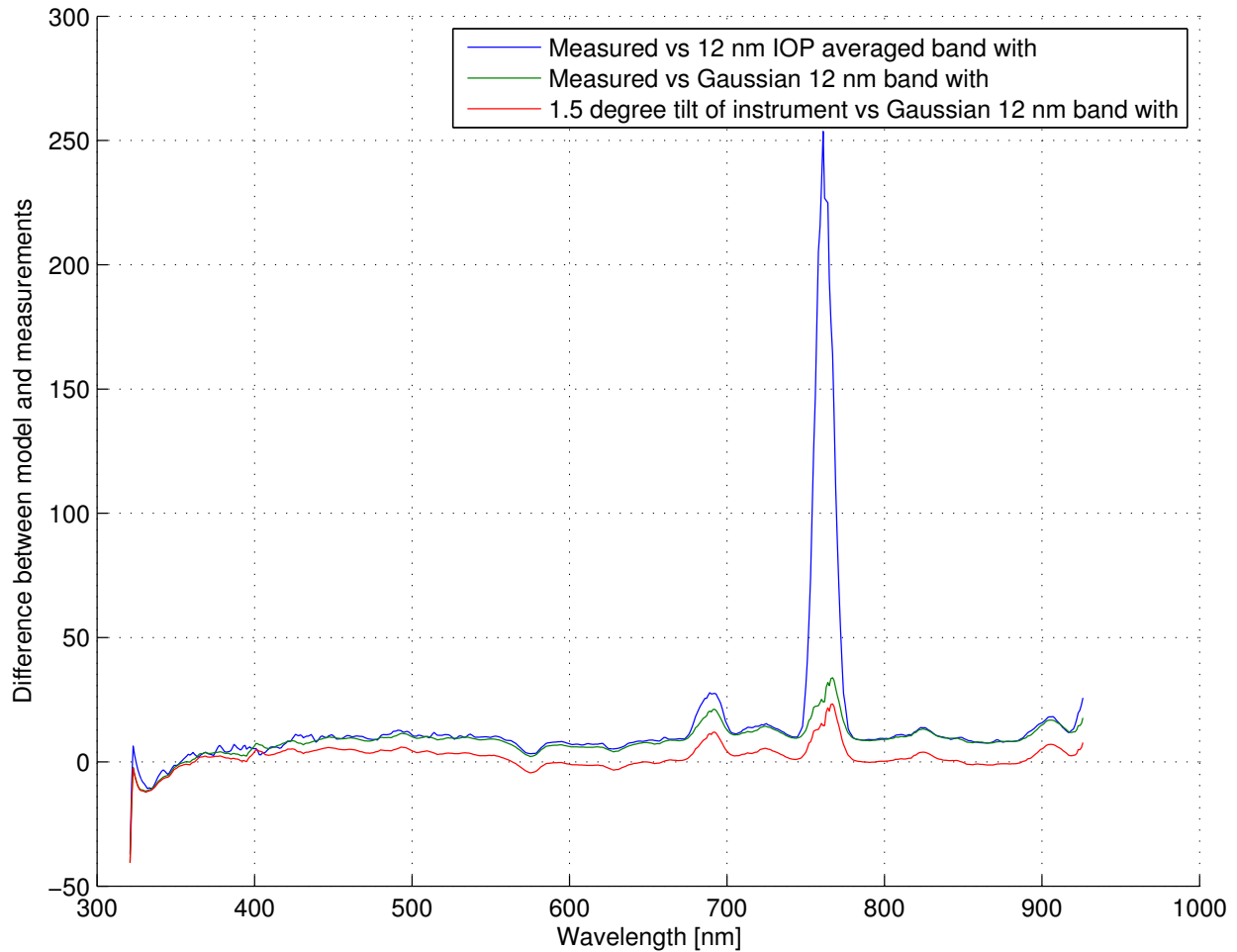


Figure 6.7: Showing the difference in percent between the corrected measurements and modeled and calculated compared to the model as a function of wavelength

In figure 6.7 with the new correction factor and improved spectrum from the model we have been able to reduce the difference from around 15% to around 9

Possible explanations for the differences in irradiance measured by the Ramses sensor compared to the model:

Reflection clouds at certain positions would result in higher irradiance. But for our sample the sky was completely blue. We also have possible reflection from the walls of the two rooms that are on top of the roof.

Solar spectrum differences exist as shown earlier with up to 6 percent variations in the

UV-region.

Angle of the sensor if the Ramses sensor was positioned leaning slightly away from the sun this would result in a lower measured irradiance as shown in figure 6.6.

Temperature There is only a default temperature setting available in the c-distort model. This default temperature is higher than the 0.8 C° registered on this date which could lead to some differences. Especially the O₂ concentration is temperature dependent (Hamre (2013)).

Bandwidth we have only measured the bandwidth at one wavelength so it is possible that it is not constant for the entire spectrum, but this is not considered very likely.

Aerosols and atmospheric gases will affect the irradiance. However these concentrations are quite low in the default setting of our model and higher concentrations should lead to lower irradiance measured on the ground.

7 Conclusion

A thorough investigation of the Ramses series of irradiance and radiance meters have been conducted. Some problems have been identified and some improvements to the accuracy of the sensors have been achieved. The stability of the sensors has been questioned in earlier projects, but we have found the sensors to be reliable, as long as regular calibrations are performed.

We have demonstrated the importance of the cosine response of irradiance sensors, and have carefully documented the cosine response error in the Ramses irradiance sensors used in this thesis. We have calculated a correction factor that can be used to improve the accuracy of measurements made with these sensors. We have shown that the measured irradiance is in agreement with the irradiance calculated by a radiative transfer model, and we have improved this agreement by applying a correction factor. The spectral accuracy of the sensors have been confirmed. We observed stable measurements, both when measuring in the laboratory and when measuring natural sunlight.

We have determined the field of view of the radiance sensor to be very close to the one specified in the manual. However the radiance sensors used in this thesis have shown a need for more testing/calibration.

The inaccuracies in the sensors we have been able to document are smaller than the inaccuracy one can expect in the alignment of the setup when doing field measurements. Hopefully the work done in this thesis have improved the value of measurements obtained with sensors from the Ramses series.

References

- Arnfield, A. (1986). Estimating diffuse irradiance on organisms: A comparison of results from isotropic and anisotropic sky radiance models. *International Journal of Biometeorology* 30(3), 201–222.
- Bais, A. F., S. Kazadzis, D. Balis, C. S. Zerefos, and M. Blumthaler (1998a, Sep). Correcting global solar ultraviolet spectra recorded by a brewer spectroradiometer for its angular response error. *Appl. Opt.* 37(27), 6339–6344.
- Bais, A. F., S. Kazadzis, D. Balis, C. S. Zerefos, and M. Blumthaler (1998b, Sep). Correcting global solar ultraviolet spectra recorded by a brewer spectroradiometer for its angular response error. *Appl. Opt.* 37(27), 6339–6344.
- Bendall, D. S., C. J. Howe, E. G. Nisbet, and R. E. R. Nisbet (2008, Aug). Introduction. photosynthetic and atmospheric evolution. *Philosophical Transactions of the Royal Society B: Biological Sciences* 363(1504), 2625–2628.
- Bernhard, G. and G. Seckmeyer (1997). New entrance optics for solar spectral uv measurements. *Photochemistry and Photobiology* 65(6), 923–930.
- Bhandari, A., B. Hamre, Ø. Frette, K. Stamnes, and J. J. Stamnes (2011, Jul). Modeling optical properties of human skin using mie theory for particles with different size distributions and refractive indices. *Opt. Express* 19(15), 14549–14567.
- Bhandari, A., S. Stamnes, B. Hamre, Ø. Frette, K. Stamnes, and J. J. Stamnes (2012, Nov). Stokes scattering matrix for human skin. *Appl. Opt.* 51(31), 7487–7498.
- Chen, Y.-C., B. Hamre, Ø. Frette, and J. J. Stamnes (2012). Climatology of aerosol optical properties in northern norway and svalbard. *Atmospheric Measurement Techniques Discussions* 5(5), 7619–7640.
- Chen, Y.-C., G. Norsang, N. Pingcuo, A. Dahlback, O. Frette, B. Kjeldstad, B. Hamre, K. Stamnes, and J. J. Stamnes (2013). Solar uv radiation measurements across the tibetan plateau. *AIP Conference Proceedings* 1531(1), 848–851.
- Demmig-Adams, B. and W. W. Adams (2000, Jan). Harvesting sunlight safely. *Nature* 403(6768), 371–374.

- Dreizin, Y., A. Tenne, and D. Hoffman (2008). Integrating large scale seawater desalination plants within israel's water supply system. *Desalination* 220, 132 – 149.
- Erga, S. R., G. C. Lie, L. H. Aarø, K. Aursland, C. D. Olseng, Øyvind Frette, and B. Hamre (2010). Fine scale vertical displacement of phaeodactylum tricornutum (bacillariophyceae) in stratified waters: Influence of halocline and day length on buoyancy control. *Journal of Experimental Marine Biology and Ecology* 384(1–2), 7 – 17.
- Erga, S. R., N. Ssebiyonga, Øyvind Frette, B. Hamre, J. Aure, Øivind Strand, and T. Strohmeier (2012). Dynamics of phytoplankton distribution and photosynthetic capacity in a western norwegian fjord during coastal upwelling: Effects on optical properties. *Estuarine, Coastal and Shelf Science* 97(0), 91 – 103.
- Fritzmann, C., J. Löwenberg, T. Wintgens, and T. Melin (2007). State-of-the-art of reverse osmosis desalination. *Desalination* 216(1–3), 1 – 76.
- Grainger, R. G., R. E. Basher, and R. L. McKenzie (1993, Jan). Uv-b robertson-berger meter characterization and field calibration. *Appl. Opt.* 32(3), 343–349.
- Gröbner, J., M. Blumthaler, and W. Ambach (1996). Experimental investigation of spectral global irradiance measurement errors due to a non ideal cosine response. *Geophysical Research Letters* 23(18), 2493–2496.
- Gröbner, J. (2003, Jun). Improved entrance optic for global irradiance measurements with a brewer spectrophotometer. *Appl. Opt.* 42(18), 3516–3521.
- Hamre, B. (2013). Personal communication: Discussion on models.
- Hamre, B., S. Stamnes, K. Stamnes, and J. J. Stamnes (2013). C-disort: A versatile tool for radiative transfer in coupled media like the atmosphere-ocean system. *AIP Conference Proceedings* 1531(1), 923–926.
- Hamre, H. B. S. J. F. O. E. S. S. (2008). Could stratospheric ozone depletion lead to enhanced aquatic primary production in the polar regions? *LIMNOLOGY AND OCEANOGRAPHY*; 53, 1; 332–338.
- K. Stamnes, W. Li, Y. F. (2013). From satellite remote sensing of the earth to non-invasive diagnostics of skin cancer. *Presentation at the Univerisity in Bergen*.

- Kiang, N. Y., A. Segura, G. Tinetti, Govindjee, R. E. Blankenship, M. Cohen, J. Siefert, D. Crisp, and V. S. Meadows (2007, Feb). Spectral signatures of photosynthesis. ii. coevolution with other stars and the atmosphere on extrasolar worlds. *Astrobiology* 7(1), 252–274.
- Kiang, N. Y., J. Siefert, Govindjee, and R. E. Blankenship (2007, Feb). Spectral signatures of photosynthesis. i. review of earth organisms. *Astrobiology* 7(1), 222–251.
- Kirk, J. T. O. (1994). *Light and Photosynthesis in Aquatic Ecosystems*. Cambridge University Press.
- Langmann, B., K. Zakšek, M. Hort, and S. Duggen (2010). Volcanic ash as fertiliser for the surface ocean. *Atmospheric Chemistry and Physics* 10(8), 3891–3899.
- Lieber, C. A., S. K. Majumder, D. L. Ellis, D. D. Billheimer, and A. Mahadevan-Jansen (2008). In vivo nonmelanoma skin cancer diagnosis using raman microspectroscopy. *Lasers in Surgery and Medicine* 40(7), 461–467.
- Michalsky, J., L. Harrison, and W. B. III (1995). Cosine response characteristics of some radiometric and photometric sensors. *Solar Energy* 54(6), 397 – 402.
- Muaddi, J. (2012). An optimal solar cell for under water measurement. *Applied Solar Energy* 48(1), 20–23.
- Platt, T. and S. Sathyendranath (1988). Oceanic primary production: Estimation by remote sensing at local and regional scales. *Science* 241(4873), 1613–1620.
- Ryer, A. D. (1997). *The Light Measurement Handbook*. 10 Technology Drive Peabody, MA01960: International Light Technologies.
- Shanmugam, P. and Y. H. Ahn (2007). Reference solar irradiance spectra and consequences of their disparities in remote sensing of the ocean colour. *Annales Geophysicae* 25(6), 1235–1252.
- Sun, J.-H., T.-K. Liu, Y.-C. Fang, C.-M. Tsai, and H.-C. Lin (2010). Optimization of 350× optical zoom lens with diffractive optical element. *Optik - International Journal for Light and Electron Optics* 121(21), 1912 – 1918.
- TriOS (2012). *RAMSES - Hyperspectral radiometer manual* (Rel. 1.1 ed.). Werftweg 15, D26135 Oldenburg, Germany: Trios.

Webb, A. R., H. Slaper, P. Koepke, and A. W. Schmalwieser (2011). Know your standard: Clarifying the cie erythema action spectrum. *Photochemistry and Photobiology* 87(2), 483–486.

ZEISS (2011). *MMS - monolithic Miniature-Spectrometer manual*. D 07740 Jena Germany.

Zibordi, G. and B. Bulgarelli (2007, Aug). Effects of cosine error in irradiance measurements from field ocean color radiometers. *Appl. Opt.* 46(22), 5529–5538.